Revalorization of the Antimicrobial Activity of Nanostructure- Based Materials with an Emphasis on TiO_2

By

Kelsey Fournier

A thesis submitted in partial fulfillment of the requirements for the Master's degree of Science in Chemistry

Department of Chemistry and Bimolecular Sciences

University of Ottawa

Abstract

The exploration in the use of nanomaterials for a multitude of different applications has grown within the last few years. This is largely due to the vast number of features exhibited by nanoscale materials when compared to their bulk counterparts. The use of nanomaterials in environmental applications can come in different facets, such as, the production of clean energy in solar cells and the application of nanotechnologies in coatings for building exterior surfaces.

The first section of the thesis focuses on the use of nanomaterials for water remediation, since purified groundwater is still not globally accessible. Chapter 2 focuses on the use of Pd nanoparticles supported on TiO_2 (Pd@TiO_2) to photo-generate H_2 while using bacterial cells as sacrificial electron donors (SEDs) rather than chemical reagents. Different conditions were examined to investigate the photo-destruction of gram negative bacteria, *E. coli*, which is a microbial pollutant often found in a number of different water sources. Samples containing photocatalyst in solution were irradiated using a solar simulator, which is a light source that is similar to the solar spectrum, for applications in a flow system. Chapter 3 is a project in collaboration with Dr. Edith Amuhaya and her research group in Nairobi, Kenya exploring the use of porphyrins, an organic compound, supported on glass wool for water treatment in a flow system. Porphyrins are photosensitizers that generate reactive oxygen species (ROS) when exposed to light and oxygen. However, their high solubility in aqueous media makes it difficult to use them for water remediation and can add an extra step in the process of water purification. Therefore, we suggest attaching the porphyrins to glass wool, which is an inexpensive and inert support that can easily be removed from a flow system. Here, we explore the use of glass wool as a support for a series of different conjugated porphyrins and metalloporphyrins. We have synthesized different porphyrins bearing carboxylic group substituents to enable ease of deposition onto the amino-functionalized glass surface (glass surface modified with (3-Aminopropyl) triethoxysilane, APTES). The

characterization of the materials suggests some of the porphyrins retain the ability to absorb solar light and generate reactive oxygen species upon irradiation. Antimicrobial activity and degradation of selected pollutants were also explored.

The last section of the thesis discusses a different approach regarding nanoparticles. Typically, nanoparticles are used for their reactivity when they absorb light, often producing a high number of free radicals in the process. However, this high reactivity can become an issue when these free radicals cause unintended damage to biological environments. This is the case for TiO_2 used for photo-protection sunscreens, where there has been some concern regarding the free radical damage to skin. Previously, the group has synthesized TiO_2 particles in a thin shell of lignin, a natural biopolymer. Lignin is an antioxidant that can scavenge the radicals produced by the photo-excited TiO_2 and prevent them from being released into the surrounding media. Here, we further characterize and investigate the properties of the lignin on TiO_2 nanoparticles and attempt to scale up the production of the particles.

Acknowledgements and Contributions

It has been a great and enriching experience to have conducted my graduate studies under Dr. Tito Scaiano's supervision. Not only was it an environment that encouraged me to grow and push my boundaries as a scientist but it also enabled me to develop close friendships and life long relationships. I would like to begin by thanking Tito for taking a chance and welcoming me into the group. He was continuously supportive throughout my graduate career and is one of the kindest people I have had the fortune of working with. I would also like to thank Anabel Lanterna, who was instrumental to my success. Anabel always made herself available when I had questions, not only in my research but in my personal life as well. I would also like to thank my parents, whose unwavering support and love has given me the confidence to pursuit my own chosen career path.

I have also had the opportunity to meet many new people during the course of my graduate career. I would like to thank everyone who I have been able to work with. Jazmin, you have taught me so much and have been a great mentor and I am so thankful that I can call you a friend. I feel very lucky to have been able to meet you. I would also like to thank Dr. Edith Amuhaya, James and everyone in Dr. Amuhaya's group, who've made my trip to Kenya a very fun and educational experience; it is one that I will never forget. I would also like to acknowledge the contribution and help from Dr. Amuhaya's group for helping me with the synthesis of my porphyrins and for guiding me in that field. To all the visiting students with whom I've been able to work, thank you for all the great chats, I have really learned a lot from all of you.

Lastly, I would like to thank my colleagues and friends in the department. You all have supported me in different ways and I will always appreciate the closed bonds we have formed.

Table of Contents

List of Figures

List of Schemes

List of Tables

List of Abbreviations

0D	zero dimensional
1D	one dimensional
^{1}H	hydrogen nucleus (proton)
$^{1}O_2$	singlet oxygen
2D	two dimensional
3D	three dimensional
$^{3}O_2$	ground state oxygen
A-Si	amorphous silicon
AFM	atomic force microscopy
AgNPs	silver nanoparticles
APTES	(3-Aminopropyl) triethoxysilane
band gap	E_b
C-Si	single crystalline silicon
CB	conduction band
CFU	colony forming unit
DBPs	disinfection by-products
DCC	N,N –Dicyclohexylcarbodiimide
DLS	Dynamic Light Scattering
DMF	dimethylformamide
DMPO	5,5-Dimethyl-1-pyrroline N-oxide
DR	Diffuse Reflectance
e^-	electron
EDTA	ethylenediaminetetraacetic acid
E_g	energy gap
EHP	electron-hole pair
EPR	electron paramagnetic resonance
EtOH	ethanol
eV	electron volt
GC-TCD	gas chromatography thermal conductivity detector
GHG	greenhouse gas
GRASE	generally recognized as safe and effective
GW	glass wool
h^+	hole
HOMO	highest occupied molecular orbital
ICP-OES	Inductively Coupled Plasma Optical Emission spectroscopy
LB	Luria-Bertani
LOD	limit of detection
LOQ	limit of quantification
LSPR	localized surface plasmon resonance
LUMO	lowest unoccupied molecular orbital
MED	minimal erythema dose
NaOD	sodium deuteroxide solution

NIR	near infrared
nm	nanometer
NP	nanoparticles
$O_2^{\bullet -}$	superoxide radical anion
OH•	hydroxyl radical
PABA	p-aminobenzoic acid
PBS	phosphate buffered saline
PDT	photodynamic therapy
PS	photosensitizer
R_∞	absolute reflectance
ROS	reactive oxygen species
rpm	revolutions per minute
SED	sacrificial electron donor
SEM	scanning electron microscopy
SPF	sun protection factor
SPP	surface plasmon polaritons
SPR	surface plasmon resonance
TCPP	5,10,15,20-tetrakis (4-carboxyphenyl) porphyrin
TEM	transmission electron microscopy
TGA	thermogravimetric analysis
TMPP	5,10,15,20-tetrakis(4-methoxyphenyl) porphyrin
TMSP	3-(trimethylsilyl)-2,2,3,3-tetradeuteropropionic acid
UV	ultra violet
UVR	ultraviolet radiation
VB	valence band
Vis	visible
Zn $(Oac)_2$	zinc acetate

Chapter 1
Introduction

Introduction

1.1 Nanomaterials

Nanomaterials are defined as materials with an internal structure or with external dimensions that are in the nanoscale region; where at least one dimension of the material ranges between 1 nm and 100 nm.[1–3]

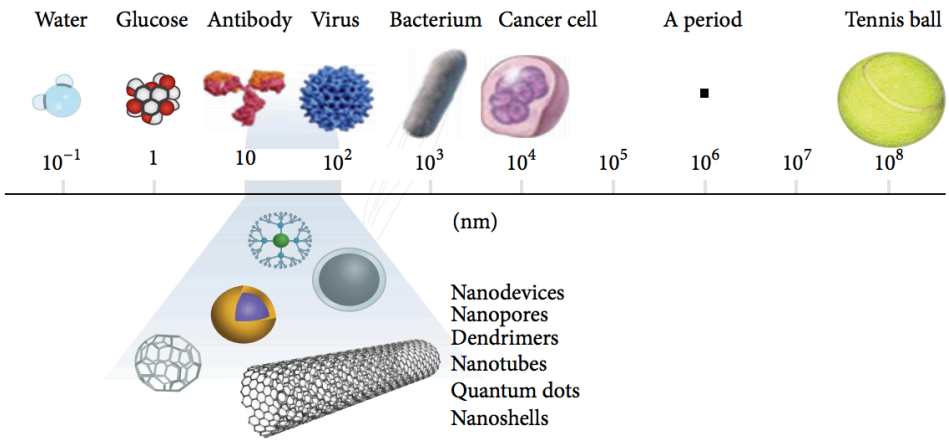

Figure 1.1. Nanomaterial size comparison with other materials of a larger size. Reprinted with permission from M. T. Amin *et al.*[3] Copyright (2014) Advances in Materials Science and Engineering.

History of nanomaterials

The use of nanomaterials dates far back in history, with one of the first known uses of nanomaterials being in Mesopotamia during 9th century, where nanoparticles were used to create the glittering effect seen on the surface of pots. This effect was produced by the homogeneous dispersion of silver and copper nanoparticles suspended in the matrix of the glass.[2,4] Another classic example of the use of nanoparticles in ancient artifacts is the Lycurgus cup created by the Romans around AD 400, where the cup changed colour upon

being exposed to a light source. The chalice is green in appearance until light is shone upon it where it will consequently appear red due to the presence of Au-Ag alloyed nanoparticles, as shown in Figure 1.2.

Figure 1.2. The Lycurgus cup, an example for use of nanotechnology materials in ancient times. Department of Prehistory and Europe, The British Museum © The Trustees of the British Museum.

The unknown use of nanomaterials may have occurred many years ago, however the first scientific report concerning nanoparticles was reported much later in 1850; where a colloidal solution of gold nanoparticles called “activated gold” was synthesized using a phosphorous-based reducing agent by Michael Faraday. In his scientific report, he provides one of the first descriptions of the optical features of metal nanomaterials.[5]

1.2 Nanomaterial characteristics

Nanomaterials are composed of single or multi-phase chemical elements that can give the material different or improved catalytic, electrical, magnetic and/or thermal properties that are superior to the corresponding bulk material.[6] The enhancement in the materials abilities, at the nanoscale size, can be attributed to surface effects and quantum effects that occur with the decrease in size. Materials at the nanoscale have an increased chemical reactivity and a lower melting point than their larger-scale counterparts due to the increase in the

fraction of atoms found at the particle's surface.[7] Simply, as the surface area per mass of material increases, the more of this material can come into contact with it's surrounding environment, thus increasing its reactivity (Figure 1.3). There are also quantum effects that can be observed when you have a nanoparticle or quantum dot that has electrons confined in a very small space that can manifest in a quantized energy spectrum. This results in magnetic moments that would not occur in bulk material such as palladium, gold or platinum.[8,9]

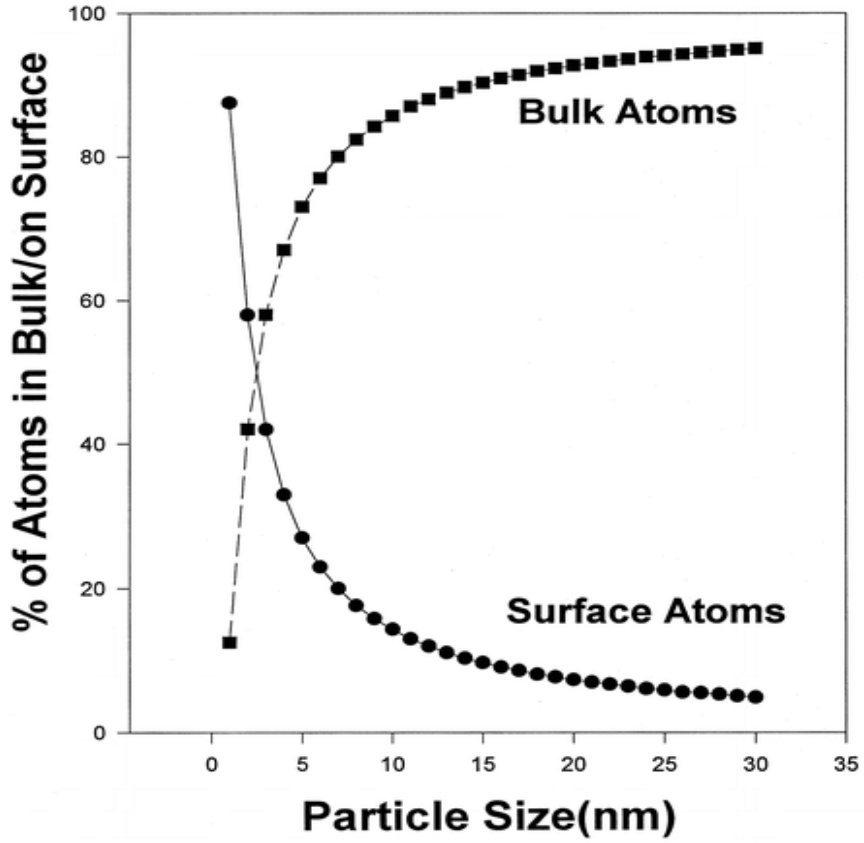

Figure 1.3. Surface to bulk ratios calculation for spherical metal nanoparticles against size. Reprinted (adapted) with permission from K. J. Klabunde *et al.*[7] Copyright (1996) American Chemical Society.

1.3 Manufacturing of nanomaterials

There are various strategies that can be utilized when synthesizing nanoparticles. Different approaches will yield nanoparticles consisting of different type of structures and surface coatings. In general, techniques for nanomaterial

synthesis can be categorized into two different principles of synthesis: top down and bottom up.

The top down approach begins with the size reduction of the bulk material to the nanoscale level. This route typically makes use of mechanical processes such as crushing, sputtering, mechanical milling or grinding to etch out crystal planes.[10,11] There are limitations to this technique; the first being that it is an unsuitable method choice for the production of uniformly shaped materials because it is difficult to fully control particle shape. The second is that it is also difficult to manufacture very small particles, even with high-energy consumption.

Bottom-up approach is an alternative technique often utilized for nanomaterial synthesis. This method is based on the formation of nanomaterial from the atomic or molecular species by means of chemical reaction or self-assembly.[12] This allows for greater control over the uniformity of the size, shape and distribution of the nanomaterial. Control over these parameters is a result of two main parts of the bottom-up synthesis: nucleation and growth. For example, synthesis of metal nanoparticles can occur with reduction of the metal salt precursor to the atomic state (I, C_s). The saturation of precursor solute increases to a level where the critical energy barrier (activation energy) is overcome, resulting in rapid self-nucleation (II, C_{min}). Homogeneous nucleation of these nanoparticles can occur spontaneously but must reach a supercritical state such as supersaturation (C_{max}).[13] With increasing consumption of the precursor solute, the saturation level decreases below self-nucleation, ending the nucleation period. Growth then occurs due to the diffusion of the monomers through the solution yielding monodispersed particles (III), as shown in Figure 1.4.[14,15]

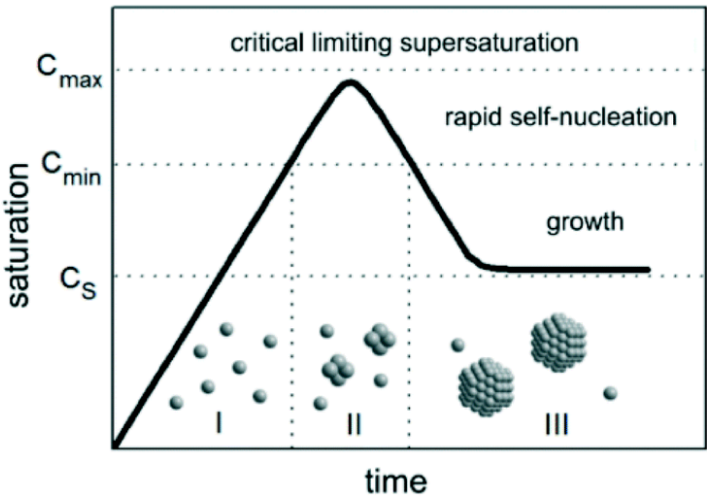

Figure 1.4. LaMer nucleation diagram. Reproduced with permission from S. Arshadi *et al.*[13] Copyright (2015) The Royal Society of Chemistry.

Within the bottom up approach, there are a number of different techniques that can be utilized to yield nanoparticles possessing different structural, physicochemical and morphological characteristics. In this thesis, the production of metal nanoparticles utilizes LaMers nucleation mechanism via the reduction of metal salts.

Classification of nanomaterials

Nanomaterials can be synthesized with a number of dimensions ranging from 1 to 100 nm. Their classification is dependent on the dimensionality of the nanostructures. Ultra-dispersive materials that have all dimensions within the nanoscale region are considered zero dimensional (0D). This includes nanoparticles, and nanopowders (Figure 1.5 A). One-dimensional (1D) structures contain two external dimensions in the nanoscale region and one in the microscale; such as nanorods and nanowires (Figure 1.5 B). Two dimensional (2D) nanomaterials only contain one external dimension at the nanoscale range, for example, nanosheets and nanofilms (Figure 1.5 C). And lastly, three dimensional (3D) nanomaterials, have no dimensions in the nanoscale range, such as the bulk material (Figure 1.5 D).[16]

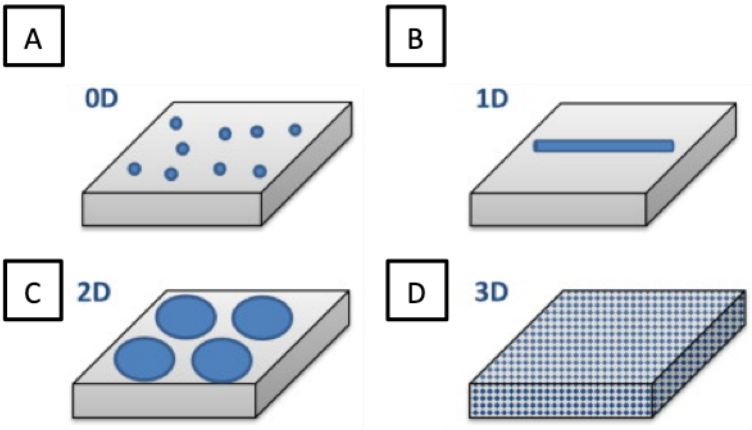

Figure 1.5. Dimensionality classification of: A zero-dimensional, B one-dimensional, C two-dimensional and D three-dimensional materials. Reproduced with permission from R. I. Dolez[17] Copyright (2015) Elsevier, Nanoengineering.

1.4 Metal nanoparticle plasmons

Optical properties demonstrated by nanoscale metals and semiconductors are frequently due to the occurrence of plasmons. Plasmons are described as a collective oscillation of free electron gas density.[18] The type of plasmon that occurs is dependent on the dimensions of the metallic object. An electromagnetic excitation can propagate along the interface between a metal and the dielectric medium called surface plasmon polaritons (SPPs) (Figure 1.6 a). The two dimensional nature of the SPP peaks at the interface will exponentially decay as the distance from the surface increases.[19,20] However, when the particle is much smaller than the incident wavelength, there is an interaction between the light and the metal nanoparticle that produces a localized surface plasmon resonance (LSPR). This phenomenon occurs when the particle's free electrons collectively oscillate in resonance (Figure 1.6 b).[21,22] LSPRs will create an enhanced electromagnetic field that is extremely sensitive to changes in the surrounding electric medium.[23]

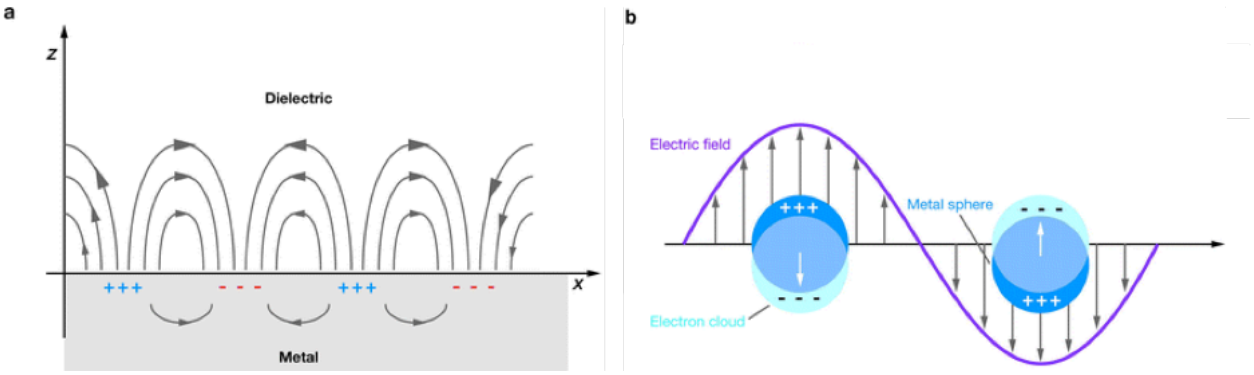

Figure 1.6. Diagrams demonstrating (a) surface plasmon polariton (SPP) and (b) localized surface plasmon (LSPR). Adapted with permission from K. Willets *et al.*[21] Copyright (2017) Annual Reviews.

When an electromagnetic wave, such as a ray of incident light, meets an obstacle or a scattering particle, it creates a scattering of light that can be thought of as light redirection. The interaction between the electromagnetic wave and the particle causes the orbit of the surface electrons to be periodically disturbed with the same frequency as the incident wave's electric field. This induces a dipole moment where there is a periodic separation of charge within the molecule, as seen in figure 1.6 b. The dipole moment will result in scattered light, as it is a source of electromagnetic radiation, producing a phenomenon called elastic scattering. Elastic scattering occurs when most of the light that is scattered by the particle is emitted at a frequency that is identical to that of the incident light.[24]

In the twentieth century, Mie developed a theoretical description for this effect by offering an analytical solution of Maxwell's equations for the scattering of electromagnetic radiation by homogeneous spherical nanoparticles that have a uniform complex index of refraction. Mie's theory, describes the extinction spectra (equation 1.1), at a given wavelength for a particle with a known diameter and refractive index.

$$\boldsymbol{Q_e = Q_s + Q_a} \qquad (1.1)$$

Where Qe is the extinction efficiency of a particle, Qs is the nanoparticle's scattering efficiency, Qa is the nanoparticle's absorption efficiency.

Mie scattering describes situations where the size of the scattering particle is comparable to that of the wavelength of light. This differs from Rayleighs approximation (scattering), where elastic scattering of light occurs by particles that are significantly smaller than the wavelength of the incident electromagnetic radiation; this scattering primarily refers to scattering from atmospheric gases.[25]

Hot electrons

Nanoparticles that contain plasmon-excited oscillations have shown to be a source of "hot" electrons (Figure 1.7a). Subsequent to excitation, plasmons can radiatively decay into re-emitted photons or decay non-radiatively, producing an electron-hole pair (EHP).[26] The excited electrons within the metal move from the occupied energy level in the valence band (VB), to the unoccupied conduction band (CB), above the Fermi level (Figure 1.7b). The high-energy "hot" electrons produced by the decay of the LSPR are able to extend further away to the surface of the nanoparticle, which can be used for photocatalysis (Figure 1.7c).

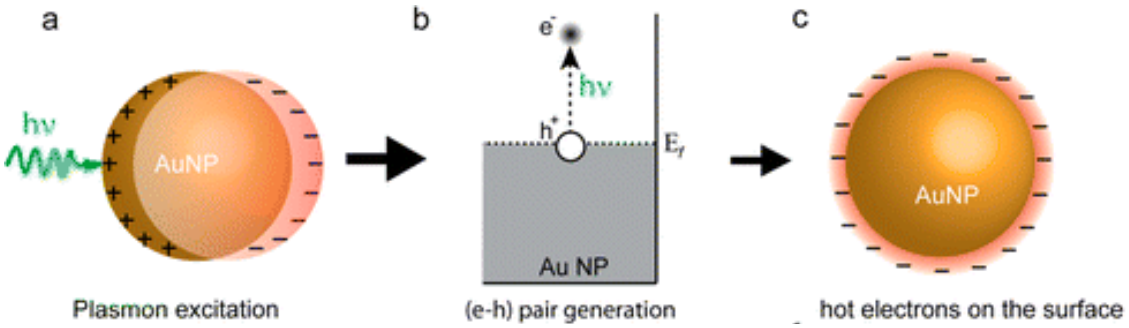

Figure 1.7. Scheme of hot electrons generated in Au plasmonic nanostructures. Adapted with permission from S. Mukherjee *et al.*[25] Copyright (2013) American Chemical Society.

The formation of these hot electrons on the surface of photo-absorbing nanoparticles can play a role in their photocatalytic activity. For example, it was discovered that "hot" electrons resulting from the excited surface plasmons of small Au nanoparticles were able to dissociate H_2.[26] Furthermore, it was found that Au nanostructures could produce local hyperthermic effects to bacteria, such

as *Staphylococcus aureus,* when irradiated with a laser light in the visible region (~530 nm).[27]

1.5 Applications of nanomaterials

Recent attention has evolved surrounding nanomaterial's due to the number of physical and chemical properties they exhibit when compared to their bulk counterparts. They offer unprecedented opportunities in many different areas of research that can range from improving current technologies, from solar cells to biological systems, which includes the application of nanoparticles for imaging, biosensing, and medical diagnostics.[28] Additionally, a significant area of research is the use of nanomaterials for environmental research, in particular, the use of photocatalysts for water decontamination.

Energy harvesting

A major source of energy comes from fossil fuels, which are a non-renewable energy sources that are primary contributors to global warming and climate change through the release of carbon dioxide and other greenhouse gases.[29,30] This has resulted in a shift towards the development of alternative renewable energies that are generated from available resources while remaining cost-effective and efficient. Nanotechnology is one of the leading candidates to reduce the impact of energy production due to the optical properties, catalytic nature, and large surface area of the nanomaterials.[31] Rather than use oil and other fossil fuels for a source of energy, solar power is a less environmentally impactful resource for electricity. Solar cells have been developed to absorb solar light, trap this solar energy and convert it into electrical energy.

Constant reconstruction of the solar cell is being undertaken with a main goal in mind: the production of the solar cell must be low-cost while trying to improve the efficiency by either enhancing the materials ability to absorb light or to minimize loss in electricity/heat after the light has been absorbed. The first generation of solar cells was based on single crystalline semiconductor wafers.

Using silicon solar cells can yield relatively high efficiencies in converting solar energy to electricity. This is illustrated in figure 1.8, where single crystalline silicon (C-Si) had an efficiency of ~25%. However, this requires a thick film (>100 μm) to optimize light absorption, which can lead to poor electricity collection because the minority carrier diffusion length, which is the average distance a minority carrier will travel before recombining, must be larger than the film thickness.

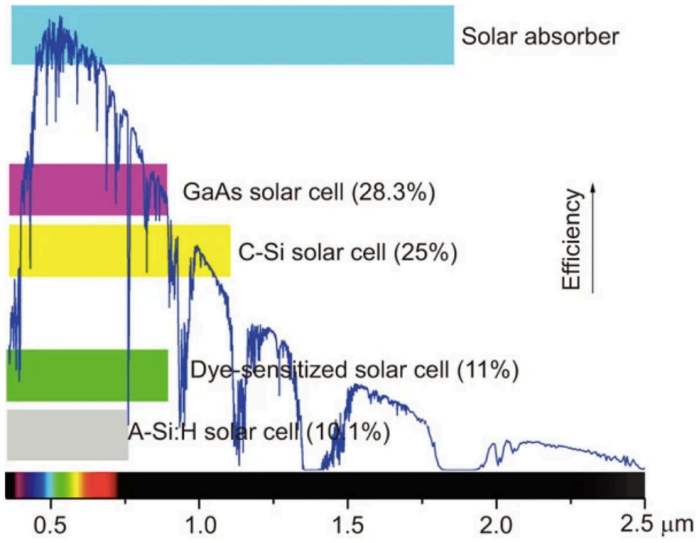

Figure 1.8. Comparison of the efficiency of several solar energy harvesting techniques against the solar spectrum and their respective working wavelength from I. Khan *et al.*[30] Copyright (2014) Springer Nature.

This led to the development of new solar cells technologies constructed using inorganic thin film in the cells. The decrease in the active layer thickness enables the reduction in the carrier recombination and thus, increases the conversion efficiency. This new generation of solar cells is made from highly absorbing materials such as GaAs and amorphous silicon (A-Si) that can reduce the active layer thickness to lower than a few microns. Additionally, the switch to thinner films can lower the amount of semiconducting materials used and consequently, can reduce the cost of production. Thin film solar cells have also been subject to further improvement through the integration of plasmon

structures that can retain high absorbance capabilities but can also decrease the thickness of the photovoltaic material. [32]

Biological

Nanoparticles have also gained a great deal of attention for their diverse application in the biomedical field. The unique properties exhibited by nanoparticles; such as the high surface to mass ratio and reactivity at the surface makes them applicable for a wide spectrum of biomedical purposes, ranging from drug delivery to biosensors.

There are many shortcomings when it comes to traditional drug delivery practices. Since most current drugs used for therapy fail to reach the targeted tissue and get distributed to normal cells, treatment efficiency is often reduced. For example, cytostatic drugs that are used for chemotherapy are unable distinguish between cancer and healthy cells, which can lead to severe and dangerous side effects.[33] The use of nanoparticles enables the reduction of undesirable effects and can protect the drugs from degrading during transport. Depending on the composition, nanoparticles can contain fluorescent properties, be responsive under light exposure (UV, Vis or NIR excitation) and contain an electric/ magnetic field, which would enable better tracking of the drug and increase control of the drug's release. Moreover, the composition of the nanomaterial can be modified (for example the charge, size, etc.) to not only improve cellular uptake of drugs but also help control distribution to the intended site in the body.[16,34]

There has also been a focus on the development of a broad range molecules used as sensors at low concentrations while still maintaining a high specificity. In recent years, metal nanoparticle-based biosensors have been investigated as a new class of biosensors due to the physicochemical properties offered by metals in the nanoscale region. Noble metal nanoparticles can be functionalized with different moieties, such as antibodies, enzymes, or other proteins in an attempt to improve biocompatibility and specificity for the target.[35]

The use of noble metals in nanobiosensors has garnered much attention. In particular, gold nanoparticles have been of interest due to their unique optical properties. Gold nanoparticles can be easily synthesized to form a number of different shapes that can range in size between 3 and 200 nm in diameter. They have optical properties within the visible range of the light spectrum that can induce surface plasmon resonance (SPR) setups that enables a visible color change when there is a change in the frequency of oscillation of the electrons. These characteristics allow for gold nano-colorimetric biosensors for DNA or oligonucleotide detection.[36,37]

Environmental

Current practices for water remediation often use strong oxidants such as chlorination that can result in the production of disinfection by-products (DBPs) including trihalomethanes and haloacetic acids. This has increased the exploration of using engineered photocatalytic nanostructures in water treatment systems. Photocatalytic disinfection offers many advantages including, the ability to use solar energy provided by natural sunlight or artificial light, as well as, using inorganic nanomaterials that can be recycled.[38] Furthermore, it does not require the consumption of oxidizing agents, which are often expensive. These features are particularly attractive for water remediation in developing countries or in remote and rural areas where access to clean water is limited.

Nanoparticles can decontaminate water using different mechanisms, depending on structure and composition of the materials. Nanotechnology comprised of titanium oxide (TiO_2), silica (SiO_2) or carbon nanotubes (CNTs), for example, demonstrate microbicidal effects that can remove and/or inactivate a number of different pathogens including bacteria, viruses, fungi and protozoa.[39] Nanoparticles can also be modified to be able to adsorb heavy metals and remove toxic pollutants and pharmaceuticals from sullied bodies of water.[40,41]

1.6 Photocatalysis

Photocatalysis is the modification of the rate of a chemical reaction by either direct irradiation or by the irradiation of a catalyst, without the catalyst being consumed. The use of a photocatalyst provides the benefit of increasing the rate of reaction by lowering the activation energy, which enables the reaction to occur under milder conditions.[42] Catalysis can be divided into two different categories –homogeneous and heterogeneous. In a homogeneous reaction, the catalyst and product are in the same phase as the reactant, whereas with heterogeneous catalysis, the catalyst is in a different phase. However, this classification system can overlook some occurrences that can happen during the reaction. Figure 1.7 depicts three different examples of this phenomenon. The first is heterogeneous catalysis to homogeneous catalysis where the active species is leached from the heterogeneous catalyst, diffuses away from the surface and reacts in the homogenous phase (left-hand image, Figure 1.8). The second is where the homogeneous catalyst forms an insoluble nanostructure complex that can behave as a heterogeneous catalyst in situ (middle image, Figure 1.8). Lastly, the phenomenon where the heterogeneous catalyst will leach the catalytic species that goes on to react in the homogeneous phase and then returns and deposits onto the surface of the heterogeneous material (right-hand image, Figure 1.8)[43]

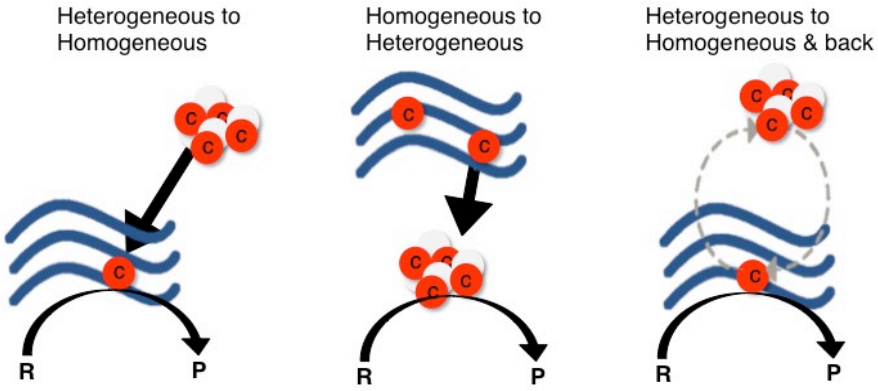

Figure 1.9. Schematic representations of three types of heterogeneous catalysis with respect to reactant (R) and the formation of the product (P).

1.7 Semiconductors

Heterogeneous semiconductors can be advantageous and more environmentally friendly than homogeneous photocatalysts in chemical processes, since they are more readily removed from the reaction mixture and can be reused for subsequent reactions.

Semiconducting materials contain unique properties where electrical conductivity is between that of an insulator and a conductor. These electrical properties are a result of the positioning of the materials valence band (VB) and conduction band (CB).

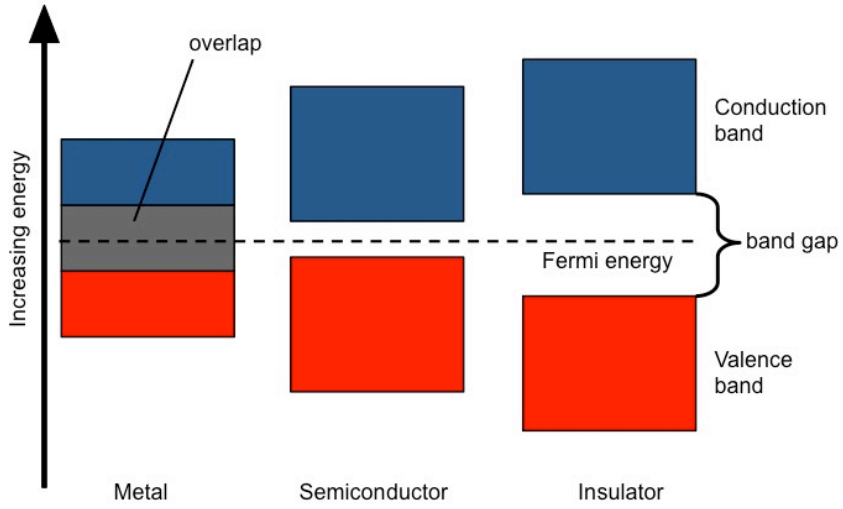

Figure 1.10. Diagram illustrating the valence and conduction bands of metals, semiconductors and insulators.

The VB is similar to the highest occupied molecular orbital (HOMO), where it is the outermost electron orbital of an atom in a material that is occupied with electrons. Similarly, the CB is the lowest unoccupied molecular orbital (LUMO), which is a band of electron orbitals that is high in energy but generally empty where excited electrons jump into from the VB. The difference in energy between the VB and CB is called the band gap energy, denoted by E_g in Figure 1.10, which is an indication of the electrical conductivity of the material. The structuring

of the bands (band gap) in addition to the positioning of the VB and CB are important properties for a semiconductor photocatalyst. They will determine the semiconductors light absorption properties and its redox capability.[44]

A widely used semiconducting photocatalyst is titanium dioxide (TiO_2). Common application of TiO_2 is for the creation of the white pigmentation in paints and coatings. It is a cheap and chemically stable material with a high refractive index that makes it a very desirable substance to produce white opaque coatings.[45] While it is still being used today in industrial applications like glazes, foods and cosmetics, to name a few, it has also been the focus in the application of energy and environmental research. TiO_2 based nanoparticles have the ability to reduce or oxidize materials by converting solar energy into chemical energy to drive a number of chemical reactions; from the generation of hydrogen to the removal of organic and biological pollutants.[46,47] Although TiO_2 has become one of the most popular and widely studied photocatalysts due to its high photocatalytic reactivity and photostability, there are some limitations of using this heterogeneous material. TiO_2, in its most common crystalline form, anatase, contains a large band gap (3.2 eV), which limits light absorption to the ultraviolet (UV) range. This can be problematic since UV is only a small fraction of the solar spectrum (~ 3-5%) limiting its application in reactions that utilizes solar energy.[48]

The photocatalytic capability of a semiconductor can be improved by different techniques. The band gap can be engineered to develop semiconducting materials with a narrower band gap.[49] Tuning the physical properties of the material can also broaden the absorbance by changing the crystallinity, crystal structure or size of the particle to improve the charge separation and migration. Additionally, decorating the material with metal nanoparticles can enhance a semiconductor's photocatalytic activity. Decorating or doping a semiconductor will increase the photo-responsive region and improve the electron-hole separation, thus, increasing the oxidative power of the photogenerated carriers. Quite often, noble metals are used as electron

acceptors to lower the rate of recombination of the photoinduced hole- electron pair separation and promote electron-transfer processes at the interface.[50]

1.8 Characterization of nanoparticles

Various instruments can be utilized to investigate nano-scale materials.

UV-Vis Spectroscopy

UV-Vis spectroscopy is an analytical technique that measures how much a chemical substance can absorb light. The spectrophotometer measures the intensity of light in the UV/Visible region that is passed through a sample. From this measurement, the absorbance can be calculated by the equation 1.2.

$$A = -\log(T) \tag{1.2}$$

Where T is the transmittance, which can also be defined as I/I_0. I is the radiation coming out of the cuvette and I_0 is the radiation going in the cuvette.

The absorbance spectrum can give data used to obtain various pieces of information regarding the material sampled. This technique can be used in a qualitative manner to identify functional groups or to confirm the structural identity of an organic/ inorganic compound with a known specific absorption spectrum.

For example, silver nanoparticles (AgNPs) can vary in size and morphology. The shape of the material can be nanorods, nanoplates and dodecahedra depending on the method of synthesis.[51,52] As shown in Figure 1.10, the shape of AgNPs can be quickly identified using UV-Vis spectroscopy.

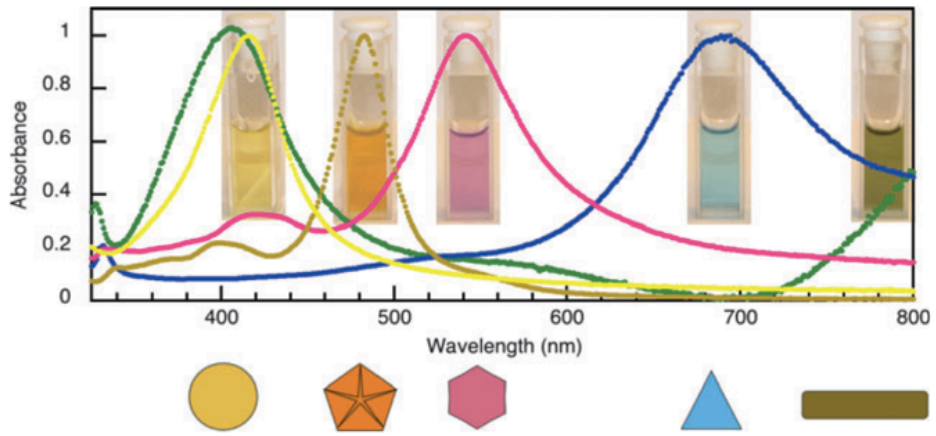

Figure 1.11. Absorption spectra for the corresponding morphologies that can be generated with the LED irradiation approach from a single precursor solution of 3 nm AgNP seeds. Reprinted with permission from K. G. Stamplecoskie *et al.*[50] Copyright (2010) American Chemical Society.

UV-Vis can also be used in a quantitative manner to determine the concentration of analyte in solution. The UV-Vis spectrum graphically depicts the absorbance as a function of wavelength. The Beer-Lambert Law governs the calculation for the concentration, which is shown in the following equation:

$$A = \varepsilon c l \tag{1.3}$$

Where A is absorbance (optical density), C is sample concentration (M), l is cuvette path length in cm, and ε (epsilon) is the sample specific constant in $M^{-1}cm^{-1}$. The height of the peak is directly proportional to the concentration of the species. In addition to using a spectrophotometer to determine concentration, it can also be used determine the analyte concentration against time and other physico-chemical parameters.

Diffuse Reflectance

Diffuse reflectance (DR) spectroscopy is a technique that can useultraviolet (UV), visible and near infrared (NIR) light to study the spectral characteristics of solid-state samples, including crystalline materials or powders. This technique is based on the principle that when light is shone on a sample, some of that monochromatic light is absorbed, and some of that light will reflect,

not only from the surface of the sample (specular reflection) but some will also be reflected internally (diffuse reflectance).[53] Some of the light will scatter and return to the surface after multiple reflections. The total light reflected is usually measured relative to a non-absorbing standard that is either a ring type reflectance attachment or an integrating sphere. The integrating sphere is a hollow enclosure, which contains an internal surface made of a non-selective diffuse reflector. The diffuse reflectance spectrum that is acquired is converted to a Kubelka-Munk function, where:

$$f(R_\infty) = \frac{(1-R_\infty)^2}{2R_\infty} = \frac{K}{S} \quad (1.4)$$

Where, R_∞ is the absolute reflectance, K is the absorption coefficient and S is the scattering coefficient. However, the absolute reflectance (R_∞) is difficult to measure in practice, therefore, the comparative reflectance, r, is measured with respect to a standard, where K is nearly zero (0) in the actual measurement range. So rather,

$$r_\infty = \frac{r_\infty(sample)}{r_\infty(standard\ powder)} \quad (1.5)$$

is measured and equation,

$$f(r_\infty) = \frac{(1-r_\infty)^2}{2r_\infty} = \frac{K}{S} \quad (1.6)$$

is determined.

Dynamic Light Scattering (DLS)

Dynamic Light Scattering (DLS) is a method used to analyze the size of spherical colloids in suspension. DLS can acquire data quickly and provide information (average estimations) regarding aggregation and size of particles in suspensions, ranging in size from ~0.2 nm to ~10 μm.[54] The instrument measures Brownian motion of particles and correlates this motion with the size of the particles. Brownian motion is the random movement of particles that is produced by the surrounding solvent molecules. DLS measures the hydrodynamic radius of a molecule suspended in liquid, not just the core. The

Stokes–Einstein equation is used to derive the hydrodynamic radius R_h from the translational diffusion coefficient D_T.

$$D_\tau = \frac{k_B T}{6\pi\eta R_h} \quad (1.7)$$

Where, k_B is the Botlzmann constant (1.380×10^{-23} kg.m^2.s^{-2}.K^{-1}), T is absolute temperature, η is the viscosity of the solution and R_h is the hydrodynamic radius of the particle.[55]

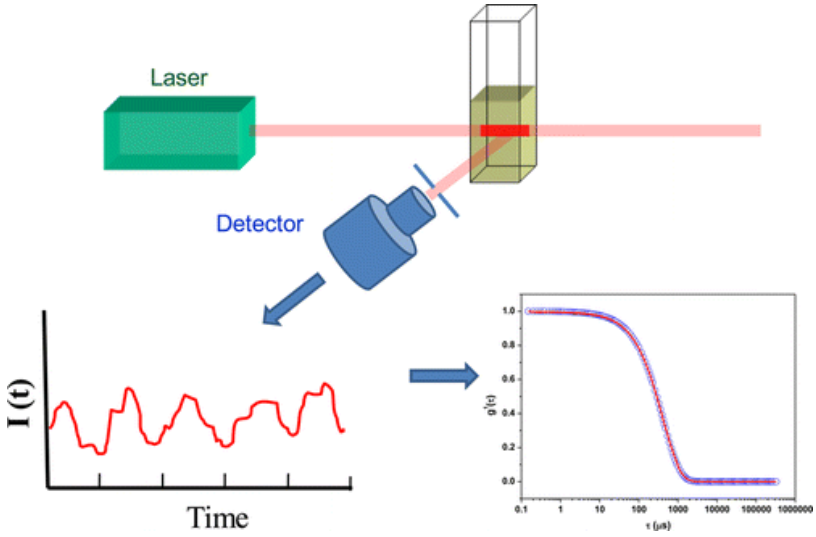

Figure 1.12. Schematic and example of data produced by dynamic light scattering instrument. Reproduced with permission from P. A. Hassan *et al.*[54] Copyright (2014), American Chemical Society.

In a DLS instrument, a laser of a known wavelength is passed through a dilute sample. When it encounters molecules in solution, the incident light scatters and the intensity of this light measured by a detector (Figure 1.12).

The random motion of particles leads to random fluctuations in signal. This is due to the changing constructive and destructive interference of scattered light. Smaller particles are pushed further by the solvent molecules and will move more rapidly. The larger the particle, the more slowly it diffuses and the smaller Brownian motion will be.

The Zetasizer software can provide information regarding the state of aggregation of the sample by DLS. The two most widely used methods for this are ‘size distribution by intensity’ and ‘size distribution by volume’.

Some of the limitations of DLS for size analysis is that DLS will give the hydrodynamic radius, which can include any stabilizer bound to the molecule that cannot be seen with microscopic techniques. Therefore, it often gives size values that are larger than those provided by other analytical techniques such as atomic force microscopy (AFM), scanning electron microscopy (SEM) and transmission electron microscopy (TEM).

Fluorescence Spectroscopy

Fluorescence spectroscopy is a technique used to measure fluorescence properties of a sample. A beam of light passes through the sample and can excite the electrons of the material by UV or visible radiation. The sample then emits photons with a wavelength longer than the excitation light and can fluoresce in the UV/Vis/NIR region. There are two types of measurements: emission and excitation spectrum, which can tell you different information about your sample. For an emission spectrum, the excitation monochromator is set to a given wavelength to excite the sample, and the fluorescence emission intensity is scanned over a series of different emission wavelengths.

Fluorescence is a type of luminescence that is predominantly concerned with vibrational and electronic states. Most molecules occupy the lowest vibrational level of the ground state at room temperature. When light is absorbed, the electronic state is elevated to generate an excited state of the molecule. The molecule begins in the ground state (S_0) and can go to higher states such as the first (S_1) or second (S_2) or even the nth excited state. The molecule can be excited to any of the vibrational sub-levels associated with each electronic state.[56] Even though the sample can be excited to different electronic states that contain multiple vibrational and rotational energy levels, electrons that are reach

an energy state higher than S_1 will relax back to the first excited state extremely quickly and emit from the lowest excited level, in accordance to Kasha's rule.[57]

Measurements of fluorescence and phosphorescence are collected using a fluorometer, often with a liquid sample held in a cuvette. However, conventional fluorescence spectroscopy can also be applied to solid-state samples, which was utilized for qualitative analysis of samples in Chapter 3.

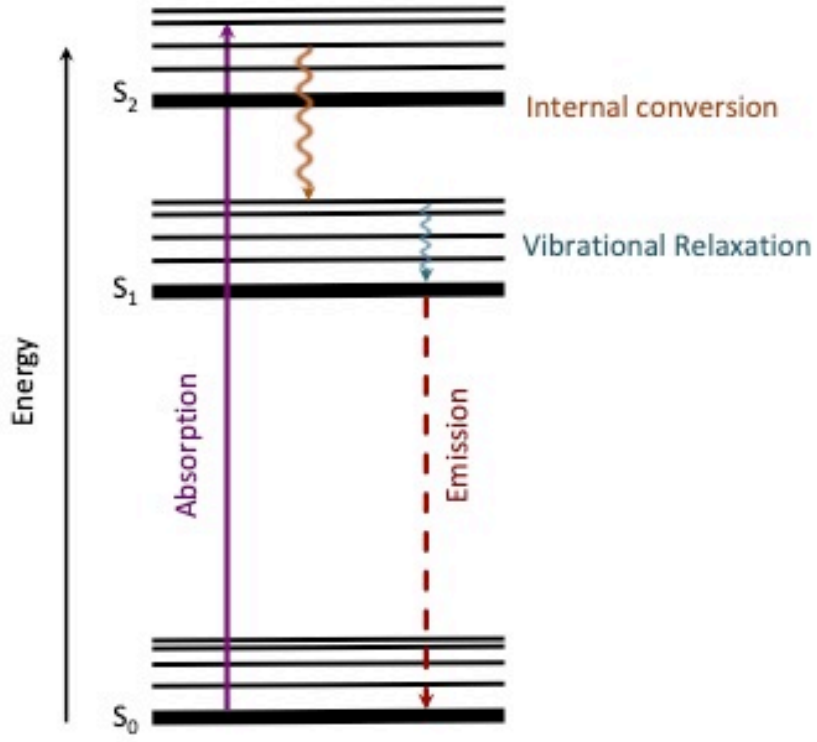

Figure 1.13. Simplified Jablonski diagram showing a possible scenario with absorption, internal conversion and vibrational relaxation, and emission. Adapted permission from L. K. McKenzie *et al.*[54] Copyright (2018) Elsevier, Coordination Chemistry Reviews.

References

1 Nanomaterials definition matters, *Nat. Nanotechnol.*, 2019, **14**, 3, 193.

2 P. N. Sudha, K. Sangeetha, K. Vijayalakshmi and A. Barhoum, in *Emerging Applications of Nanoparticles and Architectural Nanostructures: Current Prospects and Future Trends*, 2018, pp. 341–384.

3 M. T. Amin, A. A. Alazba and U. Manzoor, A review of removal of pollutants from water/wastewater using different types of nanomaterials, *Adv. Mater. Sci. Eng.*, 2014, 825910.

4 J. Pérez-Arantegui, J. Molera, A. Larrea, T. Pradell, M. Vendrell-Saz, I. Borgia, B. G. Brunetti, F. Cariati, P. Fermo, M. Mellini, A. Sgamellotti and C. Viti, Luster Pottery from the Thirteenth Century to the Sixteenth Century: A Nanostructured Thin Metallic Film, *J. Am. Ceram. Soc.*, 2001, **84**, 2, 442–46.

5 K. Parveen, V. Banse and L. Ledwani, in *AIP Conference Proceedings*, 2016.

6 J. Huang, L. Lin, D. Sun, H. Chen, D. Yang and Q. Li, Bio-inspired synthesis of metal nanomaterials and applications, *Chem. Soc. Rev.*, 2015, **44**, 17, 6330–6374.

7 K. J. Klabunde, J. Stark, O. Koper, C. Mohs, D. G. Park, S. Decker, Y. Jiang, I. Lagadic and D. Zhang, Nanocrystals as stoichiometric reagents with unique surface chemistry, *J. Phys. Chem.*, 1996, **100**, 12142–12153.

8 R. Nagarajan, Nanoparticles: Building blocks for nanotechnology, *ACS Symp. Ser.*, 2008, **996**, 2–14.

9 C. Buzea and I. Pacheco, in *EMR/ESR/EPR Spectroscopy for Characterization of Nanomaterials*, ed. A. K. Shukla, Springer India, New Delhi, 2017, pp. 3–45.

10 T. Prasad Yadav, R. Manohar Yadav and D. Pratap Singh, Mechanical Milling: a Top Down Approach for the Synthesis of Nanomaterials and Nanocomposites, *Nanosci. Nanotechnol.*, 2012, **2**, 3, 22–48.

11 J. Singh, T. Dutta, K.-H. Kim, M. Rawat, P. Samddar and P. Kumar, 'Green' synthesis of metals and their oxide nanoparticles: applications for environmental remediation, *J. Nanobiotechnology*, 2018, **16**, 1, 84.

12 N. Kumar and S. Kumbhat, in *Essentials in Nanoscience and Nanotechnology*, 2016, pp. 29–76.

13 J. Polte, Fundamental growth principles of colloidal metal nanoparticles - a new perspective, *CrystEngComm*, 2015, **17**, 36, 6809–6830.

14 N. T. K. Thanh, N. Maclean and S. Mahiddine, Mechanisms of nucleation and growth of nanoparticles in solution, *Chem. Rev.*, 2014, **114**, 15, 7610–7630.

15 S. Arshadi, J. Moghaddam and M. Eskandarian, LaMer diagram approach to study the nucleation and growth of Cu_2O nanoparticles using supersaturation theory, *Korean J. Chem. Eng.*, 2014, **31**, 11, 2020–2026.

16 L. Yan and X. Chen, in *Nanocrystalline Materials: Their Synthesis-Structure-Property Relationships and Applications*, 2014, pp. 221–268.

17 P. I. Dolez, in *Nanoengineering: Global Approaches to Health and Safety Issues*, 2015, pp. 3–40.

18 K. M. Mayer and J. H. Hafner, Localized surface plasmon resonance sensors, *Chem. Rev.*, 2011, **111**, 6, 3828–3857.

19 P. Berini and I. De Leon, Surface plasmon-polariton amplifiers and lasers, *Nat. Photonics*, 2012, **6**, 16–24.

20 A. V. Zayats, I. I. Smolyaninov and A. A. Maradudin, Nano-optics of surface plasmon polaritons, *Phys. Rep.*, 2005, **408**, 3, 131–314.

21 M. Pelton, J. Aizpurua and G. Bryant, Metal-nanoparticle plasmonics, *Laser Photonics Rev.*, 2008, **2**, 3, 136–159.

22 K. A. Willets and R. P. Van Duyne, Localized surface plasmon resonance spectroscopy and sensing, *Annu. Rev. Phys. Chem.*, 2007, **58**, 267–297.

23 E. Kazuma and T. Tatsuma, Localized surface plasmon resonance sensors based on wavelength-tunable spectral dips, *Nanoscale*, 2014, **6**, 2397–2405.

24 D. W. Hahn, Light Scattering Theory, http://plaza.ufl.edu/dwhahn/Diagnostic Tutorials.html, (accessed 24 May 2020).

25 X. Li, L. Xie and X. Zheng, The comparison between the Mie theory and the Rayleigh approximation to calculate the EM scattering by partially charged sand, *J. Quant. Spectrosc. Radiat. Transf.*, 2012, **113**, 3, 251–258.

26 S. Mukherjee, F. Libisch, N. Large, O. Neumann, L. V. Brown, J. Cheng, J. B. Lassiter, E. A. Carter, P. Nordlander and N. J. Halas, Hot electrons do the impossible: Plasmon-induced dissociation of H_2 on Au, *Nano Lett.*, 2013, **13**, 1, 240–247.

27 Y. Feng, L. Liu, J. Zhang, H. Aslan and M. Dong, Photoactive antimicrobial nanomaterials, *J. Mater. Chem. B*, 2017, **5**, 44, 8631–8652.

28 H. Liang, X. B. Zhang, Y. Lv, L. Gong, R. Wang, X. Zhu, R. Yang and W. Tan, Functional DNA-containing nanomaterials: Cellular applications in biosensing, imaging, and targeted therapy, *Acc. Chem. Res.*, 2014, **47**, 6, 1891–1901.

29 M. Höök and X. Tang, Depletion of fossil fuels and anthropogenic climate change-A review, *Energy Policy*, 2013, **52**, 797–809.

30 A. Shahsavari and M. Akbari, Potential of solar energy in developing countries for reducing energy-related emissions, *Renew. Sustain. Energy*

Rev., 2018, **90**, 275–291.

31 I. Khan, K. Saeed and I. Khan, Nanoparticles: Properties, applications and toxicities, *Arab. J. Chem.*, 2017, **12**, 7, 908–931.

32 C. Fei Guo, T. Sun, F. Cao, Q. Liu and Z. Ren, Metallic nanostructures for light trapping in energy-harvesting devices, *Light Sci. Appl.*, 2014, **3**, 4, e161.

33 S. Juneja, A. Ghosal and J. Bhattacharya, Raman "Green" Spectroscopy for Ultrasensitive Analyte Detection, *Integrating Green Chemistry and Sustainable Engineering*, 2019, 165-190.

34 J. K. Patra, G. Das, L. F. Fraceto, E. V. R. Campos, M. del P. Rodriguez-Torres, L. S. Acosta-Torres, L. A. Diaz-Torres, R. Grillo, M. K. Swamy, S. Sharma, S. Habtemariam and H.-S. Shin, Nano based drug delivery systems: recent developments and future prospects, *J. Nanobiotechnology*, 2018, **16**, 71.

35 A. Samanta and I. L. Medintz, Nanoparticles and DNA-a powerful and growing functional combination in bionanotechnology, *Nanoscale*, 2016, **8**, 9037–9095.

36 G. Doria, J. Conde, B. Veigas, L. Giestas, C. Almeida, M. Assunção, J. Rosa and P. V. Baptista, Noble metal nanoparticles for biosensing applications, *Sensors*, 2012, **12**, 2, 1657–1687.

37 M. Holzinger, A. Le Goff and S. Cosnier, Nanomaterials for biosensing applications: A review, *Front. Chem.*, 2014, **2**, 63.

38 D. Zhang, G. Li and J. C. Yu, Inorganic materials for photocatalytic water disinfection, *J. Mater. Chem.*, 2010, **20**, 4529–4536.

39 M. A. Mahmood, S. Baruah, A. K. Anal and J. Dutta, Heterogeneous photocatalysis for removal of microbes from water, *Environ. Chem. Lett.*, 2012, **10**, 145–151.

40 J. Yang, B. Hou, J. Wang, B. Tian, J. Bi, N. Wang, X. Li and X. Huang, Nanomaterials for the removal of heavy metals from wastewater, *Nanomaterials*, 2019, **9**, 3, 424.

41 W. M. M. Mahmoud, T. Rastogi and K. Kümmerer, Application of titanium dioxide nanoparticles as a photocatalyst for the removal of micropollutants such as pharmaceuticals from water, *Curr. Opin. Green Sustain. Chem.*, 2017, **6**, 1–10.

42 S. Zhu and D. Wang, Photocatalysis: Basic principles, diverse forms of implementations and emerging scientific opportunities, *Adv. Energy Mater.*, 2017, **7**, 23, 1700841.

43 J. C. Scaiano and A. E. Lanterna, Is Single-Molecule Fluorescence Spectroscopy Ready to Join the Organic Chemistry Toolkit? A Test Case Involving Click Chemistry, *J. Org. Chem.*, 2017, **82**, 10, 5011–5019.

44 K. Zhang, J. Deng, Y. Liu, S. Xie and H. Dai, in *Semiconductor Photocatalysis - Materials, Mechanisms and Applications*, 2016, pp. 559–561.

45 K. Hashimoto, H. Irie and A. Fujishima, TiO_2 Photocatalysis: A Historical Overview and Future Prospects, *Jpn. J. Appl. Phys.*, 2005, **44**, 12, 8269–8285.

46 A. S. Hainer, J. S. Hodgins, V. Sandre, M. Vallieres, A. E. Lanterna and J. C. Scaiano, Photocatalytic Hydrogen Generation Using Metal-Decorated TiO_2: Sacrificial Donors vs True Water Splitting, *ACS Energy Lett.*, 2018, **3**, 3, 543–545.

47 T. Tong, A. Shereef, J. Wu, C. T. T. Binh, J. J. Kelly, J. F. Gaillard and K. A. Gray, Effects of material morphology on the phototoxicity of nano-TiO_2 to bacteria, *Environ. Sci. Technol.*, 2013, **47**, 21, 12486–12495.

48 M. R. D. Khaki, M. S. Shafeeyan, A. A. A. Raman and W. M. A. W. Daud, Application of doped photocatalysts for organic pollutant degradation - A review, *J. Environ. Manage.*, 2017, **198**, 78–94.

49 X. Yan, K. Yuan, N. Lu, H. Xu, S. Zhang, N. Takeuchi, H. Kobayashi and R. Li, The interplay of sulfur doping and surface hydroxyl in band gap engineering: Mesoporous sulfur-doped TiO_2 coupled with magnetite as a recyclable, efficient, visible light active photocatalyst for water purification, *Appl. Catal. B Environ.*, 2017, **218**, 20–31.

50 P. V. Kamat, Manipulation of charge transfer across semiconductor interface. A criterion that cannot be ignored in photocatalyst design, *J. Phys. Chem. Lett.*, 2012, **3**, 5, 663–672.

51 K. G. Stamplecoskie and J. C. Scaiano, Light emitting diode irradiation can control the morphology and optical properties of silver nanoparticles, *J. Am. Chem. Soc.*, 2010, **132**, 6, 1825–1827.

52 K. G. Stamplecoskie and J. C. Scaiano, Silver as an example of the applications of photochemistry to the synthesis and uses of nanomaterials, *Photochem. Photobiol.*, 2012, **88**, 4, 762–768.

53 A. L. Companion, in *Developments in Applied Spectroscopy*, 1965, pp. 221–234.

54 P. A. Hassan, S. Rana and G. Verma, Making sense of Brownian motion: Colloid characterization by dynamic light scattering, *Langmuir*, 2015, **31**, 1, 3–12.

55 J. Stetefeld, S. A. McKenna and T. R. Patel, Dynamic light scattering: a practical guide and applications in biomedical sciences, *Biophys. Rev.*, 2016, **8**, 4, 409–427.

56 L. K. McKenzie, H. E. Bryant and J. A. Weinstein, Transition metal complexes as photosensitisers in one- and two-photon photodynamic therapy, *Coord. Chem. Rev.*, 2019, **379**, 2–29.

57 M. Kasha, Characterization of electronic transitions in complex molecules, *Discuss. Faraday Soc.*, 1950, **9**, 14–19.

Chapter 2

Bacterial cells as SEDs for H_2 generation using $Pd@TiO_2$ photocatalyst

Introduction

2.1 Production of hydrogen for alternative fuel

Due to the current global energy problem, there has been an increasing interest in the exploration of clean alternative energy sources that are low in greenhouse gas (GHG) emissions in addition to being economically friendly.[1] One of the leading areas of research presently being explored is the use of renewable solar energy sources to produce chemical fuels; in particular, using photocatalytic materials that can use solar energy to split water and produce hydrogen with no GHG being emitted.[2] Since its initial discovery in 1972 by Fujishima and Honda, who reported the use of solar energy to produce hydrogen by means of a TiO_2 electrode, the use of semiconducting photocatalysts as a sustainable treatment in the production of green energy has been widely investigated.[3] Semiconductor based photocatalysts will absorb irradiated light, either in the UV and/or the visible spectral region, and subsequently, go into a photoexcited state where the electrons from the valence band (VB) are promoted to the conduction band (CB). This creates hole- (h^+) electron (e^-) pairs, as shown in Scheme 2.1.[4,5] The energy difference between the valence band and the conduction band is referred to as the band gap (E_b) of the semiconductor.

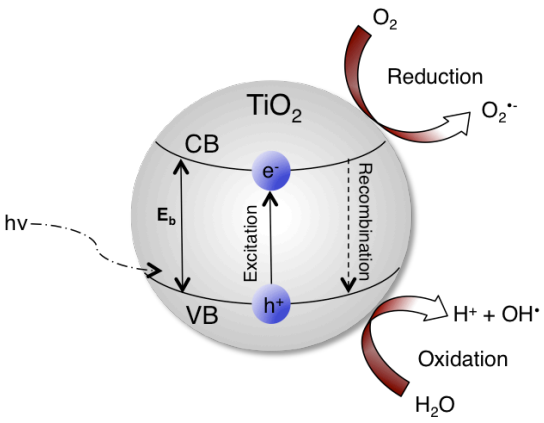

Scheme 2.1. Electron-hole pair formation in a TiO_2 semiconductor.

Once in the excited state, the electron and hole can migrate to the surface of the catalyst where water can be split through the reduction and oxidation of water to produce H_2 and O_2 respectively. However, development of highly efficient phototcatalytic H_2 evolution systems is limited by the strict requirements placed on the photocatalyst for a one- step water splitting reaction. This includes the photocatalyst having to contain an appropriate thermodynamic potential for water splitting, a band gap that is narrow enough to absorb visible photons and be photostable.[6]

The application of metal oxides, such as pure TiO_2, as the photocatalyst in the water-splitting reaction is not ideal for solar applications due to the large band gap of this semiconductor (anatase, 3.2 eV) that limits the absorption of light to the UV range, which only accounts for a small fraction of the incoming solar energy and can make this process less efficient. A possible solution to overcome this issue is to dope the semiconducting material with different elements, ranging from transition metals to non-metallic elements, which allows for the photocatalyst to absorb lower energetic wavelengths found in the visible region of the solar spectrum.[7,8] Deposition of metal nanoparticles (NPs) onto a semiconductor support improves the efficiency by affecting the systems energetics and facilitating light induced charge separation at the interface of the semiconductor. [9–11] Despite all the efforts done to extend the absorption profile of the semiconductor materials into the visible region, as well as, increasing the

electron-hole pair lifetime, creating a photocatalyst that can split pure water into stoichiometric amounts of hydrogen and oxygen using the solar spectrum in sufficient capacity still remains very challenging.[2,8]

2.2 Uses of Sacrificial Electron Donors (SEDs) for the production of H_2

To improve the H_2 generation efficiency many have adopted the use of sacrificial electron donors (SEDs), which can act as a hole trap and prevent the rapid recombination of the charge carriers.[12] The use of hole scavengers to improve the H_2 generation is frequently criticized because the SED used can be an expensive chemical reagent and/or can potentially form by-products that no longer make this a source for clean, renewable fuel.

Our group previously investigated the rate of hydrogen production, where they compared the efficiencies of different catalysts under conditions of true water splitting and in the presence of sacrificial organic electron donors.[13] H_2 production of TiO_2-based catalysts were decorated with various metal nanoparticles were evaluated either under true water splitting conditions (absence of a SED) or against common SED-assisted approaches (organic sacrificial donors such as methanol or formic acid).[14,15]

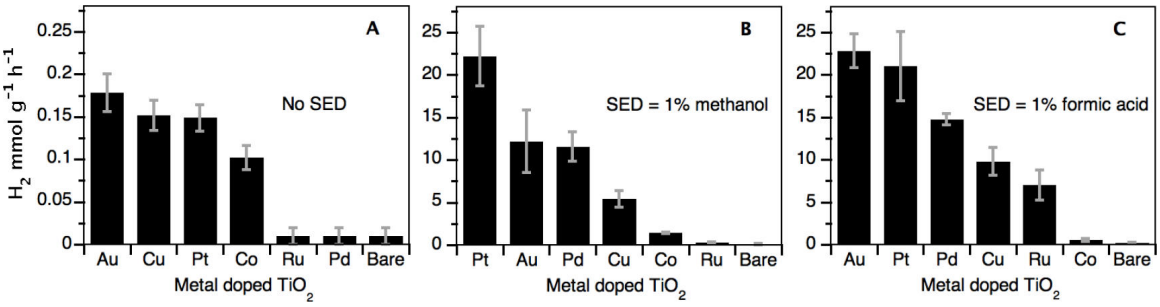

Figure 2.1. The rate of H_2 production using varying catalysts for the following conditions: (A) true water splitting, (B) in the presence of 1% methanol, and (C) in the presence of 1% formic acid (pH ≈ 2.2) using 368 nm irradiation (0.33 W cm^{-2}). Reproduced with permission from A. S. Hainer *et al.*[13] Copyright (2018) American Chemical Society.

As was predicted, the rates of H_2 generation with the use of a SEDs were greater than those under water splitting conditions, as shown in Figure 2.1. The efficiency of the photocatalytic H_2 production were almost two orders of magnitude greater when using SED compared to the condition absent of SEDs.[13]

These results demonstrated that efficiency of the H_2 evolution of a catalyst could also vary depending the co-catalyst dopant. For example, the Co doped particle does not produce an H_2 in the presence of formic acid (1%) and very little in methanol (1%) whereas, in the absence of a SED close to 0.1 mmol/g/h of hydrogen was generated. Another example is that the ruthenium based catalysts only produced H_2 in the presence of formic acid.

Additionally, these findings highlight the low effectiveness of photocatalytic H_2 generation by means of splitting without a hole scavenger, with H_2 production without a donor being a fraction as efficient as using a popular organic donor. Rather than vilify the use of chemical SEDs for the H_2 production, authors noted that if the organic molecule sacrificed for hydrogen generation was low value product, such as a pollutant naturally found in water, the use of a SED could reap more benefits than true water splitting alone. Thus, pollutants, including microbes or pharmaceutical contaminants, could be used as SEDs by the catalyst to produce hydrogen more efficiently while simultaneously being destroyed.[7] As shown in Scheme 2.2, the pollutant (microorganism or other organic material) can act as the SED to help slow the electron-hole recombination and be oxidized in the process. Moreover, under aqueous conditions, hydroxyl radicals (OH•) are created and can further react with more organic materials and further degrade the undesired contaminants.[16,17] Additionally, the presence of oxygen will also slow the recombination rate of the electron-hole pair, which allows for the formation of the superoxide radical anion ($O_2^{\bullet -}$) that can form other radical species that will interact with biological and organic pollutants and lead to destroyed oxidized products. These photogenerated reactions allow for the opportunity to study the photocatalysts ability to simultaneously decontaminate

water while creating H_2 using organic pollutants found in aquatic systems rather than using the valuable molecules commonly studied as SED.

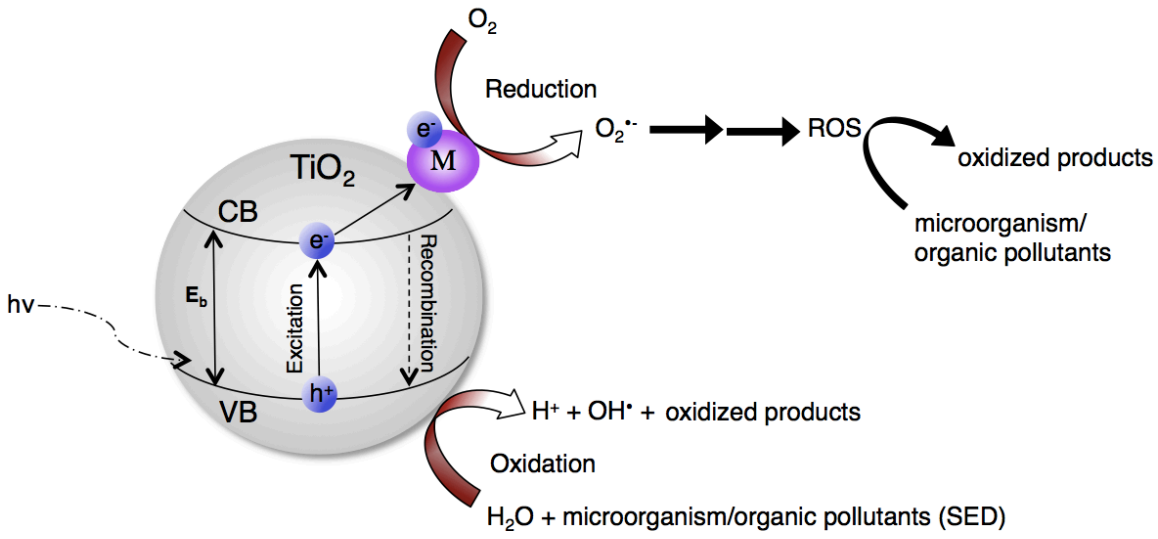

Scheme 2.2. Diagram illustrating the photocatalysis of TiO_2 under air, with the presence of biological and organic pollutants.

Heterogeneous photocatalysts are a more suitable choice for water remediation than homogeneous materials as they can be more easily removed from the aqueous environment. In particular, anatase TiO_2 has been the focus of much of this research because it is an inexpensive, photostable and active compound.[18] Titania nanoparticles are also heavily researched as they have a broad spectrum of toxicity against a number of microorganisms, including gram-positive and gram-negative bacteria. The formation of the aforementioned hydroxyl radicals and other reactive species ($O_2^{\bullet -}$, ROS) in an aquatic environment can cause photo-destruction of these microorganisms and other cell cultures. While there is still some debate on the mechanism behind the bactericidal activity of TiO_2, one well studied area is inactivation through oxidative attack on the outer/inner cell membrane of the microbe.[19,20] Other possible routes for cell death by titania based nanomaterials includes the alteration of a cells coenzyme A-dependent enzymatic activities and DNA damage caused by the production of hydroxyl radicals.[21] The diverse range of mechanisms for cell

deactivation makes TiO_2 and its derivatives a leading choice for the destruction of water contaminants, particularly microorganisms.

2.3 Bacterial cell structures

There are two main classifications that are used to differentiate bacterial cells based on their cell wall structure: gram- negative and gram- positive. Gram-positive cell walls are composed of a thick layer of peptidoglycan, which differs from the gram- negative bacterial wall that is composed of a thin layer of peptidoglycan surrounded by an additional outer layer of lipopolysaccharide. Damage to the organic layer can occur when metal nanoparticles are introduced to the bacterial environment and there is a physical interaction between the NPs and the microorganism. It has been said to be more detrimental for gram-negative species due to their lack of thick peptidoglycan wall that can possibly act as a protective layer for gram-positive bacteria.[22]

Exploring the use of aquatic contaminants, particularly bacterial cells, as sacrificial electron donors for the simultaneous production of hydrogen and degradation of pollutants by means of heterogeneous photocatalysis is the inspiration behind this project. Here, we investigate the formation of hydrogen using $Pd@TiO_2$ nanoparticles in the presence of gram-negative bacteria, *Escherichia coli (E. coli)*. We expect TiO_2 nanoparticles to be able to produce H_2 while eliciting microbial death when subjected to simulated solar light.

In the previous work using the $Pd@TiO_2$ nanomaterial for non hydrogen-mediated hydrogenation or isomerization of benzyl substituted alkenes, found that the heterogeneous material could easily be recovered with centrifugation.[23] This is important because if we want to create a flow system using these nanomaterials for oxidative destruction of microorganisms while simultaneously generating photocatalytic H_2, the material should able to be separated from the aqueous media.

Also, as the intended use of the photocatalyst is for water remediation in either a batch or a flow system, it would be ideal that they have some capacity to eradicate potential biofilms that can form within the system.

In addition to recovering the catalyst, an advantageous attribute for a heterogeneous material to have is to be reusable and efficient after multiple cycles. These characteristics can give heterogeneous material a slight advantage over its homogenous counterpart. This is an important feature for applications in industry because reusability of the catalyst can lower the cost of operation, as the catalyst would not have to be changed after every cycle. Previous work regarding the reusability and efficiency of the Pd@TiO_2 has been mixed, depending on the reaction being catalyzed. It was found that the Pd@TiO_2 catalyst for the heterogeneous Ullman cross-coupling reaction using mixed light was able to retain 100% conversion after 4 cycles and had high selectivity towards the desired cross-coupled product for at least 3 cycles.[24] However, it was also found that for Sonogashira C-C coupling, the Pd@TiO_2 nanoparticles could be reused twice with good performance but the activity drop substantially dropped after the second cycle. They found no evidence of Pd leaching from the catalyst through ICP-OES analysis and believe that the alkyne hydrogenation products had accumulated on the surface of the catalyst, which had likely poisoned it.[25] Therefore, the reusability of the palladium nanoparticles is dependent on the reaction and has potential for being suitable heterogeneous catalyst for water remediation as it can be readily recovered and has better catalyst longevity than its homogeneous counterpart.

2.4 Materials and Methods

Reagents. All chemicals were purchased from Sigma-Aldrich, unless specified otherwise. TiO_2 P25 was purchased from Univar Canada.

Synthesis of palladium-decorated nanoparticles

Synthesis of palladium supported on TiO_2 was prepared using a photodeposition method of PdNPs onto TiO_2 (P25) previously reported by the Scaiano group.[23] Briefly, TiO_2 (500 mg) and $PdCl_2$ (22 mg) were dispersed into a solution of 200 ml of Milli-Q water and subsequently sonicated for 10 minutes. The mixture was irradiated in a photoreactor equipped with 14 UVA bulbs for 8 hours while vigorously stirring. The resulting slurry was centrifuged and washed by centrifugation three times to remove any unreacted $PdCl_2$. Catalysts were placed in a desiccator under vacuum overnight to dry. Characterization of nanoparticles has been previously done in the group by TEM, XPS, ICP-EOS and DRS. The loading of Pd onto the TiO_2 was found to be 2% metal loading (w/w) and particles are ~1.6 nm in size.[23]

Photo-induced hydrogen generation

In a vial, 5 mg of the catalyst was suspended in 4 ml of Milli-Q water alone or a solution of Milli-Q and *E. coli*. Samples were degassed with argon under vacuum, sealed and irradiated in a Luzchem SolSim photoreactor that provides solar simulated light using a 300W ceramic Xe lamp (Figure 2.2) while vigorously stirring for 4 h. Each experiment was conducted in duplicate.

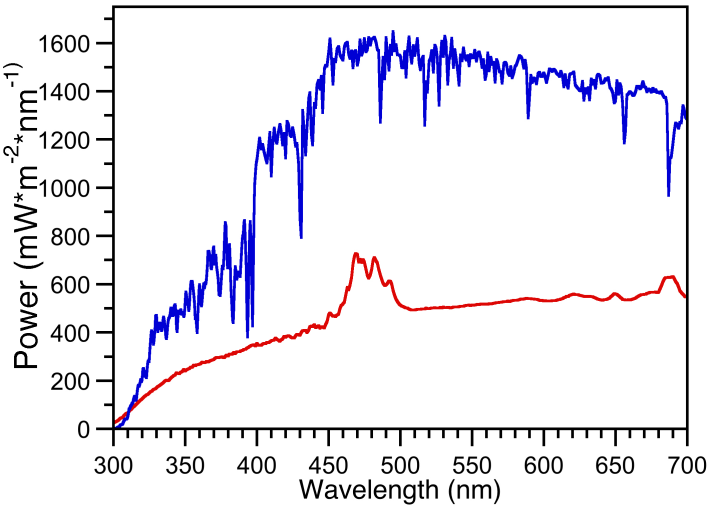

Figure 2.2. Emission spectrum of the solar spectrum AM1.5 (blue) and Xenon lamp emission using 305 nm filter (red).

Hydrogen detection

The production of H_2 was quantified through the analysis of 1 mL of gas sample from each vial and running it through a previously calibrated GC-TCD instrument. A separatory funnel was filled with distilled water while ensuring there was no air bubbles inside then was secured in a glass container that was filled one third of the way with water. Pure H_2 gas was injected through a septum at the top of the funnel and then equilibrated with atmospheric pressure. Then 6 mL vials were filled with distilled water (4 mL) under Argon atmosphere. To each vial, a known amount of H_2 gas was added to run a calibration curve containing 0.02 – 2 mL of H_2. After allowing time for the gases to equilibrate within the vials' headspace, 1 mL of gas sample from each vial was analyzed using GC-TCD.

Preparation of *E.coli*

One colony of *Escherichia coli* CF073 was picked from an agar plate and grown overnight in 2 mL of Luria-Bertani broth (LB) and washed with sterile Milli-Q by centrifugation at 1500 rpm for 10 min at 22 °C and then re-suspended in 10 mL sterile Milli-Q (or a different media if indicated otherwise). Bacterial cultures in concentrations of $1x10^8$ CFU/ mL were used.

2.5 Results and Discussion

In order to see any H_2 production using bacterial culture, experiments were conducted using *E. coli* concentrations that far exceed any amount that would be found in different bodies of water (ocean, lake, river, etc.). The limit of detection (LOD) for the H_2 is 5.53 µmol and the limit of quantification (LOQ) is 16.75 µmol, therefore a very high concentration of bacterial species was used. The concentration of *E. coli* varies immensely from area to area. Health Canada's recommended microbiological guideline determines that the quantification of *E. coli* coliforms can be used as an indicator of recreational water quality for fresh water. The standard values of this guideline for fresh water are 200 *E. coli* per 100 mL or 200 fecal coliforms per 100 mL, where over 90% of the fecal coliforms are *E. coli*.[26] A 2018 study testing different water sources in Isiolo County, Kenya found *E. coli* present in a multitude of water sources, where the mean *E. coli* microbial count in tap was 6 CFU/ mL and the highest mean count for contamination were 160 CFU/ mL in rain water.[27] These concentrations are too small to detect or quantify the production of H_2, therefore suspensions containing 10^8 CFU/ mL of bacteria were used to ensure we can see the H_2 generated. This is demonstrated in Figure 2.3, where the concentration deemed 'unacceptable' by Health Canada produced a very minimal amount of hydrogen. The reason for the small amounts of hydrogen produced by these 2 samples can be due to the fact that sterile saline (0.9% NaCl) was used rather than sterile Milli-Q water. Saline solution produces as small amount of H_2 alone, as seen in Figure 2.4, but was not a significant value meaning that the small amount of H_2 produced by 2 CFU/ mL could be due to the bacteria, the saline solution or a combination of the two. Salt can deposit on the catalyst over time and possibly affect its photocatalytic abilities; therefore, saline solution was only used with small concentrations of bacterial cells. Saline solution was chosen to prevent premature cell death of the SEDs at low concentrations. This is because Milli-Q water is a hypotonic solution that could make the cells swell due to the lower

solute concentration in the solution. Using saline ensures that the cells were alive at the beginning of the reaction in the SolSim.

As shown in Figure 2.3, the sample containing a higher concentration of *E. coli* ($1x10^8$ CFU/ mL) was the only sample to produce a significant amount of H_2. This demonstrates that a high concentration of bacterial cells is necessary to produce a detectable and quantifiable amount of H_2.

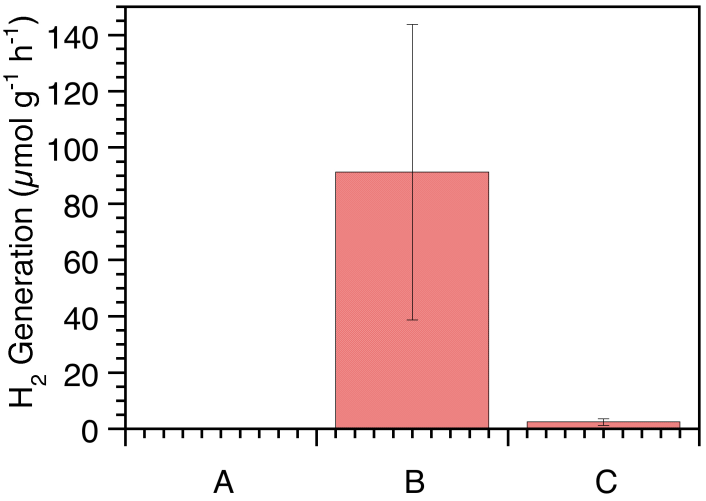

Figure 2.3. H_2 generation rates under solar simulated radiation containing A) No *E.coli,* B) *E.coli* and C) *E. coli* (2 CFU/mL) in the presence of Pd@TiO_2.

E. coli was initially chosen to be the SED because preliminary studies using samples of water from various sources in the local area determined that *E. coli* was the bacterial species that was most prevalent in the water samples.

Palladium was chosen as the co-catalyst for the H_2 generation reaction using biological matter as SEDs. Previous results using this photocatalyst found that under 368nm UVA LED irradiation, Pd@TiO_2 did not produce any H_2 (within experimental error) in the absence of a SED (Figure 2.1). Since Pd@TiO_2 does not generate any photocatalytic H_2 in water, we can assume that H_2 produced can be attributed to the SED present in the reaction.

Besides Pd@TiO_2, Ru@TiO_2 and bare TiO_2 also did not produce any H_2 in the absence of an SED. However, Ruthenium produced no H_2 in the presence of methanol and low amounts of H_2 in the presence of formic acid compared to the other photocatalysts. Bare TiO_2 did not produce H_2 in the presence nor the absence of a SED. Due to the low amount of H_2 generated by Ru@TiO_2 and bare TiO_2, we chose to focus on the Pd@TiO_2 for this set of experiments. These conditions allow for us to safely determine that if H_2 is produced it is due to the biological organic matter and not the water.

Three different sterile media were investigated for the production of H_2 in the presence of only the Pd@TiO_2 catalyst. The solvent choice for this reaction is important as any additional components can act as an SED and could form H_2 independent from the biological material. As was expected, the sterilized Milli-Q samples (H_2O in Figure 2.4) produced zero hydrogen under the conditions studied, similar to the initial findings by Hainer et al.[13] In contrast to these results, the solution that contained 10% (v/v) LB broth in sterile Milli-Q with the catalyst produced a small quantity of H_2, as shown in Figure 2.4, which can be attributed to the nutrient rich composition of the LB which contains a mixture of peptides, yeast and NaCl which are capable of acting as organic sacrificial donors without the presence of the bacteria.[28] The rate of H_2 production was also examined in a saline solution (0.9% NaCl) providing an isotonic environment that supports cell viability. Although the saline solution appeared to produce a slight amount of hydrogen it is still within experimental error. To ensure that the only component in the samples that can produce hydrogen is the bacterial cell; sterile H_2O was used as the solvent, unless indicated otherwise.

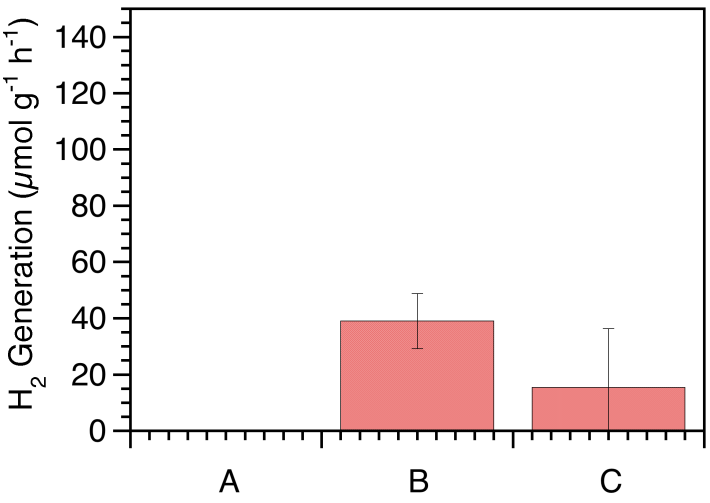

Figure 2.4. H_2 generation rates in the presence the Pd@TiO_2 in either A) Milli-Q, B) 10% (v/v) LB and C) 0.9% NaCl solution in Milli-Q under solar simulated radiation.

A control experiment was conducted to determine if the production of H_2 could only be achieved in the presence of both the Pd@TiO_2 NPs (catalyst) and the *E. coli* bacterial cells (sacrificial donor) under solar simulated irradiation. When either the catalyst or the SED is absent, there is no evident production of hydrogen. When the Pd@TiO_2 catalyst is compared to the use of the semiconductor alone (TiO_2), the rate production of production is approximately 7x higher (Figure 2.5), which fits with what is stated in the literature about how metal decorated TiO_2 can slow down the recombination rate of the hole-electron pair and capture the electrons to allow more time for the reduction of the H^+ to H_2 at the surface of the metal.[29]

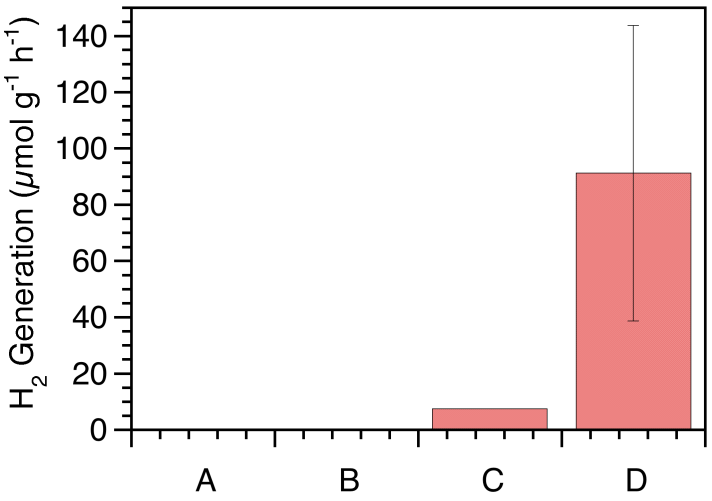

Figure 2.5. H_2 generation rates under solar simulated radiation of samples containing A) No catalyst B) No *E. coli* C) TiO_2 and D) Pd@TiO_2 in the presence of *E. coli* in Milli-Q.

Previous reports on the use of Pd@TiO_2 for the production of H_2 were all done under argon due to the fact that under air, the presence of oxygen can trap electrons faster than the H^+ and produce reactive oxygen species (ROS).[30] Results from the experiments conducted under air versus argon reflect this hypothesis; samples containing the Pd@TiO_2 and concentrated *E. coli* that were suspended in MilliQ water and irradiated under air produced no hydrogen whereas the inert conditions did produce H_2 (91.23± 52.52 μmol/g/h), demonstrating that the presence of oxygen can inhibit the photocatalytic reaction.

Under dark conditions, there should be no production of hydrogen, as there is no expected photoactivity caused by the semiconductor and consequently no photo-induced redox reactions. This theory is reflected in the experimental results where under dark conditions, in the presence and absence of the Pd@TiO_2 catalyst, there was no observed production of hydrogen, whereas under solar simulated irradiation in the presence of the photocatalyst, H_2 production was observed as seen in Figure 2.6.

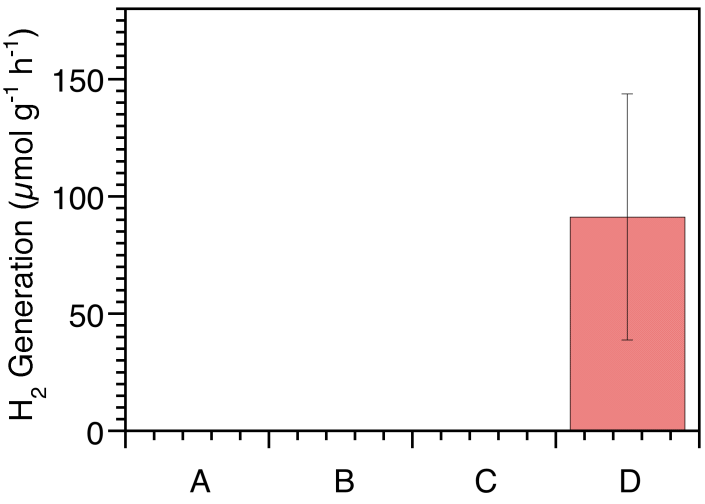

Figure 2.6. H_2 generation rates using Pd@TiO_2 under dark conditions where *E. coli* is A) absent and B) present in sterile Milli-Q, compared to H_2 generation rates using Pd@TiO_2 under simulated solar radiation where *E. coli* is C) absent and D) present in sterile Milli-Q.

2.6 Conclusion

We were able to determine that the rate of H_2 generation observed is dependent upon the presence of the heterogeneous photocatalyst (Pd@TiO_2) and that debris derived from the cells can act as a sacrificial donor facilitating the generation of H_2 when irradiated under solar light. This has the potential application to generate H_2 while cleaning water.

2.7 Future Work

Future work in the study of metal-doped nanoparticles in the production of hydrogen will involve the exploration of using different metals, particularly those that are more inexpensive and earth abundant. Currently, all of our assessments of hydrogen production using a water splitting reaction are conducted in a batch method, where vials containing the solutions are measured individually. For a more practical application of this nanomaterial, a flow system would allow for the continuation of the production of green energy and the treatment of polluted water. It would also be intriguing to compare the experimental results of the hydrogen production rates using other organic pollutants, such as

pharmaceuticals or hormones, found in local bodies of water to determine whether contaminants can contribute to efficient H_2 production.

References

(1) Xiang, Q.; Yu, J.; Jaroniec, M. Graphene-Based Semiconductor Photocatalysts. *Chem. Soc. Rev.* 2012, **41**, 782–796.

(2) Chen, X.; Shen, S.; Guo, L.; Mao, S. S. Semiconductor-Based Photocatalytic Hydrogen Generation. *Chem. Rev.* 2010, **110**, 11, 6503–6570.

(3) Fujishima, A.; Honda, K. Electrochemical Photolysis of Water at a Semiconductor Electrode. *Nature* 1972, **238**, 37–38.

(4) Bodzek, M.; Rajca, M. Photocatalysis in the Treatment and Disinfection of Water. Part I. Theoretical Backgrounds. *Ecol. Chem. Eng. S* 2012, **19**, 629–638.

(5) Mapukata, S.; Hainer, A. S.; Lanterna, A. E.; Scaiano, J. C.; Nyokong, T. Decorated Titania Fibers as Photocatalysts for Hydrogen Generation and Organic Matter Degradation. *J. Photochem. Photobiol. A Chem.* 2020, **388**, 112185.

(6) Maeda, K.; Domen, K. Photocatalytic Water Splitting: Recent Progress and Future Challenges. *J. Phys. Chem. Lett.* 2010, **1**,18, 2655–2661..

(7) Lusvardi, G.; Barani, C.; Giubertoni, F.; Paganelli, G. Synthesis and Characterization of TiO_2 Nanoparticles for the Reduction of Water Pollutants. *Materials (Basel).* 2017, **10**, 1208.

(8) Zou, Z.; Ye, J.; Sayama, K.; Arakawa, H. Direct Splitting of Water under Visible Light Irradiation with an Oxide Semiconductor Photocatalyst. *Nature* 2001, **414**, 625–627.

(9) Plante, I. J. La; Habas, S. E.; Yuhas, B. D.; Gargas, D. J.; Mokari, T. Interfacing Metal Nanoparticles with Semiconductor Nanowires. *Chem. Mater.* 2009, **21**, 15, 3662–3667.

(10) Banin, U.; Ben-Shahar, Y.; Vinokurov, K. Hybrid Semiconductor-Metal Nanoparticles: From Architecture to Function. *Chem. Mater.* 2014, **10**, 99.

(11) Subramanian, V.; Wolf, E.; Kamat, P. V. Semiconductor-Metal Composite Nanostructures. To What Extent Do Metal Nanoparticles Improve the Photocatalytic Activity of TiO_2 Films? *J. Phys. Chem. B* 2001, **105**, 46, 11439–11446.

(12) Schneider, J.; Bahnemann, D. W. Undesired Role of Sacrificial Reagents in Photocatalysis. *J. Phys. Chem. Lett.* 2013, **4**, 2, 3479–3483.

(13) Hainer, A. S.; Hodgins, J. S.; Sandre, V.; Vallieres, M.; Lanterna, A. E.; Scaiano, J. C. Photocatalytic Hydrogen Generation Using Metal-Decorated TiO_2: Sacrificial Donors vs True Water Splitting. *ACS Energy Lett.* 2018, **3** 3, 543–545.

(14) Chen, W. T.; Chan, A.; Al-Azri, Z. H. N.; Dosado, A. G.; Nadeem, M. A.; Sun-Waterhouse, D.; Idriss, H.; Waterhouse, G. I. N. Effect of TiO_2

Polymorph and Alcohol Sacrificial Agent on the Activity of Au/TiO_2 Photocatalysts for H2 Production in Alcohol-Water Mixtures. *J. Catal.* 2015, **329**, 499–513.

(15) Liu, H.; Yuan, J.; Shangguan, W. Photochemical Reduction and Oxidation of Water Including Sacrificial Reagents and Pt/TiO_2 Catalyst. *Energy and Fuels* 2006, **20**, 6, 2289–2292.

(16) Elhage, A. A.; Scaiano, J. C.; Lanterna, A. E. Dressing up for the Occasion: The Many Faces of Decorated Titanium Dioxide in Photocatalysis. In *Photoactive Inorganic Nanoparticles: Surface Composition and Nanosystem Functionality*; 2019; pp 78–108.

(17) Dong, H.; Zeng, G.; Tang, L.; Fan, C.; Zhang, C.; He, X.; He, Y. An Overview on Limitations of TiO_2-Based Particles for Photocatalytic Degradation of Organic Pollutants and the Corresponding Countermeasures. *Water Res.* 2015, **79**, 128–146.

(18) Lettmann, C.; Hinrichs, H.; Maier, W. F. Combinatorial Discovery of New Photocatalysts for Water Purification with Visible Light. *Angew. Chemie - Int. Ed.* 2001, **40**, 17, 3160–3164.

(19) Foster, H. A.; Ditta, I. B.; Varghese, S.; Steele, A. Photocatalytic Disinfection Using Titanium Dioxide: Spectrum and Mechanism of Antimicrobial Activity. *Appl. Microbiol. Biotechnol.* 2011, **90**, 6, 1847–1868.

(20) Kiwi, J.; Nadtochenko, V. Evidence for the Mechanism of Photocatalytic Degradation of the Bacterial Wall Membrane at the TiO_2 Interface by ATR-FTIR and Laser Kinetic Spectroscopy . *Langmuir* 2005, **21**, 10, 4631–4641.

(21) Kubacka, A.; Diez, M. S.; Rojo, D.; Bargiela, R.; Ciordia, S.; Zapico, I.; Albar, J. P.; Barbas, C.; Martins Dos Santos, V. A. P.; Fernández-García, M.; et al. Understanding the Antimicrobial Mechanism of TiO_2 -Based Nanocomposite Films in a Pathogenic Bacterium. *Sci. Rep.* 2014, **4**, 1–9.

(22) Slavin, Y. N.; Asnis, J.; Häfeli, U. O.; Bach, H. Metal Nanoparticles: Understanding the Mechanisms behind Antibacterial Activity. *J. Nanobiotechnology* 2017, **15**, 65.

(23) Elhage, A.; Lanterna, A. E.; Scaiano, J. C. Tunable Photocatalytic Activity of Palladium-Decorated TiO_2: Non-Hydrogen-Mediated Hydrogenation or Isomerization of Benzyl-Substituted Alkenes. *ACS Catal.* 2017, **7**, 1, 250–255.

(24) Marina, N.; Lanterna, A. E.; Scaiano, J. C. Expanding the Color Space in the Two-Color Heterogeneous Photocatalysis of Ullmann C-C Coupling Reactions. *ACS Catal.* 2018, **8,** 8, 7593–7597.

(25) Elhage, A.; Lanterna, A. E.; Scaiano, J. C. Light-Induced Sonogashira C-C Coupling under Mild Conditions Using Supported Palladium Nanoparticles. *ACS Sustain. Chem. Eng.* 2018, **6**, 2, 1717–1722.

(26) Lévesque, B.; Gauvin, D. Microbiological Guideline Values for Recreational

Bathing in Canada: Time for Change? *Can. J. Infect. Dis. Med. Microbiol.* 2007, **18,** 2, 153–157.

(27) Onyango, A. E.; Okoth, M. W.; Kunyanga, C. N.; Aliwa, B. O. Microbiological Quality and Contamination Level of Water Sources in Isiolo County in Kenya. *J. Environ. Public Health* 2018, 1–10.

(28) Sezonov, G.; Joseleau-Petit, D.; D'Ari, R. Escherichia Coli Physiology in Luria-Bertani Broth. *J. Bacteriol.* 2007, **190**, 23, 8746–8749.

(29) Hainer, A.; Marina, N.; Rincon, S.; Costa, P.; Lanterna, A. E.; Scaiano, J. C. Highly Electrophilic Titania Hole as a Versatile and Efficient Photochemical Free Radical Source. *J. Am. Chem. Soc.* 2019, **141**, 11, 4531–4535.

(30) Li, Y.; Lu, G.; Li, S. Photocatalytic Hydrogen Generation and Decomposition of Oxalic Acid over Platinized TiO_2. *Appl. Catal. A Gen.* 2001, **214**, 2, 179–185.

Chapter 3

Water purification using porphyrin attached to glass wool for potential flow system applications

Introduction

3.1 Water treatment and current system used

As the Earth's population continues to grow, we increase the production and release of harmful contaminants into the planet's water resources. Water pollution can come in many forms, from toxic chemicals to the presence of dangerous pathogens that stem from a myriad of different sources. High aquatic pollution can not only have a direct negative effect on the health of the surrounding community but it can also have lasting secondary effects that are equally as devastating. The consequences from water contamination can extend from the toxicity that harms aquatic and mammalian life to the negative impact on the financial state of a populace due to the decline in many recreational activities.[1] Moreover, the resulting treatment of these polluted bodies of water often requires very costly treatment methods that can further impact the society's economy, particularly in developing countries that have limited access to clean and safe natural water resources.[2] Common water remediation methods begin with the use of a mechanical approach, such as sedimentation, filtration or some sort of membrane technology; these however, are quite costly to operate and maintain.[3] The secondary treatment is the use of chemical disinfectants. Chlorination is a common disinfectant treatment used to treat microbial contaminants in drinking water, however, the disinfectant by-products (DBPs) that are generated by chlorination have been found to possibly be mutagenic and carcinogenic.[4,5] Therefore, the development of inexpensive, safe and environmentally friendly purification methods is highly desirable.

A recently explored alternative to the current strategies implemented to clean water is the use of photocatalytic disinfection. This approach requires three components: a photosensitizer (PS), a light source and molecular oxygen. Photocatalytic disinfection has garnered a great deal of interest because each of these elements are essentially harmless to the natural environment individually.[6,7] Upon light irradiation, the PS can produce reactive oxygen species (ROS) in the presence of oxygen, such as singlet oxygen or the hydroxyl radical species, which are cytotoxic to unwanted microorganisms, including bacteria, fungi and viruses.[8,9] Photosensitizers can experience two different pathways when photo-excited, which are termed the Type I and Type II reactions. The mechanism for the Type I reaction occurs when there is a direct interaction between the PS and substrate (bio-organic molecule) leading to the formation of active free radicals and radical ions. The Type II reaction is mediated by the transfer of energy from the photosensitizer to the ground state oxygen ($^3O_2$) generating an excited singlet state of oxygen (Figure 3.1).[10,11]

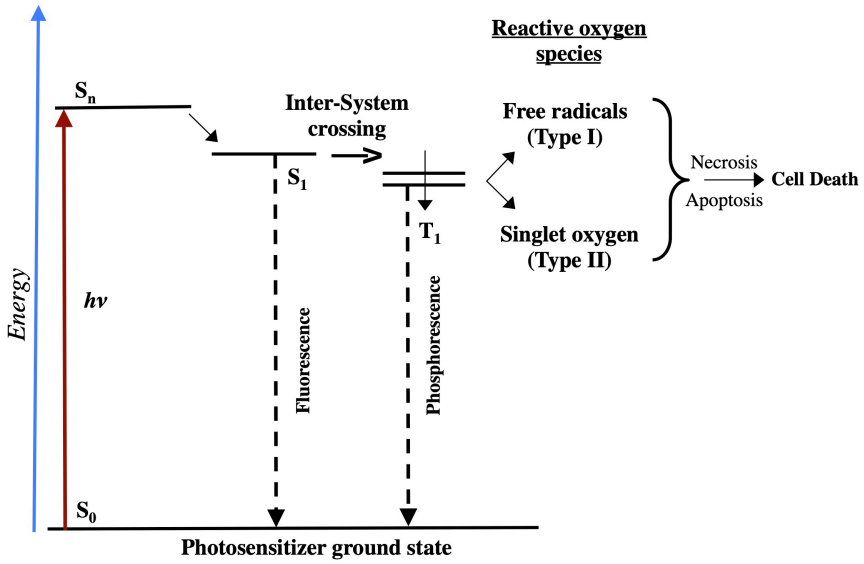

Figure 3.1. Jablonski diagram of photosensitization.

3.2 Porphyrins as photosensitizers for water remediation

Photosensitizers have a tendency to have low biodegradability and/or have high chemical stability that makes them an attractive potential for the removal of bioorganic pollutants. Porphyrins are a type of photosensitizer that have historically been investigated for photodynamic therapy (PDT) due to their selectivity and successful destruction of malignant cells. Porphyrin–based PSs have negligible toxicity under dark but when illuminated with light of the appropriate wavelength, the PSs can accumulate in the cell and elicit a toxic response. Moreover, they have a high extinction coefficient and can strongly absorb light in the visible region to produce radicals, whereas most photocatalytic compounds require UV light.[12,13] Upon the absorption of a photon of light, the ringed structure of the porphyrin can undergo either the Type I or Type II reaction, which will prompt the porphyrin to go into an excited singlet state and undergo intersystem crossing into the excited triplet state. Once in the photo-excited triplet state, the molecule can produce radicals through different pathways. The pathway often utilized for PDT is through the production of the reactive singlet oxygen. Photoexcited porphyrins can also generate other reactive species including hydroxyl radicals by reacting with water, superoxide ions and biomolecule radicals (Figure 3.2).

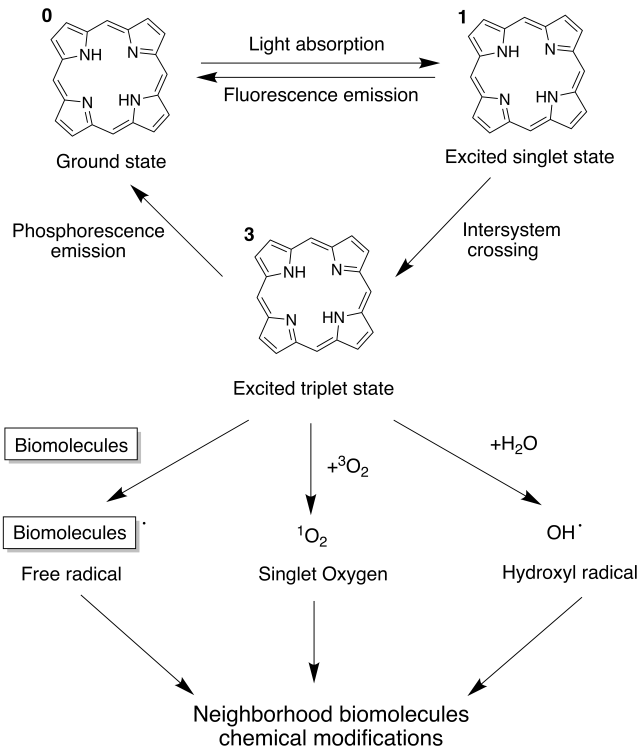

Figure 3.2. Porphyrin photochemical reactions responsible for the generation of free radicals and singlet oxygen in a biological system. Repodruced from Z. Malik *et al.*[14] Copyright (1990) Elsevier, Journal of Photochemistry and Photobiologi B: Biology.

3.3 Challenges of using porphyrins for water remediation

The application of porphyrin-based photosensitizers has been extensively explored for PDT-related studies, however, there are few reports examining their possible application in water remediation. This could be due to the fact that most of the characteristics that make a porphyrin an ideal PDT treatment candidate may be disadvantageous for water treatment.

One important characteristic of a porphyrin for PDT is the molecules solubility in solution and its ability to enter the cell and cause damage to different internal components; for example, the molecule could interact with, and cleave, the hosts DNA through the formation of singlet oxygen.[15] However, using a homogenous photocatalyst would make it difficult to apply them to water remediation since their separation from an aquatic system would produce a

process that is tedious and expensive.

Of the few studies focused around porphyrin use for water remediation, the majority focuses on the attachment of a cationic porphyrin onto support. The reason for this is because the positive charge will enable the interaction between the positively charged porphyrin and negatively charged cell wall. An example of this is by Mbakidi *et al.,* where they attached a tricationic porphyrin to a cellulosic support and tested its antimicrobial response against *Staphylococcus aureus* and *Escherichia coli* under visible light irradiation. Although there does seem to be potential for the application of cationic porphyrins for water purification, this application can be limited by the low yield generated of desired porphyrin product during synthesis.

The Adler-Longo method has been widely used for meso-substituted porphyrin synthesis because it can generate a greater yield of meso-substituted porphyrins than the competing Rothemund method and under milder conditions: ~20% yield over the ≤10% afforded by the latter method.[16,17] A more recent synthetic strategy for porphyrins, called the Lindsey method, has been developed to allow for larger scaled reactions.[18] However, the sacrifice for the higher yield is the need of an inert atmosphere, large diluent agents and the use of expensive quinones that significantly increases the cost and harsh conditions of porphyrin synthesis.[19,20]

Targeting gram-negative bacteria can be difficult because their outer cell membrane contains a thick peptidoglycan layer that limits the permeability of the PSs into the cell. The interaction between the PS and the gram-negative bacteria must be facilitated either by the presence of a membrane disrupting molecule (such as EDTA) or a PS that contains a positive charge that displace the cations and result in the rearrangement of the imbedded lipopolysaccharides which will alter the cell wall barrier properties.[6]

One possible solution for overcoming the limitation of using a homogeneous organic photocatalyst for water remediation is supporting it on

heterogeneous material. This would facilitate the recovery and reusability of the photocatalyst while minimizing the loss of the PSs catalytic properties.

The goal of this project was to develop a purification method that can be implemented into a flow system for photoactivated purification of the water. Previously, our group immobilized various metal and metal oxides onto glass wool (GW). [21,22] Glass wool is inexpensive, inert and readily available with a high surface area that is easy to modify. For these reasons, glass wool was chosen as a support for heterogeneous catalysis.

Here we explore the use of glass wool as inert support for a series of different conjugated porphyrins and metalloporphyrins. We synthesized different porphyrins bearing at least one carboxylic group substituent to enable the deposition of the porphyrin onto an amino-functionalized glass surface (glass surface modified with (3-Aminopropyl-triethoxysilane, APTES).[21] The characterization of the materials suggests most of the porphyrins retain the ability to absorb solar light and generate reactive oxygen species upon irradiation. We believe our work will inspire the design of new systems to that can reduce the cost and improve the environmental impact of the methods implemented for water purification.

This work has been done in collaboration with Dr. Edith Amuhaya, Dr. Amuhaya's research group and Dr. Tebello Nyokong with support from the Canada's international Development Research Centre (IDRC).

3.4 Materials and Methods

Reagents. All chemicals were purchased from Sigma-Aldrich, unless specified otherwise. Sterile PBS solution was prepared using 18.2 MΩ cm^{-1} Milli-Q water obtained from a Millipore System equipped with a 0.22 μm filter.

Synthesis of porphyrins

Porphyrins were synthesized via the Adler-Longo method.[23] Benzaldehyde was added to distilled pyrrole and reacted for 3h under reflux in propionic acid. The formation of the porphyrin occurs by the addition of the pyrrole to the carbonyl carbon of benzaldehyde and then undergoes tetramerization to form the porphyrin ring. Subsequently, the solution was cooled to room temperature, filtered under vacuum and washed thoroughly using either methanol or dichloromethane depending on the benzaldehyde used (Scheme 3.1).

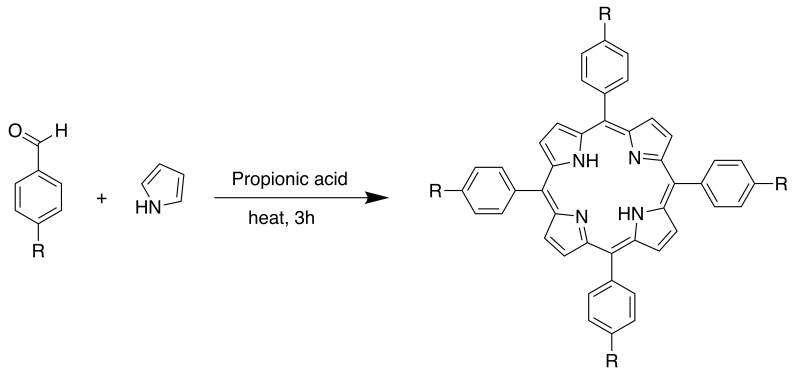

Scheme 3.1. Acid catalyzed synthesis for the preparation of meso-substituted porphyrin.

5,10,15,20-tetrakis (4-carboxyphenyl) porphyrin (TCPP) (0.259 mmol 14% yield) was synthesized by the addition of 4-formylbenzoic acid (1.09 g, 0.0073 mol) to 125 mL of propionic acid. Distilled pyrrole (0.516 mL, 0.0073 mol) was added to the solution and placed under reflux for 3 h. The solution was then left to cool overnight and washed under vacuum with chilled ethanol (100 mL). Afterward, the filter paper containing the sample was dried in the oven and further washed using distilled water and dried.

Similarly, 5,10,15,20-tetrakis(4-methoxyphenyl) porphyrin (TMPP) (0.148 mmol 18% yield) was synthesized by adding p-anisaldehyde (2.22 mL, 0.018 mol) to 125 mL of propionic acid. Distilled pyrrole (1.26 mL, 0.018 mol) was added to the solution then placed under reflux for 3 h. The sample was washed under the same conditions as the aforementioned porphyrin, however, due to the

high dissolution of the compound in EtOH, the sample was washed with dichloromethane (DCM) instead.

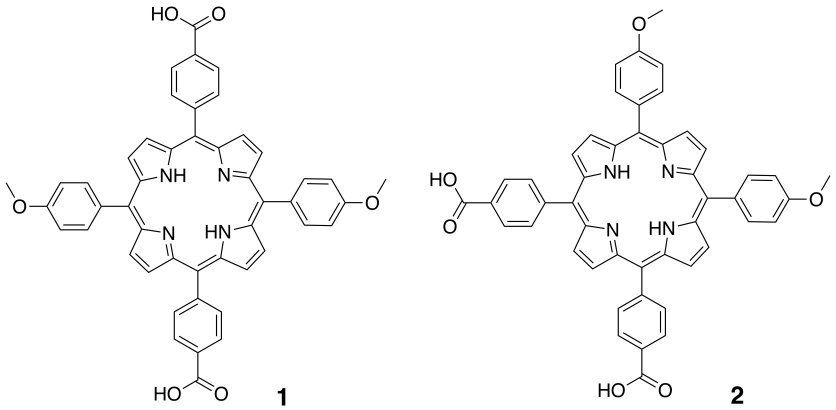

Scheme 3.2. Structure of compounds 1 and 2.

Compounds 1 & 2 (Scheme 3.2) were prepared by combining 4-formylbenzoic acid (0.7 g, 0.0047 mol) and p-anisaldehyde (1.7 mL, 0.0140 mol) in 125 mL of propionic acid. Distilled pyrrole (1.3 mL, 0.018 mol) was added to the solution and placed under reflux for 3 h. Compounds were separated using a silica plug containing DCM and was filtered using a separatory funnel containing diethyl ether and distilled water to eliminate any propionic acid or impurities remaining in the mixture. The mixture was further purified using column chromatography using hexane: ethyl acetate (3:1) then dried in a rotary evaporator to remove any remaining solvent. Structure was identified using electrospray ionization mass spectroscopy (Appendix Figure 3A.1).

Synthesis of metallophorphyrins

Porphyrin complexes inserted with zinc (II) were synthesized by magnetic stirring of the free base porphyrins with zinc (II) acetate at a molar ratio of 3:1 (Zn $(Oac)_2$: porphyrin). The final solution contained a mixture (50:50 v/v) of Zinc (II) acetate in methanol and porphyrin in DC in a round bottom flask. The solution was covered and left to stir for 3 days.

Activation of glass wool using (3-Aminopropyl)triethoxysilane (APTES)

Bare glass wool was modified with the addition of (3-Aminopropyl)triethoxysilane (APTES). A covalent bond is formed between the silanols on the surface of the glass wool and the silane of the APTES, resulting in an exposed reactive amine group for the attachment of the carboxylic acid group of the porphyrin (Figure 3.3). Glass wool (~1 g) was immersed in HPLC grade toluene containing a 1% (v/v) APTES (≥98%) solution and was heated overnight at 110 °C to enable coverage of the GW. The solution was allowed to cool to room temperature while stirring for 8 h and subsequently washed with toluene (2x), acetone (2x) and water (2x) to remove any silane molecules that were weakly bonded to the support. The resulting APTES on glass wool (APTES@GW) was dried in the oven at 100 °C.[21]

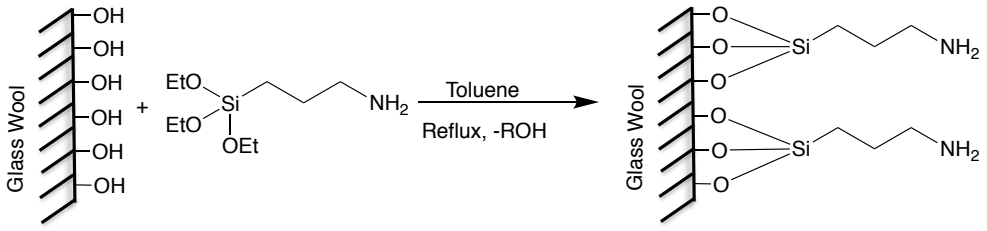

Scheme 3.3. Functionalization of glass wool with APTES.

Quantification of APTES on glass wool

The quantity of APTES attached onto bare GW was quantified using the protocol by Kunc *et al.* with some modifications.[24] Triplicate samples of APTES@GW (~65 mg) were submersed into a test tube containing 0.4M NaOD solution (1 mL) and was placed in a heated (45°C) sonicator bath for 3 h. 650 µL of the solution was removed and analyzed by ^{1}H NMR with an internal standard of maleic acid (20 µL, 9.9 mg/mL) in D_2O.

Glass wool modification

Porphyrins containing carboxyphenyl group were attached to GW according Chidawanyika *et al.* with some minor changes (Scheme 3.4).[25] 5,10,15,20-tetrakis (4-carboxyphenyl) porphyrin and compound 1&2 (2 mg) were dissolved in DMF (5 ml). N,N -Dicyclohexylcarbodiimide (DCC) was added at a molar ratio of 1.5:1 (DCC: porphyrin) to convert the –COOH group into an active carbodiimide ester group. The mixture was left to stir for 24 h and then APTES@GW (100 mg) was added to the reaction mixture and was gently rotated for 48 h using a hot dog cooker at room temperature. The glass wool product was removed from solution was washed several times with DMF to remove any excess of unreacted porphyrin and DCC intermediate by-products using vacuum filtration. The samples were subsequently dried in an oven at 100 °C overnight. To ensure there was no leaching of porphyrin, the GW was washed with water in a soxlet overnight and dried again.

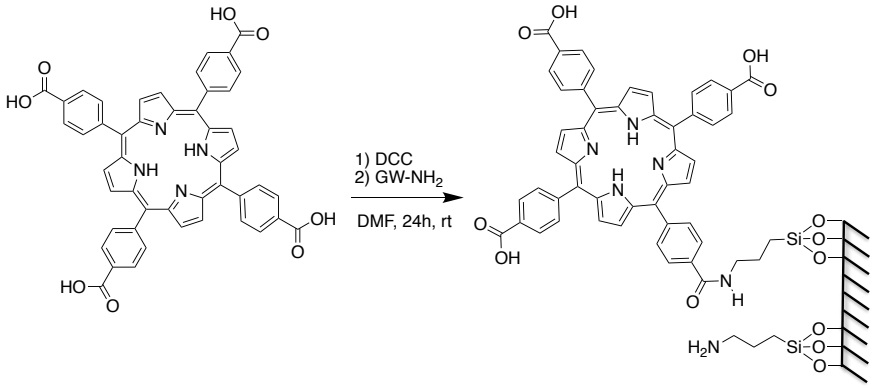

Scheme 3.4. Synthesis route for TCPP chemically linked to APTES@GW.

Attachment of metallated TMPP (TMPP-Zn (II)) to GW was attempted through the coordination of the NH_2 group to the Zinc (II) located inside of the ringed structure of the porphyrin (Scheme 3.5). TMPP-Zn (II) ($1x10^{-5}$ M) was dissolved in a solution mixture of THF and ethanol (1:1 v/v) with the APTES@GW (100 mg) and left to gently stir at ambient temperature for 72 h.

The solid was removed and washed with a THF/ethanol mixture (1:1 v/v) under vacuum and dried in an oven at 100 °C overnight. To ensure there was no leaching of porphyrin, the GW was washed with water in a soxlet overnight and dried again.

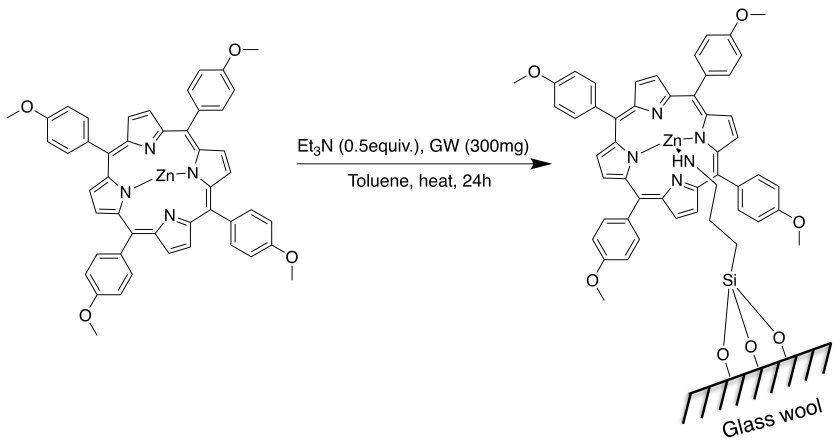

Scheme 3.5. Attachment of TMPP-Zn (II) to APTES@GW.

Photooxidation of 9,10-anthracenedicarboxylic acid

The photo-oxidative properties of the TCPP on APTES@GW (TCPP@GW) were examined by placing 1mg of the catalyst in a D_2O solution containing 9,10-anthracenedicarboxylic acid (75 μM) in a quartz cuvette. The reaction was irradiated for up to 5 h at room temperature. The concentration of the 9,10-anthracenedicarboxylic acid was measured using the absorbance spectrum and the consumption of the compound was monitored by following the decrease of the peak at 369 nm. Samples were irradiated at a wavelength of 450 nm (blue LEDi).

Antimicrobial activity of porphyrin in solution

Antimicrobial activity was tested against *Staphylococcus aureus* 292S3 at a concentration 10^6 CFU mL^{-1} in phosphate buffered saline (PBS) with 5% DMSO to solubilize the porphyrins. *Staphylococcus aureus* 292S3 was grown in Luria-Bertani (LB) broth at 37°C, shaking at 200 rpm. Using a 96-well plate, 10 μL of

porphyrin (100 µg/mL serially diluted to give differing concentrations) in DMSO and 190 µL of bacterial suspension were mixed and irradiated with blue-red light at 37 °C shaking at 150 rpm. All samples were in triplicate. Absorbance at 600 nm was read using a microplate reader.

Instrumentation

UV-visible Spectroscopy (UV-VIS) absorption spectra of porphyrin in solution were recorded by a CARY 60 UV-Vis spectrometer.

UV-Vis spectroscopy of the degradation of 9,10-Anthracenedicarboxylic acid and diffuse reflectance measurements was carried out in an Agilent Cary 50 Bio UV-Vis Spectrophotometer.

Solid-state emission spectra were acquired in a Perkin Elmer Luminescence Spectrometer LS50 by using a front-face support and quartz disc as sample holders.

^{1}H analysis was carried out in a Bruker Advance II 400MHz NMR spectrometer.

Thermogravimetric analysis was carried out using a TGA Q50 from TA instruments, from ambient temperature to 550 ºC, at a heating rate of 10 ºC/min. and under a constant nitrogen flow of 25 ml/min.

Glass wool that underwent plasma treatment was done using the Oxygen Plasma Etcher - PE-50 bombarded with oxygen (O_2, 10 sccm, 10 W) for 10 mins. Samples were not treated with oxygen plasma, unless indicated.

Absorption for antimicrobial activity experiment was carried out in a 96 well-plate using a microplate reader SpectraMax M5.

LC-MS of porphyrin sample was conducted with the Agilent InfinityLab Liquid Chromatography/Mass Selective Detector (LCMSD) system. The sample is analysed using a single quadrupole LC/MSD system that runs in parallel to the infinity II LC system.

3.5 Results and Discussion

Synthesis of the porphyrins

The Adler-Longo method garners a low yield of meso-substituted porphyrins due to the formation of oligomers and dipyrromethanes that are a product of the high reactivity of the pyrrole and the dipyrromethanes in the acidic media. This requires multiple rounds of chromatographic purification, which results in the low yield. Moreover, when trying to synthesize porphyrins under milder conditions offered, the introduction of more complex substituents can result in further decrease in an already low yield. For this reason, porphyrin structures with lesser complexity were synthesized and used for initial testing of the attachment of the porphyrins onto the support. The use of functional groups consisting of a carboxylic acid, a methoxy group or a mixture of the two, were synthesized to allow for sufficient material to be available to explore the attachment of porphyrin onto the glass wool support.

Characterization of porphyrins

Porphyrins were characterized by UV-Vis absorbance spectroscopy, unless indicated otherwise. Porphyrins characteristically have a sharp intense around 400nm (B Band), also called the Soret band. The intensity of the Soret band for metalloporphyrins is not as strong and is slightly red shifted compared to the non-metallated counterpart as a result of a weak interaction between the porphyrin and the metal.[26,27] Porphyrins also present four less intense absorption bands, called Q bands, that can be found in the visible region of the spectrum (500 to 700 nm), which are responsible for the red/ purple colour of the free base porphyrin. Upon metallation, there is a collapse of the four Q bands into two bands due to their higher D_{4h} symmetry.[28] UV-Vis spectroscopy of synthesized porphyrins produced an absorbance reading that follows the general pattern of a porphyrin absorbance spectrum demonstrating that we had successfully produced our desired products (Figure 3.3-3.5).

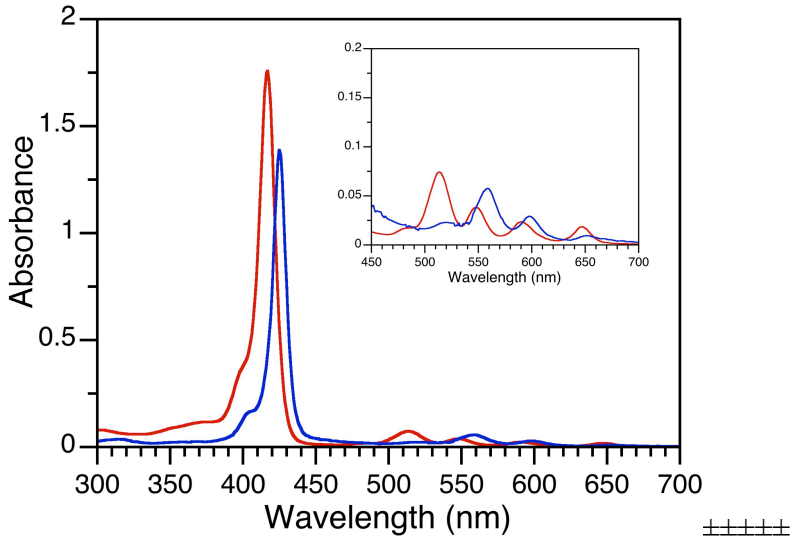

Figure 3.3. Absorbance spectra of 3.75 μM TCPP (red) and 0.2 μM TCPP-Zn (II) (blue) in ethanol.

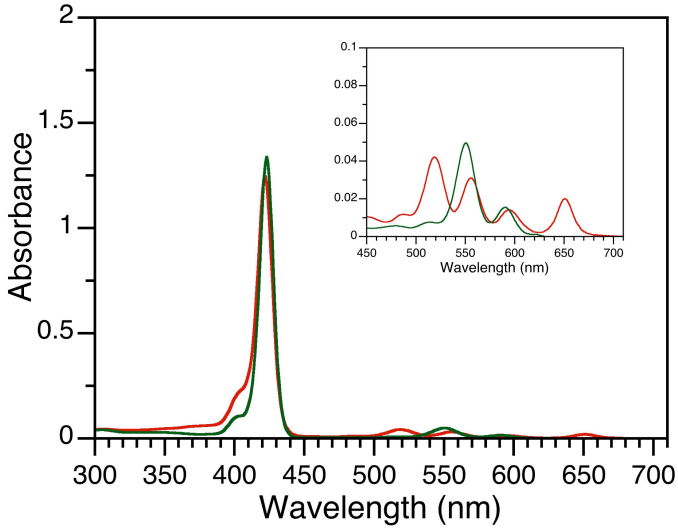

Figure 3.4. Absorbance spectra of 3 μM TMPP and 1.8 μM TMPP-Zn (II) in DCM.

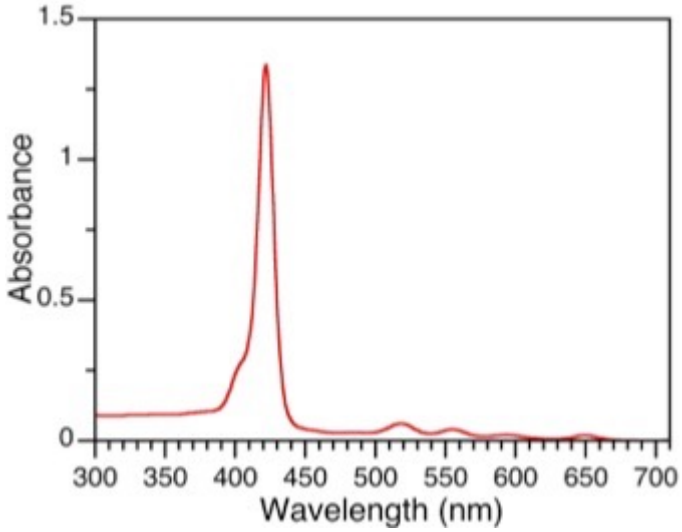

Figure 3.5. Absorbance spectrum of compound with either structure 1 (6.5 μM) in DCM. Structure 2 would give an identical absorbance profile.

Quantification of APTES supported on glass wool

APTES was used as a linker for surface functionalization of the glass wool support. The exposed amine group offered by the attached APTES facilitates covalent binding to a carboxylic acid using the coupling agent DCC.[21,29] Quantification of the APTES layer was analyzed by ^{1}H NMR. Peaks produced are a result of the hydrolysis of the amino propyl groups found on the surface of the support. Similar to previous report by Kunc *et al.*, the sample was suspended in a basic media (0.4 M NaOD solution) in order to release the immobilized functional groups into the solution for ^{1}H NMR.[24] The average integral for the three ^{1}H NMR signals of APTES was used to estimate the amine content relative to the internal calibrant (maleic acid) (Figure 3.6)

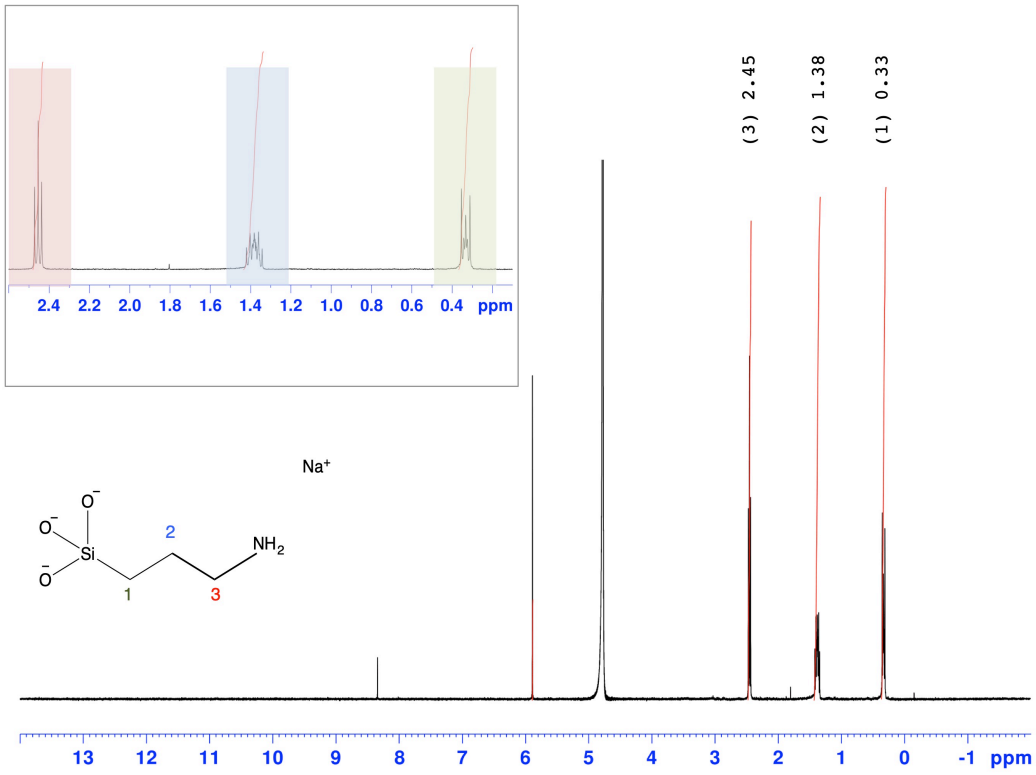

Figure 3.6. ^{1}H NMR spectrum acquired from APTES@GW in 0.4M NaOD solution (1mL). Integrals for the characteristic resonances at approximately 0.33, 1.38 and 2.45 ppm are compared to the internal standard of maleic acid (80 mmol) at 5.89 ppm.

Several different hydrolysis conditions were tested to determine the optimal method for hydrolysis. Initially, APTES@GW (~65 mg) was placed in vial containing a 0.4 M NaOD solution (4 mL) and placed in an oven heated at 45 °C for 3, 6 and 24 h. No peaks appeared for the 3 h reaction and the 24 h sample produced peaks with lower intensity than that at 6 h, which could indicate degradation of the released amine (Appendix Figure 3A.2).

To help improve hydrolysis of the amino propyl groups, the oven was replaced with a heated sonicator bath. In addition to this, reactions were conducted using 1 mL of NaOD rather than 4 mL for the reaction to improve the ^{1}H NMR signals. These aforementioned changes seem to have improved the time required to quantify the APTES functionalized on glass wool (Appendix Figure 3A.3). Triplicate samples from the same batch were reacted in the heated

sonicater bath using 1 mL of NaOD for 3 h and for 6 h. It was found that both reactions produced an estimated wt.% of APTES on GW that was within error of each other (Table 3.1) therefore, further reactions were done using 3 h.

Table 3.1. Comparison of different times used to quantify amine-functional-group of the APTES functionalized on glass wool using ^{1}H NMR.

Time (h)	Wt.% APTES on GW
6	0.24 ± 0.06
3	0.20 ± 0.04

Different batches (denoted GW batch 1 and 2 in Table 3.2) of GW functionalized with APTES were analyzed to investigate reproducibility of ^{1}H NMR quantification method. The content of APTES appears to be similar between batches with an average around 0.3 wt.%. These values combined with the previous wt.% calculations; the estimated wt.% is 0.25 ± 0.04.

The increase in standard deviation between samples in the same batch could be due to the lack of homogeneous attachment of the APTES onto the glass wool sample. This could be a result of the collapsing of the glass wool upon immersion into toluene during the synthesis process. Areas not exposed to the reaction solution would not be in contact with the APTES, resulting in a higher concentration of the APTES on the exterior of the support.

Table 3.2. Amine-functional-group quantification of the APTES functionalized on glass wool using ^{1}H NMR.

GW batch	Wt.% APTES on GW
1	0.28 ± 0.10
2	0.30 ± 0.17

This pattern of patchy attachment was further validated when TCPP was reacted with the APTES@GW. The porphyrin (yellow) attached to the GW in concentrated areas, mostly on the periphery of the GW (Figure 3.7).

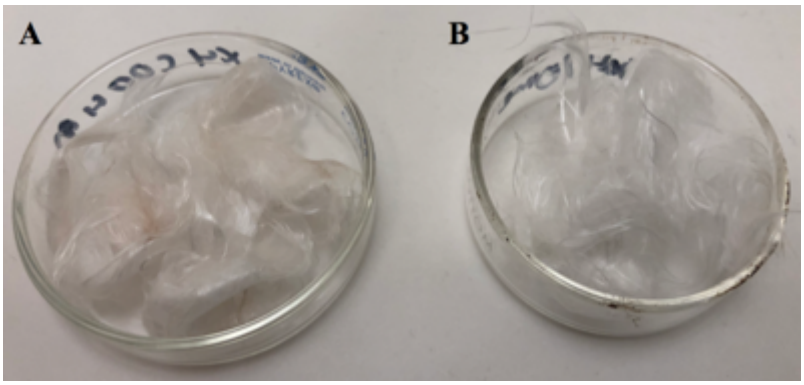

Figure 3.7. General appearance of (A) TCPP@GW and (B) APTES@GW materials.

Since the material chosen is an organic material (APTES) attached to an inorganic support (GW), thermogravimetric analysis (TGA) was used to try to provide some additional information regarding the quantity of APTES on the support. The glass wool fibers were too large for the equipment; therefore, the samples were required to be grounded into a powder using a pestle and mortar for analysis. Initial weight loss below 100 °C is due to the loss of water. Weight loss was also observed between 200 and 600 °C for both the APTES@GW (blue) and the bare GW (red), with the bare GW showing a greater decrease in weight (%) (Figure 3.8). This, unfortunately, means that this method led to inconclusive results regarding APTES concentration alone but does have the potential to be used as a tool for quantification of the APTES linker if the sample contained a higher concentration of APTES. Additionally, the TGA spectra does demonstrate that the GW undergoes minimal weight loss at high temperatures which indicates the material is quite stable and would not easily disintegrate if integrated into a flow system.

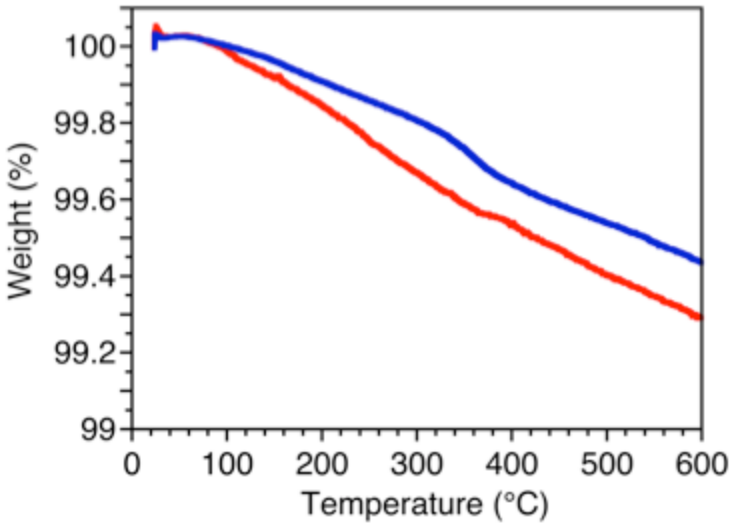

Figure 3.8. Thermogravimetric analysis (TGA) of APTES@GW (blue) (4.52 mg) and bare GW (red) (2.96 mg) under N_2 at a heating rate of 10 °C min^{-1}.

Characterization of porphyrin attachment onto APTES@GW

Initial attempts made to covalently attach the TCPP, TMPP and a mixture of compounds 1 and 2 and to attach the porphyrin by means of coordination of the metal to the APTES@GW (0.3 wt% APTES) did not produce desired results. Due to the very small quantity of APTES attached to the glass wool support (0.25%), only the TCPP sample attached to the APTES@GW was concentrated enough to produce a peak in the diffuse reflectance (Figure 3.9) or fluorescence spectra (Figure 3.10). Although we were not able to attach a high concentration of APTES to the GW, these results demonstrate that porphyrin attaches covalently, since there was only a minimal amount of APTES on the GW before the porphyrin was attached. GW reacted with porphyrin is washed thoroughly to remove any porphyrin that is weakly bonded to the support.

Additionally, porphyrins have a high molar extinction coefficient, which means the chemical species can absorb light strongly in the visible range (regions indicated in Figures 3.1-3.3). Therefore, it should not require a high concentration of porphyrin to form enough radicals to react with pollutants in its surrounding environment.

The presence of the porphyrin was analyzed by diffused reflectance and solid-state fluorescence. Diffuse reflectance of the TCPP@GW sample produced a peak around 420 nm, which corresponds to the Soret band of the porphyrin, but we are unable to see the Q bands due to the low concentration of the porphyrin (Figure 3.9). The emission spectrum of TCPP@GW produced a fluorescence pattern for TCPP similar to the emission spectrum of TCPP in solution, demonstrating that the porphyrin was able to attach to the APTES@GW, as shown in Figure. 3.10.[30]

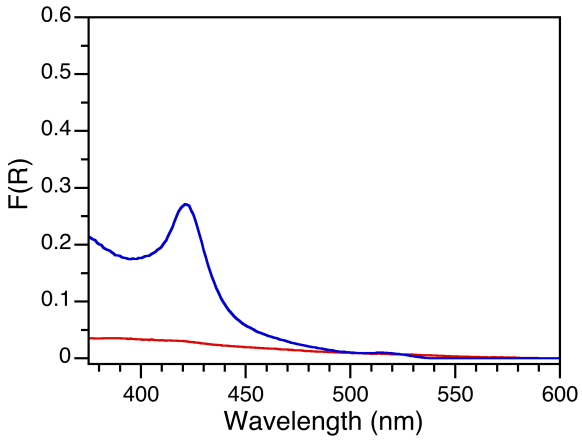

Figure 3.9. Diffuse reflectance spectra of A TCPP functionalized on APTES@GW (blue) and unmodified APTES@GW (red).

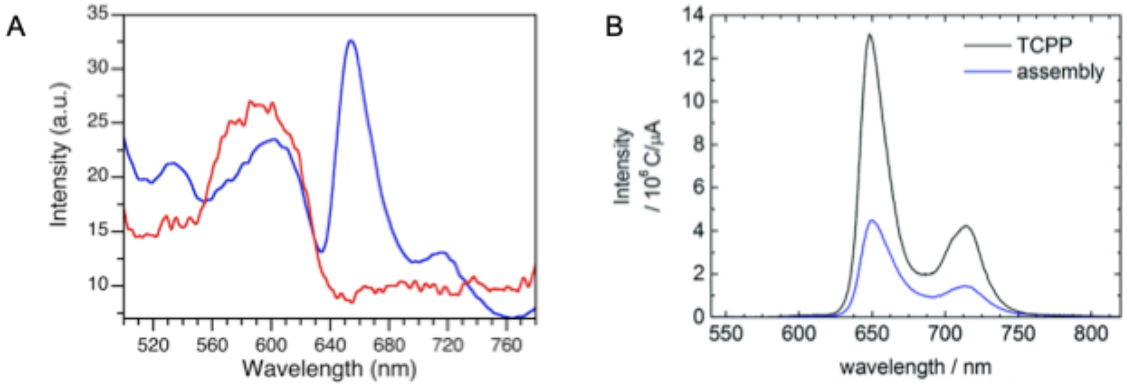

Figure 3.10. Emission spectra of A) TCPP functionalized on APTES@GW (blue) and unmodified APTES@GW (red), λ_{ex}=420 nm, and B) TCCP in solution where λ_{ex}=420 nm. Reprinted from J. Düring and F. Gröhn[30] with permission from the Royal Society of Chemistry.

Singlet Oxygen production

Free base porphyrins produce singlet oxygen when exposed to light of the appropriate wavelength. Since the singlet oxygen is short lived (10^{-4}-10^{-6} s), any damage made to biomolecules require them to be in close proximity to the site of the $^1O_2$ formation.[27,31] Therefore, it is important that the resulting porphyrin functionalized on support retains its ability to generate these radical species. The production of $^1O_2$ was analyzed according to the principle that $^1O_2$ species can degrade 9,10-anthracenedicarboxylic acid and weaken the absorption of 9,10-anthracenedicarboxylic acid. The 9,10-anthracenedicarboxylic acid molecules react with singlet oxygen and will undergo cycloaddition to yield an endoperoxide resulting in the loss of the 9,10-anthracenedicarboxylic acid absorption peaks (Scheme 3.6).

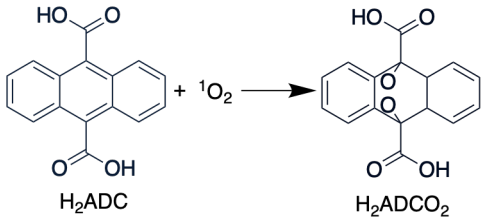

Scheme 3.6. Singlet oxygen-mediated photooxidation of 9,10 anthracenedicarboxylic acid.

As shown in Figure 3.11, the absorption peaks of the 9,10 anthracenedicarboxylic acid decreased over time in the presence of the TCPP@GW over a period of 5 h. The weakening of the absorption peaks is a consequence of the formation of the endoperoxide formed as a result of the reaction of the 9,10 anthracenedicarboxylic acid and $^1O_2$. Moreover, there was no oxidation reaction under dark conditions (Appendix Figure 3A.24). The reaction kinetics can be approximated by a linear decay (Figure 3.12).

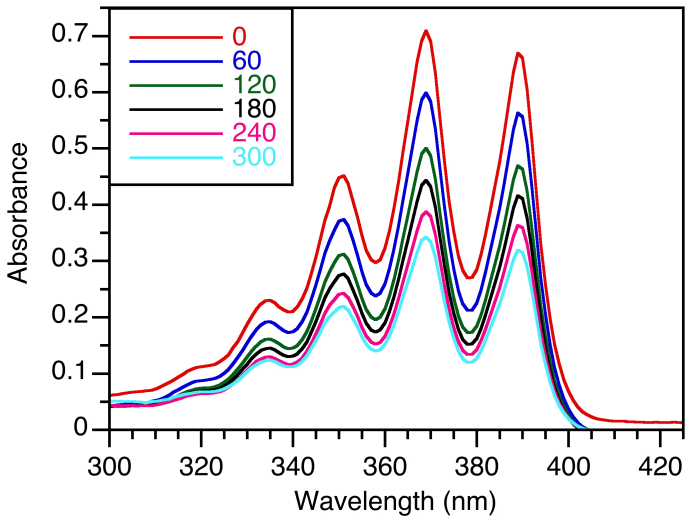

Figure 3.11. Oxidation of 9,10-anthracenedicarboxylic acid (75μM) upon 450nm light irradiation (blue LEDi) of TCPP@GW in D_2O under air for 5 h.

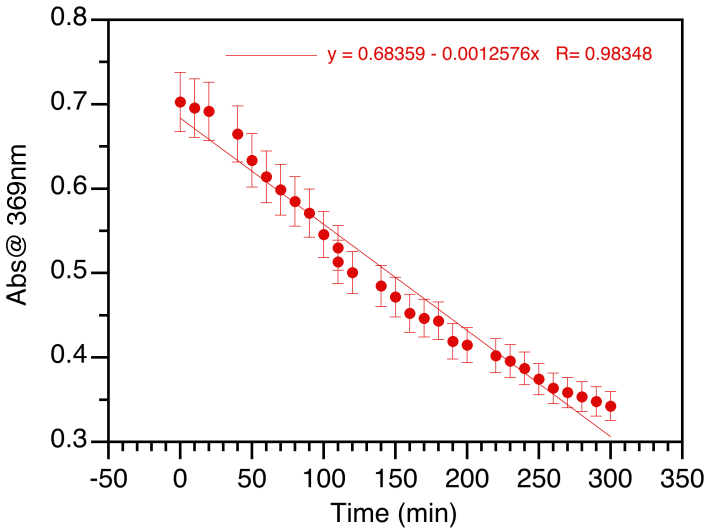

Figure 3.12. Graphical representation of the decrease of in the absorbance peak at 369 nm upon 450 nm light irradiation (blue LEDi) of 9,10-anthracenedicarboxylic acid in D_2O under air.

Plasma Oxygen Etching of APTES@GW

To aid in the synthesis of the APTES@GW and increase the quantity of APTES, bare glass wool underwent a plasma treatment. In this process, a thin surface layer is removed using short pulses of oxygen plasma. The resulting clean surface from the O_2 plasma increases its wettability and therefore, allows

for more APTES to attach. Glass wool samples (~500 mg) were flattened by hand to create a disk shape and were bombarded with oxygen for 10 minutes. Samples were then flipped and blasted again since bombardment of plasma occurred in a single upward direction. Samples were immediately reacted with APTES in toluene to minimize impurities. APTES functionalization to the treated GW was analyzed using ^{1}H NMR. Plasma treatment seemed to have increased the quantity of APTES substantially. The initial amount of APTES that to attached to the GW was estimated 0.25% (w/w), however, the plasma treatment increased this value to approximately 3% (w/w), as shown in Table 3.3. Due to the high standard deviation found for the subsequent APTES samples that were not treated with plasma oxygen (Table 3.2) and the high deviation for the 3 h using the etching, the reaction was conducted for 6 h rather than 3 h. It was found to produce a similar result. We can approximate the APTES coverage is now between 2.3-3.8 % (w/w), which is a significant improvement to previous results. The high standard deviation between triplicates in the plasma treated samples indicates that the etching was not able produce a homogeneous coating of APTES. Samples that were treated with the oxygen plasma were bombarded with the oxygen plasma in a unidirectional fashion, which could have led to than inhomogeneous plasma treatment, and thus, the deviation between samples after plasma treatment was also high.

To check the stability of the plasma oxygen etching, glass wool samples underwent the plasma treatment and were stored in a sealed container for one week. Samples were then functionalized with APTES, using the same protocol as before. The wt.% APTES bound to the GW after one week of treatment was similar to that of the samples that were immediately reacted with APTES (Table 3.3). This shows that the surface of the glass wool after plasma etching is stable and could be reacted with APTES a few days after treatment.

We are hopeful that with the demonstrated increase in APTES concentration on the GW due to the plasma treatment, the concentration of porphyrin attaching to the glass wool can also increase and be further characterized.

Table 3.3. Amine-functional-group quantification of the APTES functionalized on glass wool (with and without plasma oxygen etching treatment) using ^{1}H NMR.

GW sample	Wt.% APTES on GW
No O_2 etching average	0.25 ± 0.05
Etching batch 1 (3h)	3.86 ± 1.39
Etching batch 1 (6h)	2.28 ± 0.71
Etching batch 2* (3h)	5.70 ± 4.96
Etching 3 (1 week later) (3h)	5.19 ± 4.32

*H_2O in toluene= 0.003%

3.6 Conclusion

The minimal quantity of APTES attaching to the glass wool treated with plasma allowed for binding of the porphyrins but could possibly be improved with the treatment of plasma oxygen etching. The degradation of 9,10-anthracene dicarboxylic acid by the TCPP@GW is a promising result that indicates potential for a flow-assisted degradation of common organic pollutants, including pharmaceuticals often found in water systems. With improved attachment of the porphyrin to the GW, we hope to see an improved photocatalytic reaction from the porphyrins on support and potentially generate enough radical species to produce antibacterial effects.

3.7 Future work

Future work could begin with the attachment of porphyrins to the APTES@GW samples that have been treated with the oxygen plasma etcher. This will allow for the opportunity to characterize and analyze the heterogeneous material. Alternatively, modifying the coupling reaction of the APTES to improve APTES functionalization could be further explored. The attachment and orientation of APTES is dependent on a number of factors, including but not limited to the temperature, solvent, deposition time and the concentration of the

APTES.[32] This could prove to be more cost effective and improve the ability to scale up the reaction for a flow system. Furthermore, with the enhanced functionalization of the glass wool, the antimicrobial properties of the porphyrins can be tested against both gram-positive and gram-negative bacteria. As a preliminary study, free base porphyrins were tested against the gram-positive bacterium, *Staphylococcus aureus* (*S. au*), at differing concentrations. These studies were to see if the porphyrin could photocatalytically damage and kill the cells, since the formation of singlet oxygen from the TCPP@GW was demonstrated, as seen in Figure 3.12. Triplicate samples were irradiated with blue-red light for a total of 8 hours. The change in bacterial density was monitored over time by measuring the absorbance of each sample at OD600. Cell viability was calculated by the difference in the absorbance value from time 0, having been corrected for the absorbance of the porphyrin samples. The only concentration of porphyrin to produce sensible results was at a concentration of 20 μg/mL. Results from these absorbance readings are shown in Figure 3.13. Minimal antibacterial activity was observed during the experiment, with the samples containing methoxyl groups (light blue and dark blue) demonstrating a slight decrease in cell viability of approximately 20% or less. This decrease in cell viability can indicate that there is a potential for the use of the metallated TMPP coordinated onto the APTES@GW through the metal ion. However, more accurate results could be obtained by counting the colony forming units (CFU) on an agar plate.

The antibacterial activity of the photosensitizers should be further tested when attached to the GW support. It would be beneficial to also synthesize and attach porphyrin consisting of different functional groups and/or with a different type of metal inserted into the ringed structure, to see if that can improve the antibacterial activity of the material.

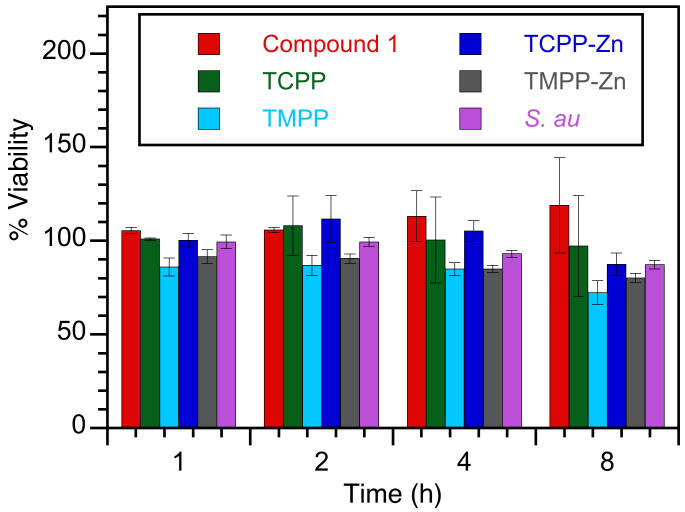

Figure 3.13. Time dependent cell viability (%) of *S. aureus* against compounds 1 and 2 (red), TCPP (green), TMPP (light blue), TCPP-Zn (II) (dark blue) and TMPP-Zn (II) (grey) porphyrins (20 µg/mL) compared to bacteria alone (purple) in PBS relative to time zero (t=0) irradiated using blue-red wavelength lamps (3x) at 37 °C shaking at 150 rpm

As part of the collaborative work, decorated titania fibers were fabricated with the ability to generate hydrogen, as well as, degrade organic material.[33] Through the use of APTES as a linker[34], TiO_2 fibers could be used as a support rather than the glass wool. Attaching porphyrins to the TiO_2 fibers can potentially improve the photocatalytic activity of the material by extending of light absorption capability and lower the rate of the TiO_2 electron-hole recombination; which will ultimately improve the materials ability to generate radical species and its photo-destructive abilities.[35]

Since pollution in water goes beyond the presence of microbes, it would be worthwhile to examine the potential of these porphyrins on support against other organic pollutants such as pharmaceutical pollutants and toxic metals that plague water sources. In 2011, Jeong *et al*. synthesized a organic-inorganic hybrid adsorbent consisting of TCPP immobilized on an amino functionalized mesoporous silica for the adsorption of Cu (II)-ions.[36] This shows purification potential of the porphyrins supported on glass wool that could go beyond the

scope of killing microbes. Lastly, since the goal of this heterogeneous catalyst is to be applied into a flow system, it will be essential to test the stability and reusability of the catalyst.

3.8 Appendix

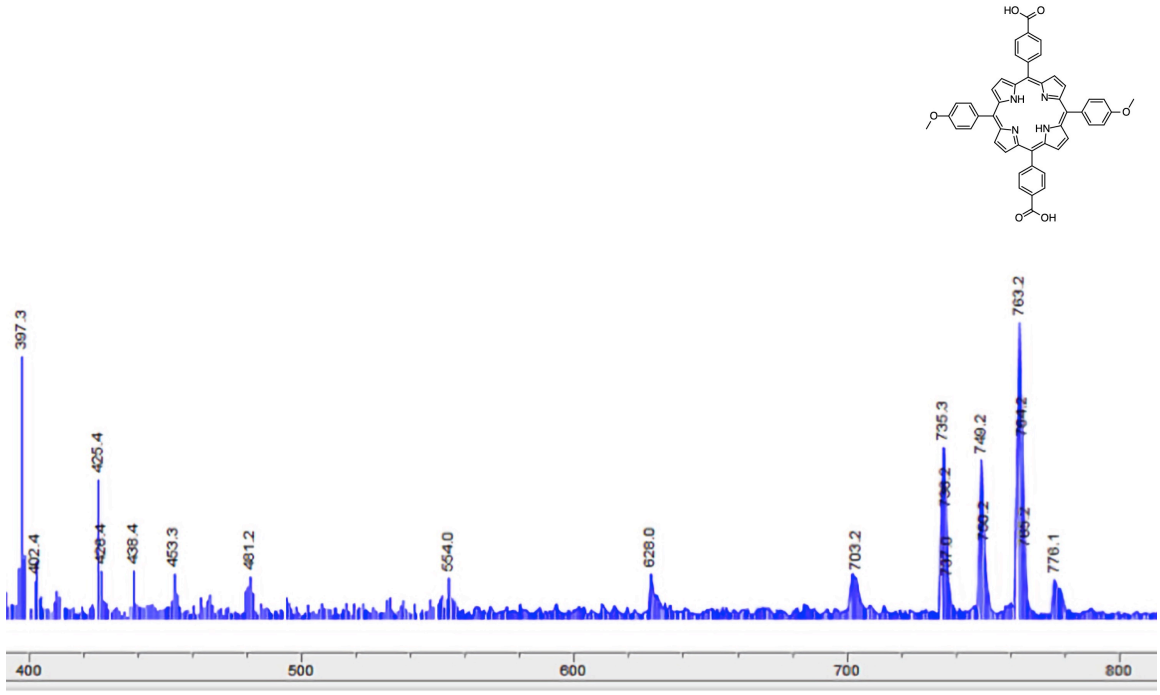

Figure 3A.1 MS spectrum of a mixture of compounds 1&2.

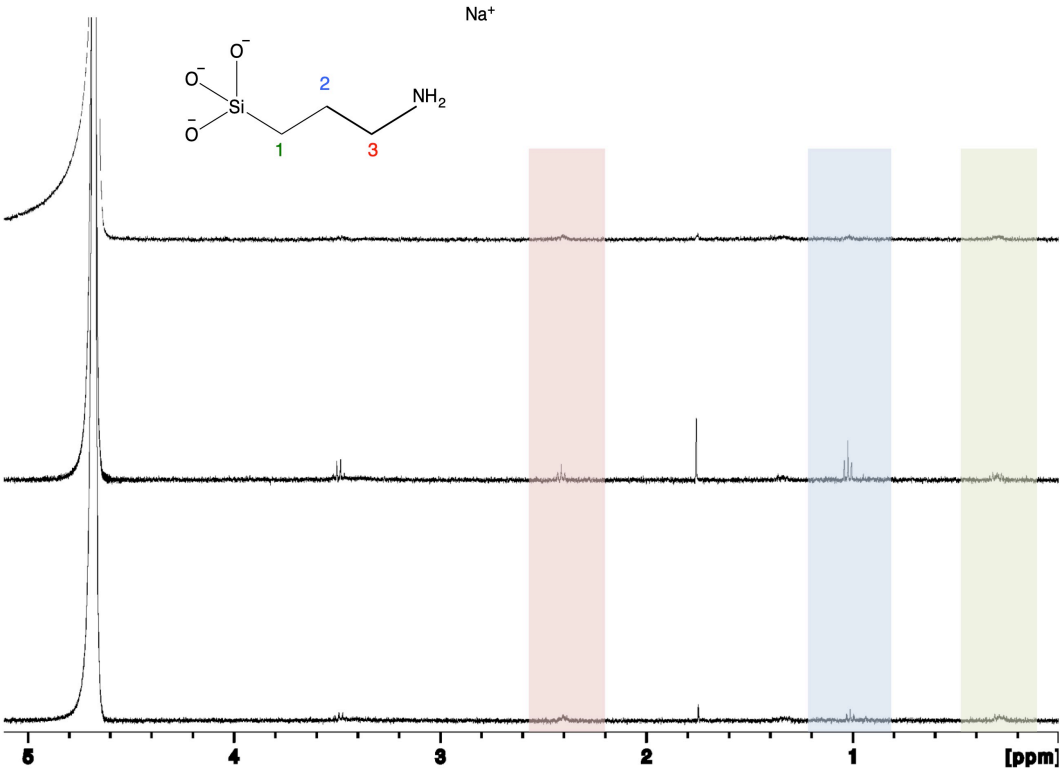

Figure 3A.2. ^{1}H NMR spectra acquired from APTES@GW in 0.4 M NaOD solution in D_2O heated in an oven 45 °C for 3, 6 and 24 h.

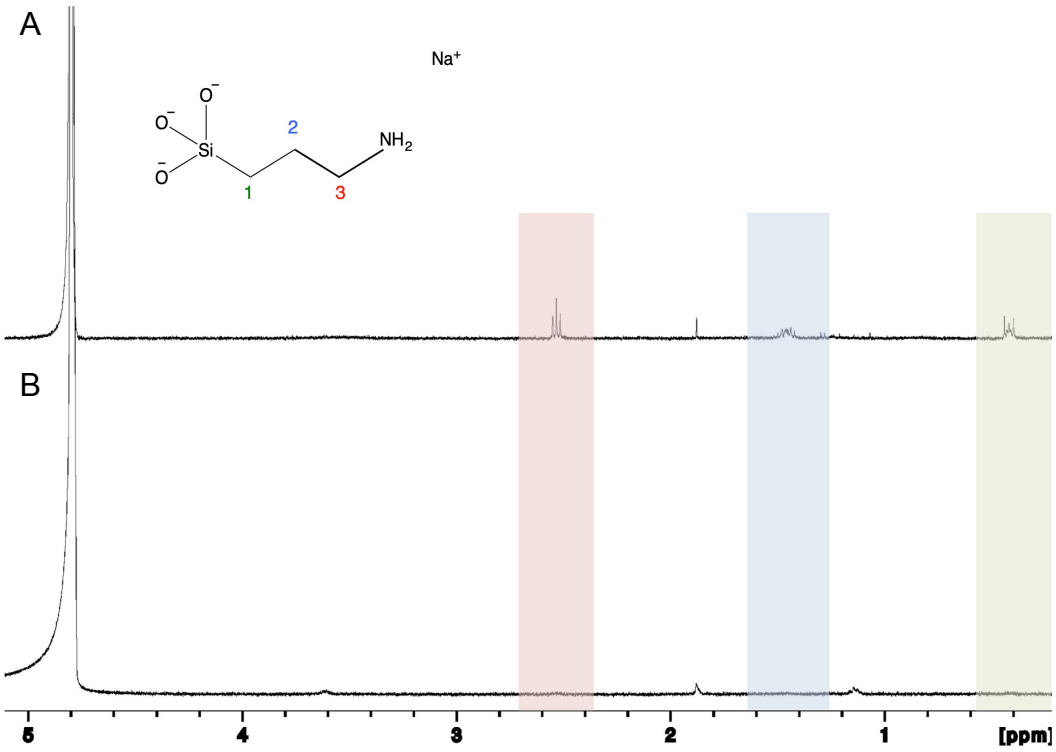

Figure 3A.3. ^{1}H NMR spectra acquired from APTES@GW in 0.4 M NaOD solution (4 mL) heated in an oven 45 °C for A) 6 h and B) 3 h.

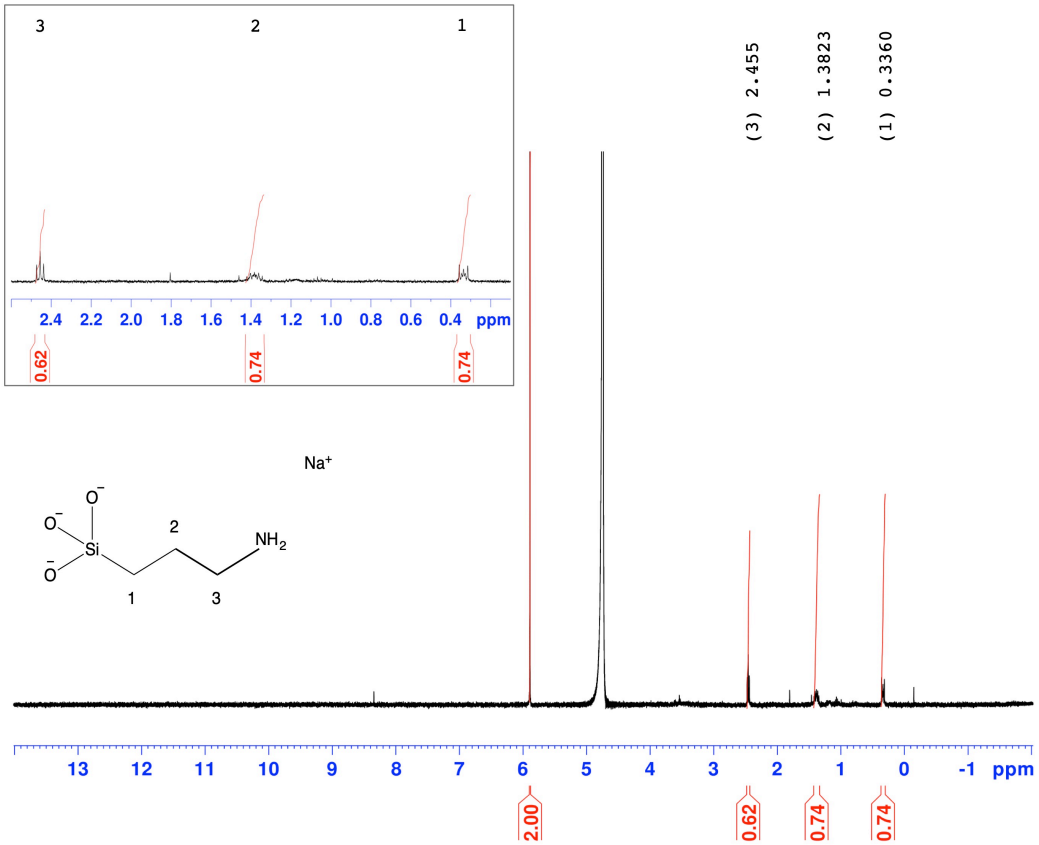

Figure 3A.4 ^{1}H NMR spectrum acquired from APTES@GW (1% APTES sample 1 6h) in 0.4M NaOD solution compared to the internal standard of maleic acid (80 mmol) at 5.89 ppm.

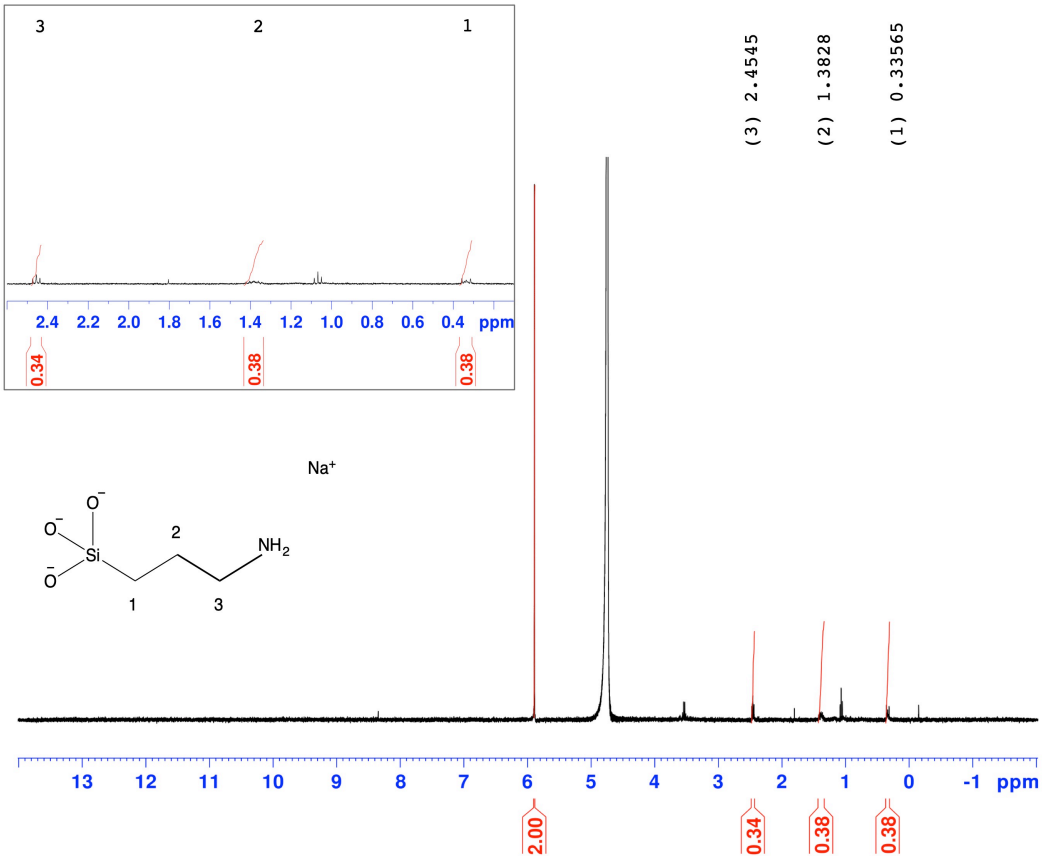

Figure 3A.5. ^{1}H NMR spectrum acquired from APTES@GW (1% APTES sample 2 6h) in 0.4M NaOD solution compared to the internal standard of maleic acid (80 mmol) at 5.89 ppm.

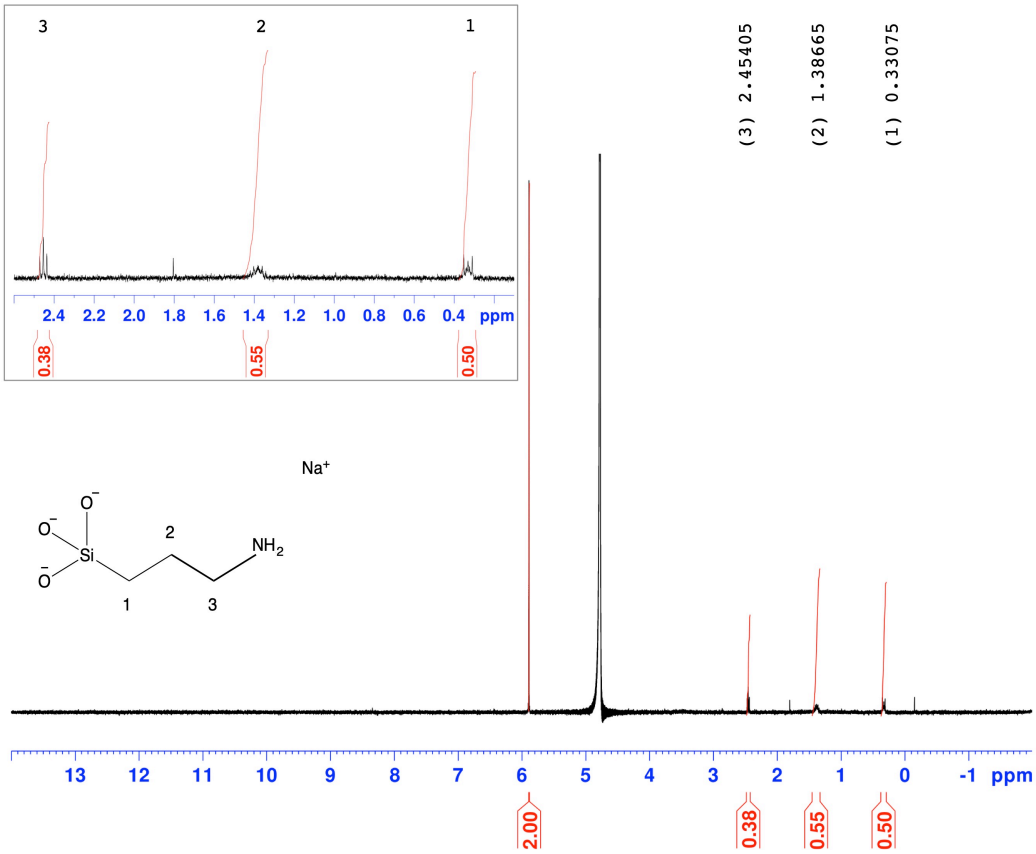

Figure 3A.6. ^{1}H NMR spectrum acquired from APTES@GW (1% APTES sample 1 spectrum 1) in 0.4M NaOD solution compared to the internal standard of maleic acid (80 mmol) at 5.89 ppm.

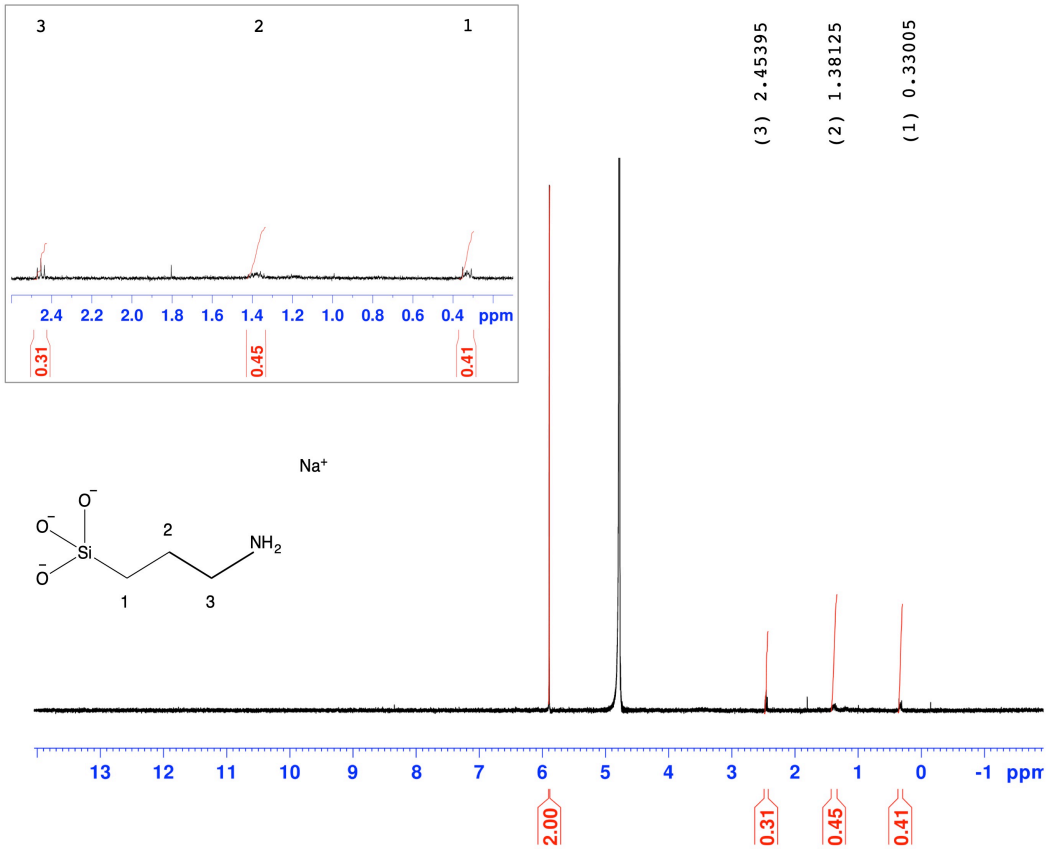

Figure 3A.7. ^{1}H NMR spectrum acquired from APTES@GW (1% APTES sample 1 spectrum 2) in 0.4M NaOD solution compared to the internal standard of maleic acid (80 mmol) at 5.89 ppm.

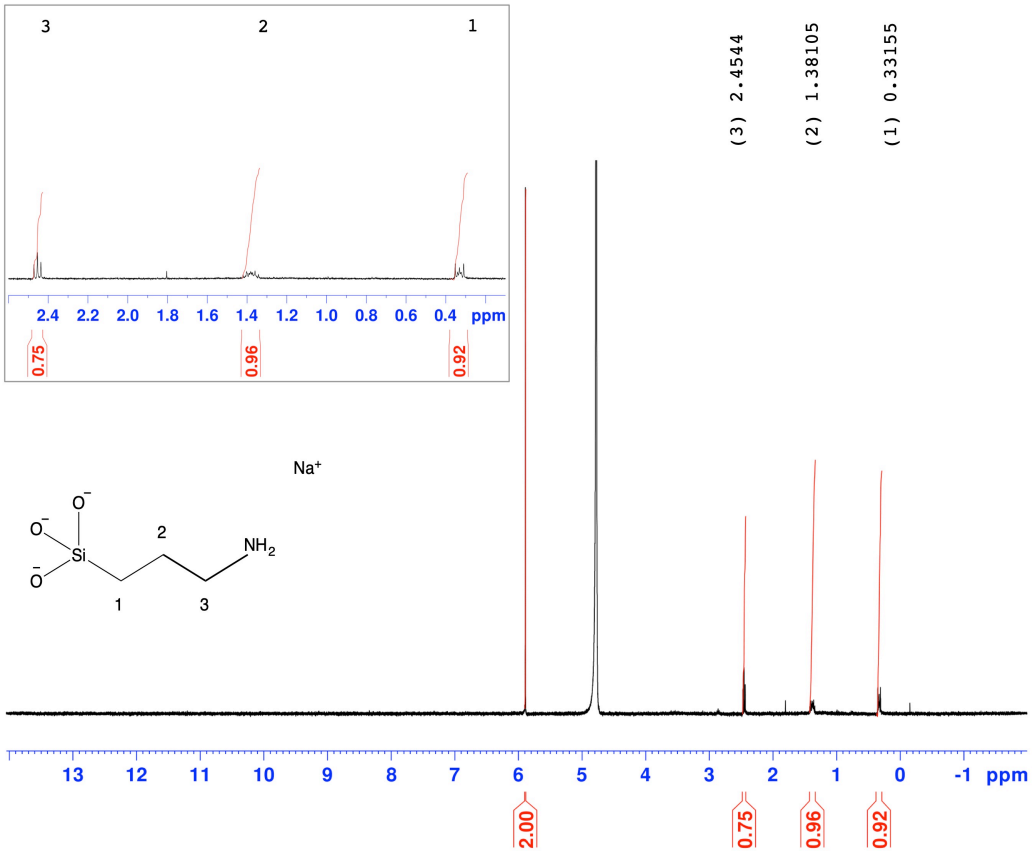

Figure 3A.8. ^{1}H NMR spectrum acquired from APTES@GW (1% APTES sample 1 spectrum 3) in 0.4M NaOD solution compared to the internal standard of maleic acid (80 mmol) at 5.89 ppm.

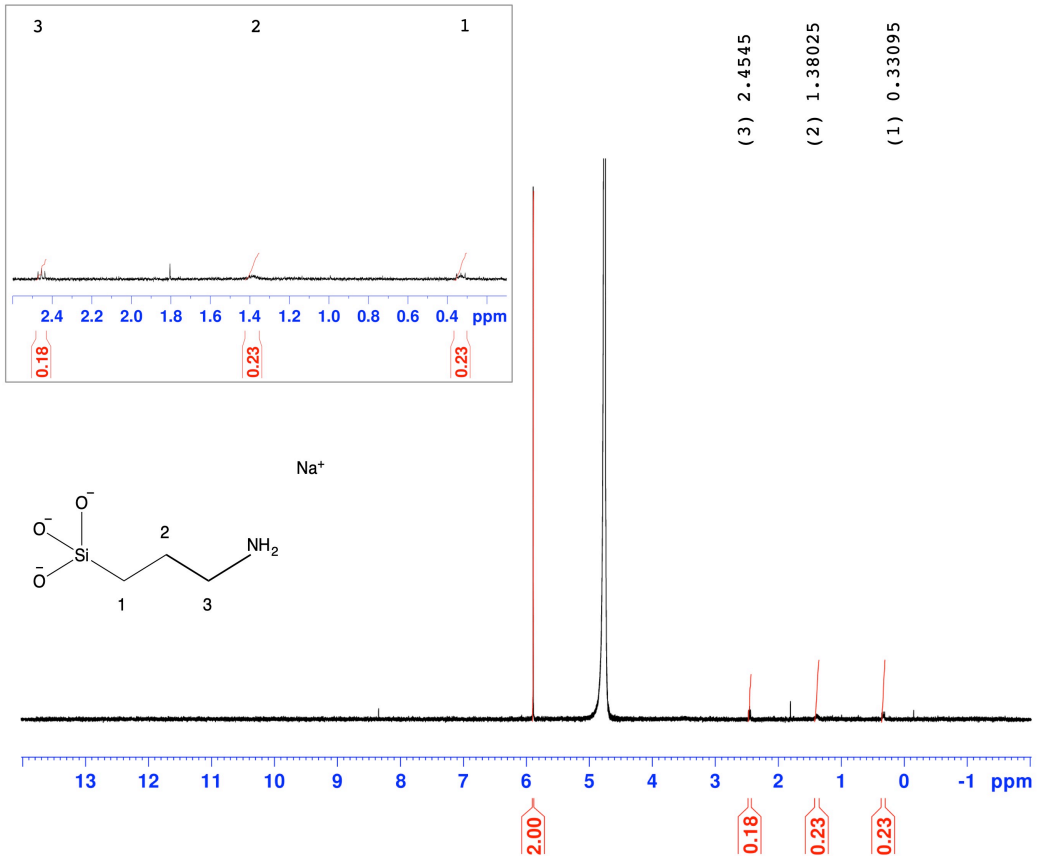

Figure 3A.9. ^{1}H NMR spectrum acquired from APTES@GW (1% APTES sample 2) in 0.4M NaOD solution compared to the internal standard of maleic acid (80 mmol) at 5.89 ppm.

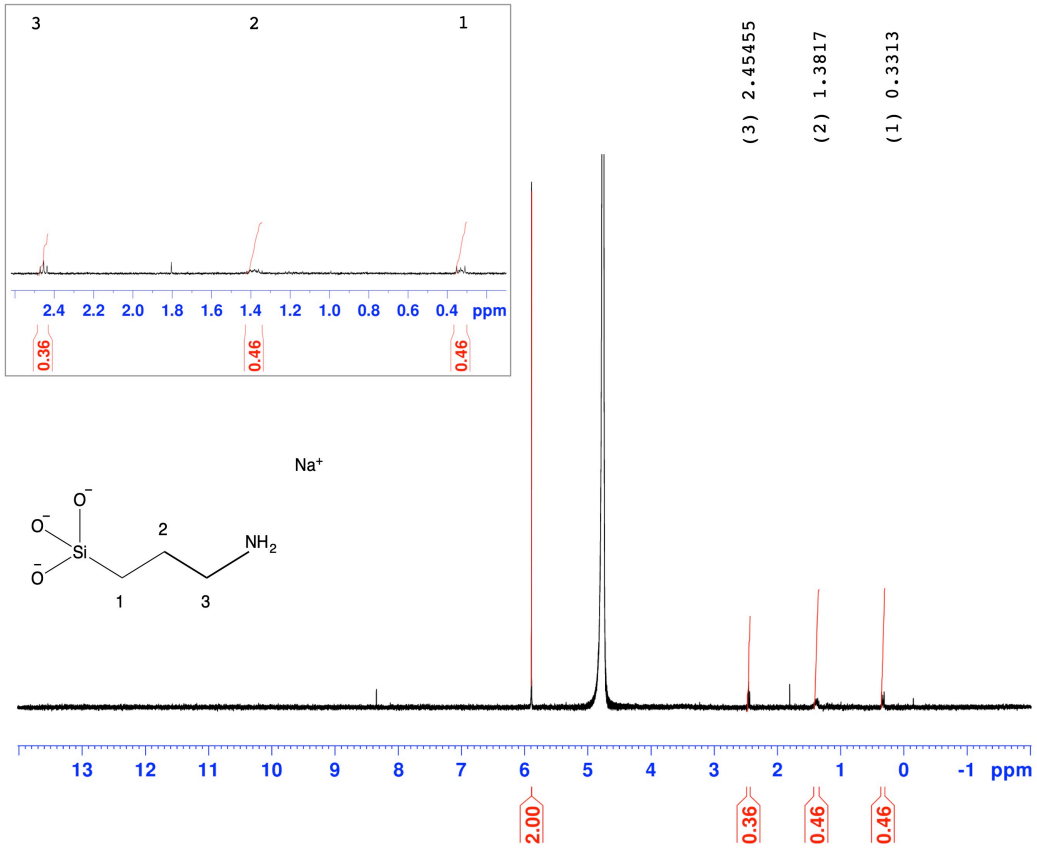

Figure 3A.10. ^{1}H NMR spectrum acquired from APTES@GW (1% APTES sample 2) in 0.4M NaOD solution compared to the internal standard of maleic acid (80 mmol) at 5.89 ppm.

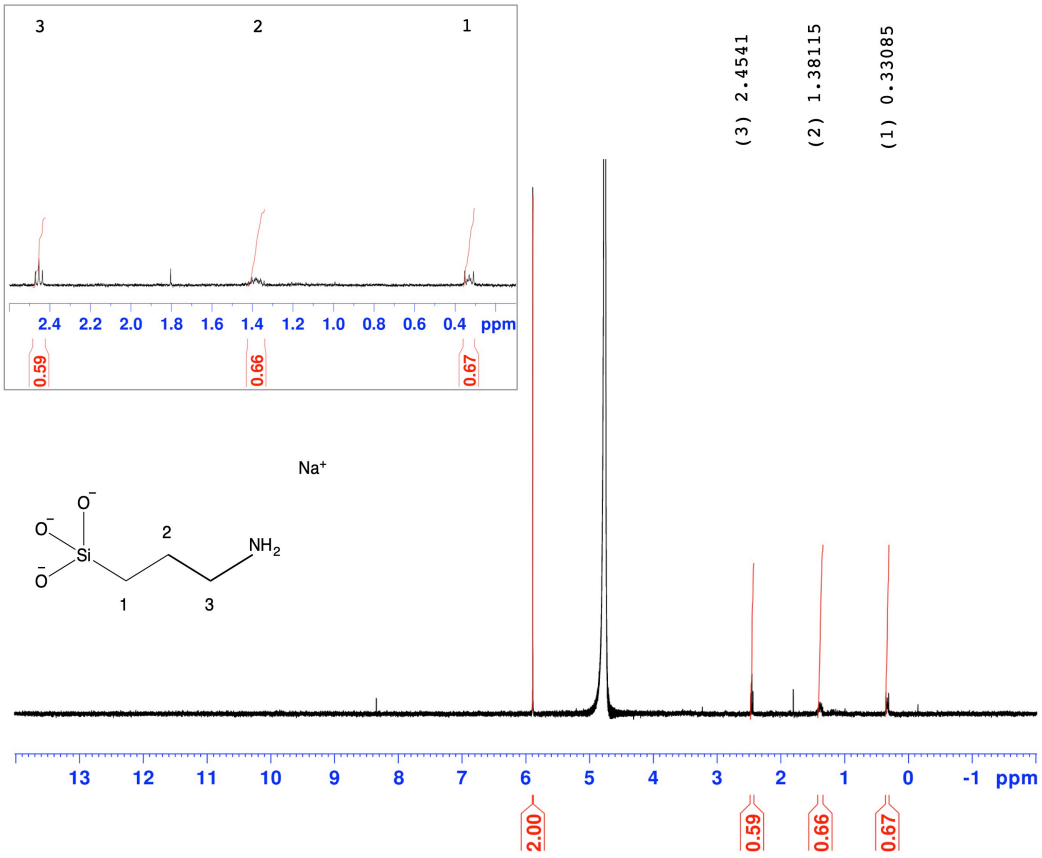

Figure 3A.11. ^{1}H NMR spectrum acquired from APTES@GW (1% APTES sample 2) in 0.4M NaOD solution compared to the internal standard of maleic acid (80 mmol) at 5.89 ppm

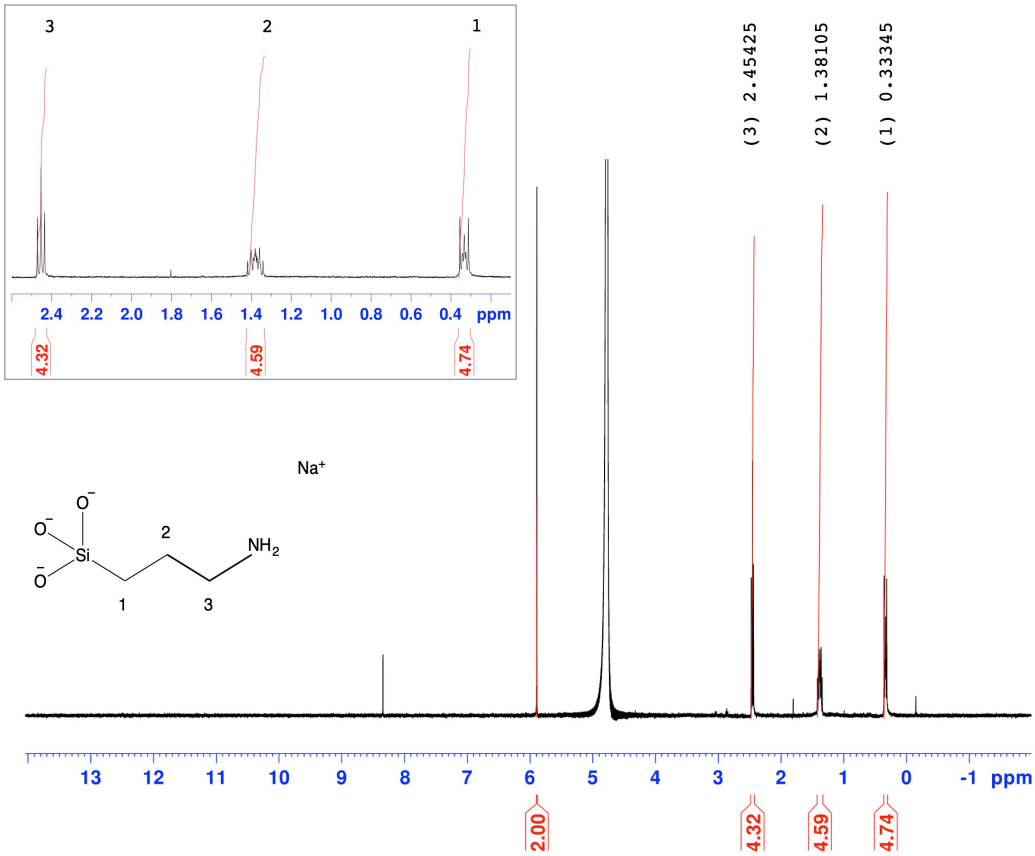

Figure 3A.12. ^{1}H NMR spectrum acquired from APTES@GW (1% APTES, plasma oxygen etching, batch 1 sample 1 reacted for 3h) in 0.4M NaOD solution compared to the internal standard of maleic acid (80 mmol) at 5.89 ppm.

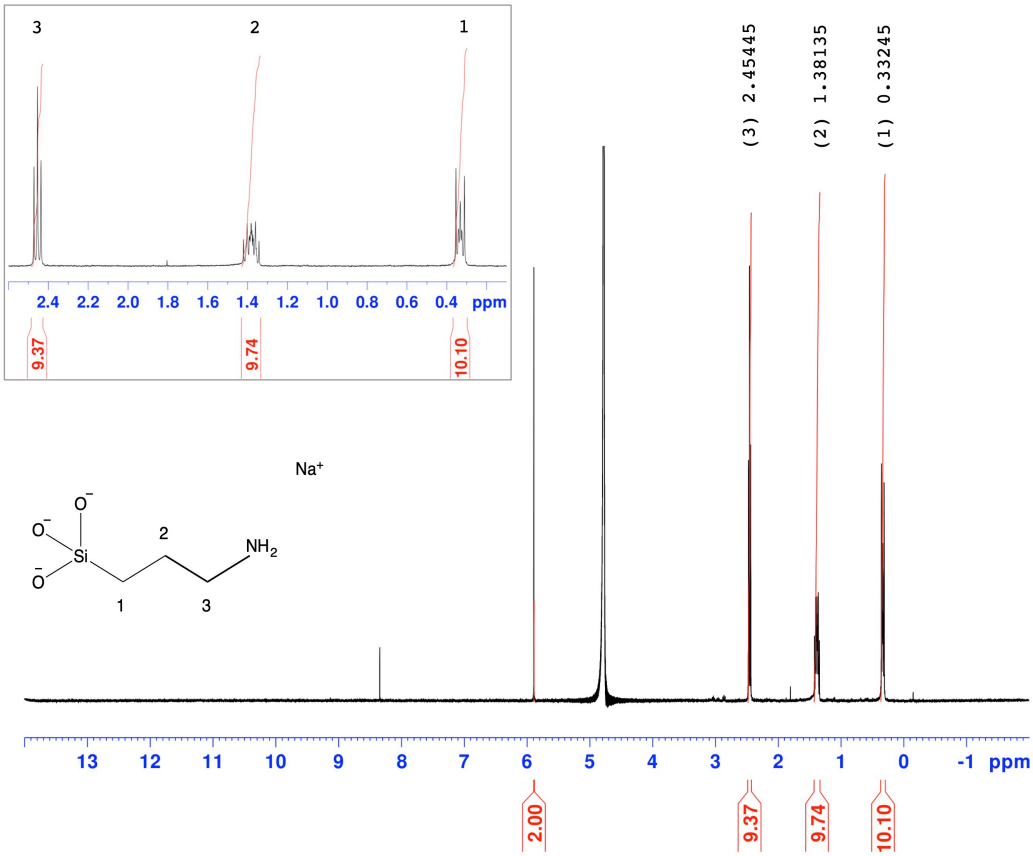

Figure 3A.13. ^{1}H NMR spectrum acquired from APTES@GW (1% APTES, plasma oxygen etching, batch 1 sample 2 reacted for 3h) in 0.4M NaOD solution compared to the internal standard of maleic acid (80 mmol) at 5.89 ppm.

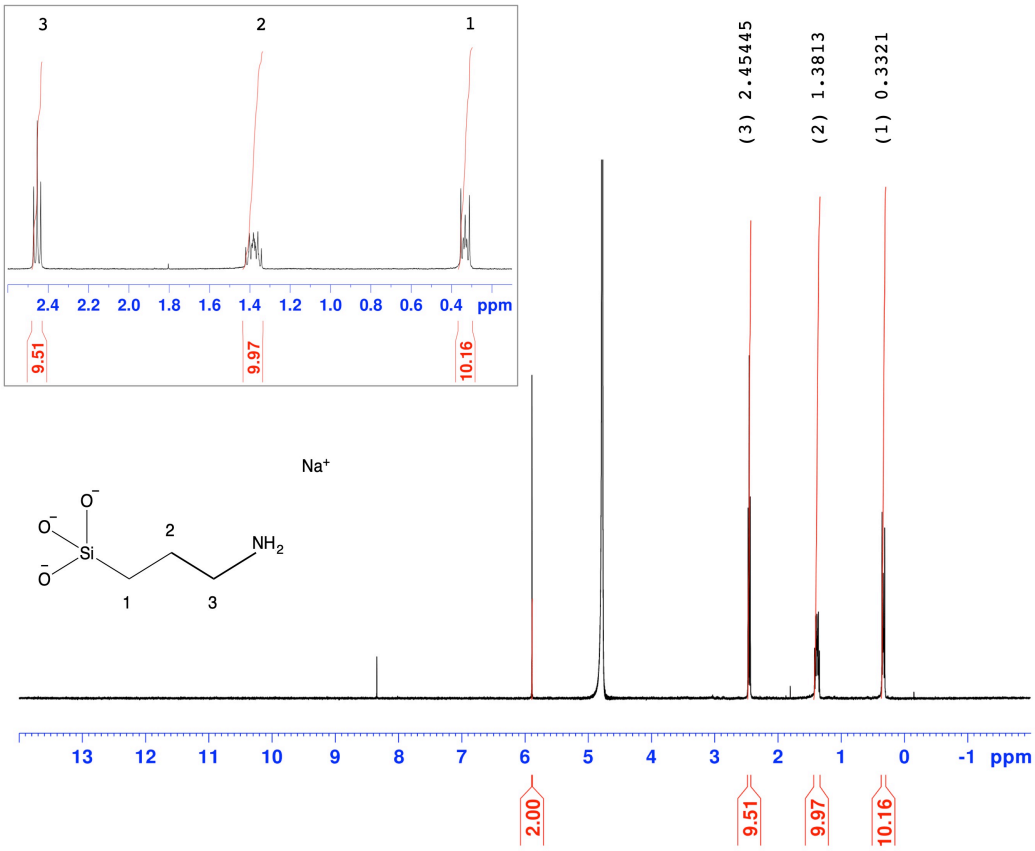

Figure 3A.14. ^{1}H NMR spectrum acquired from APTES@GW (1% APTES, plasma oxygen etching, batch 1 sample 3 reacted for 3h) in 0.4M NaOD solution compared to the internal standard of maleic acid (80 mmol) at 5.89 ppm.

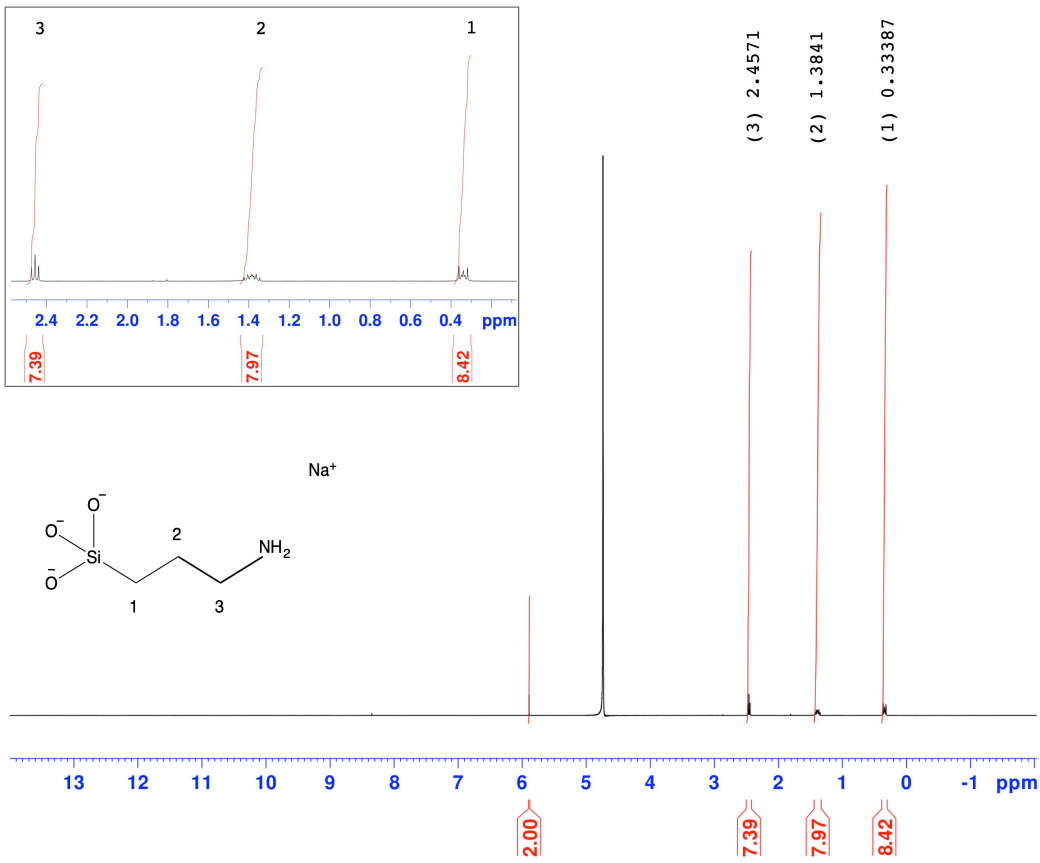

Figure 3A.15. ^{1}H NMR spectrum acquired from APTES@GW (1% APTES, plasma oxygen etching, batch 1 sample 1 reacted for 6h) in 0.4M NaOD solution compared to the internal standard of maleic acid (80 mmol) at 5.89 ppm.

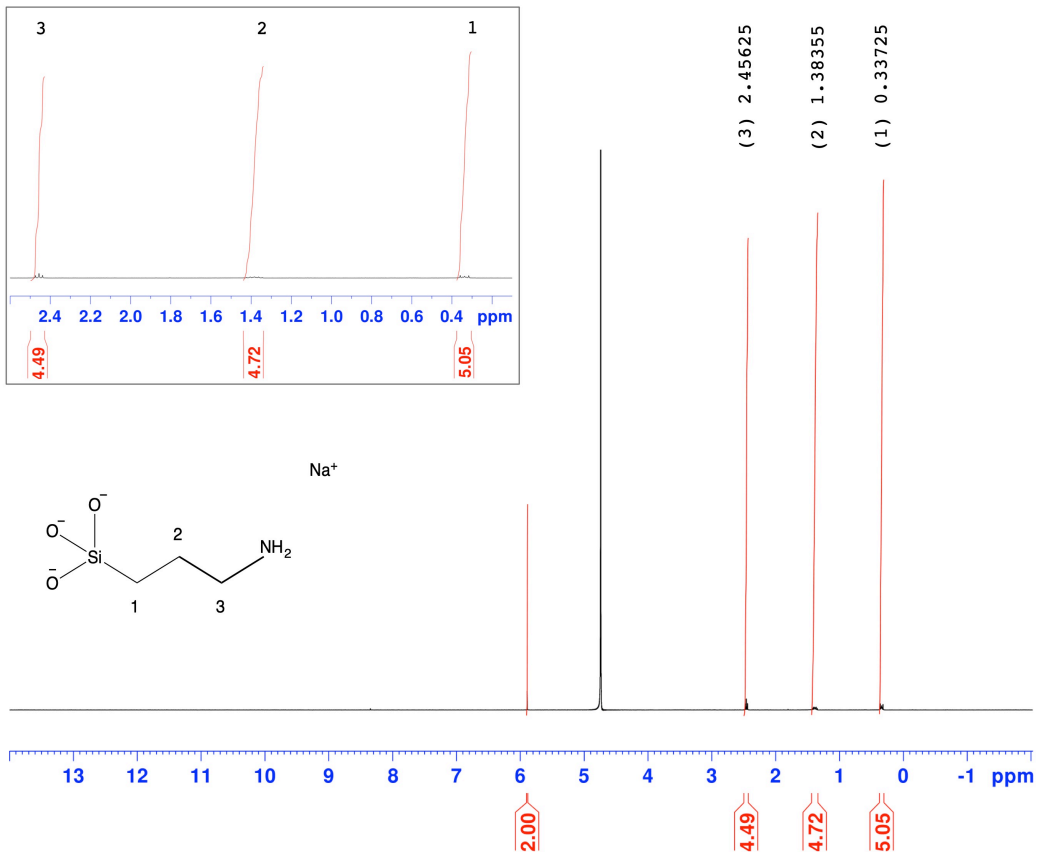

Figure 3A.16. ^{1}H NMR spectrum acquired from APTES@GW (1% APTES, plasma oxygen etching, batch 1 sample 2 reacted for 6h) in 0.4M NaOD solution compared to the internal standard of maleic acid (80 mmol) at 5.89 ppm.

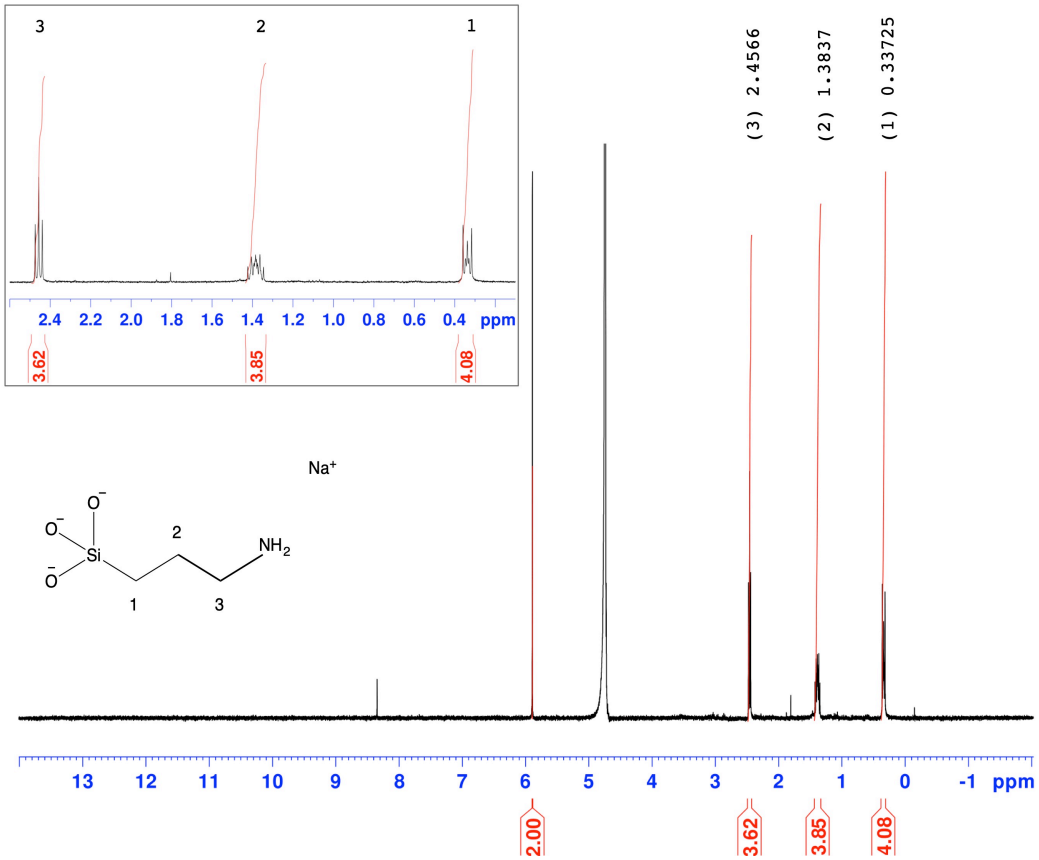

Figure 3A.17. ^{1}H NMR spectrum acquired from APTES@GW (1% APTES, plasma oxygen etching, batch 1 sample 3 reacted for 6h) in 0.4M NaOD solution compared to the internal standard of maleic acid (80 mmol) at 5.89 ppm.

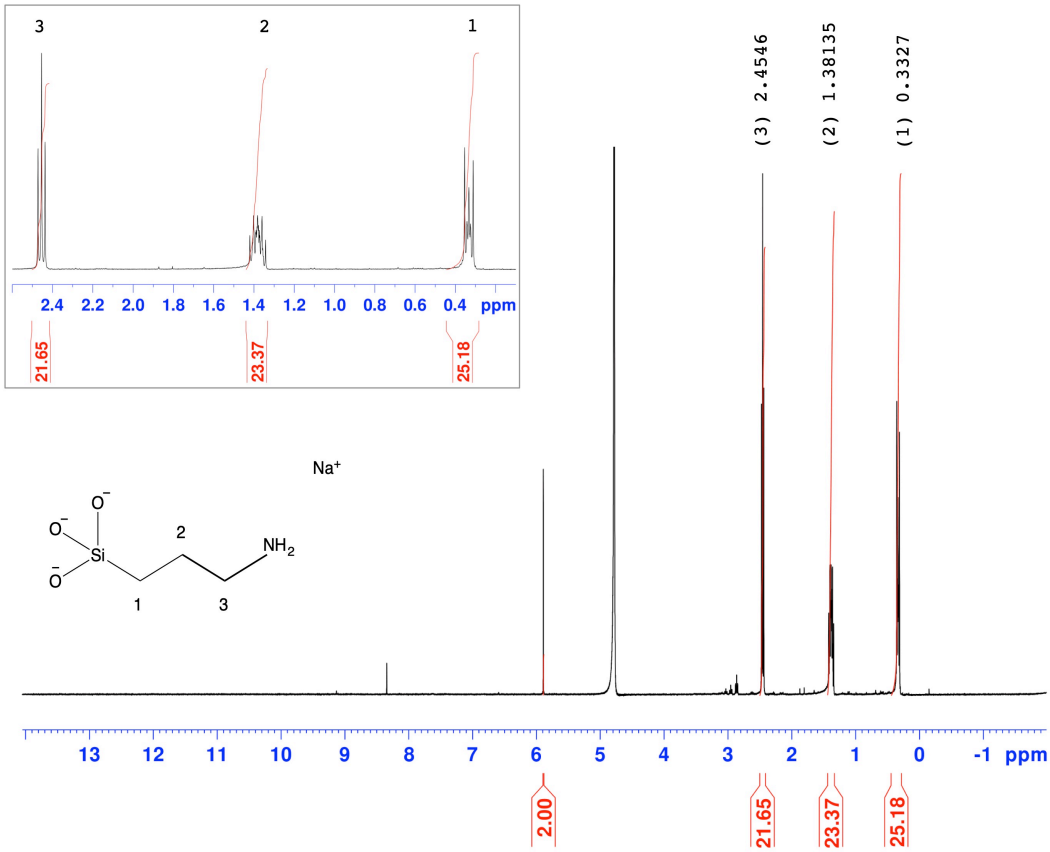

Figure 3A.18. ^{1}H NMR spectrum acquired from APTES@GW (1% APTES, plasma oxygen etching, batch 2 sample 1 reacted for 3h) in 0.4M NaOD solution compared to the internal standard of maleic acid (80 mmol) at 5.89 ppm.

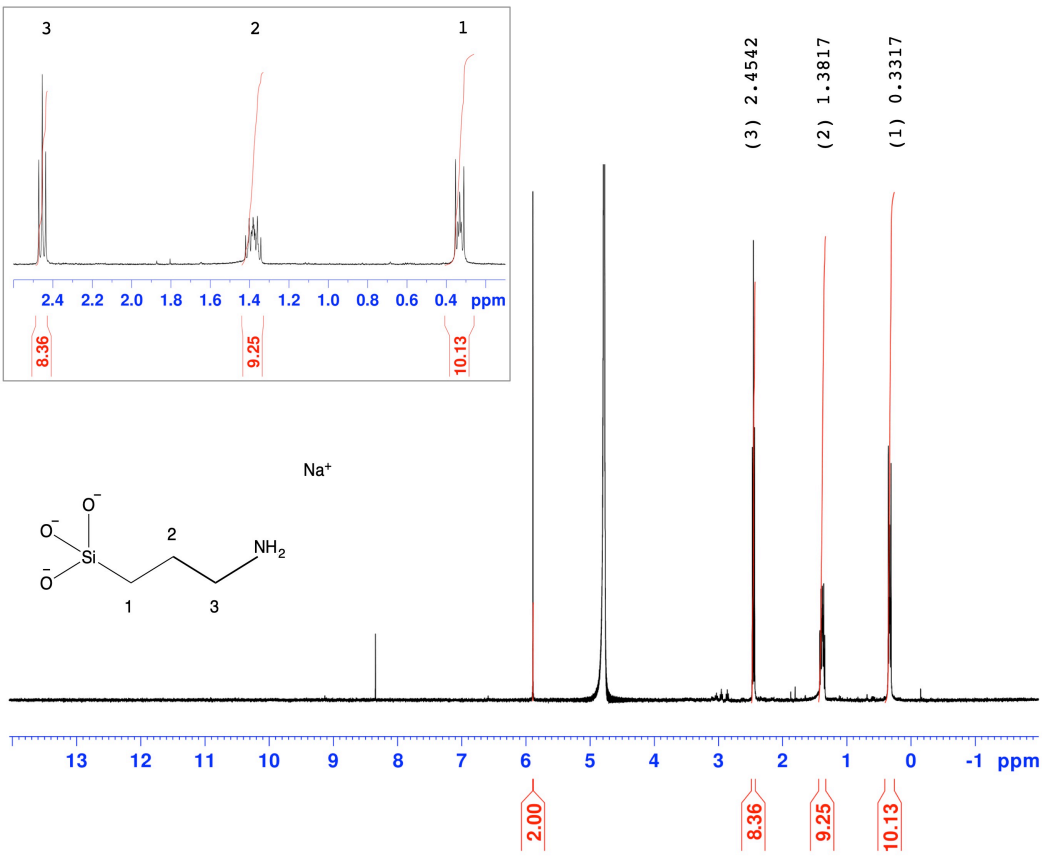

Figure 3A.19. ^{1}H NMR spectrum acquired from APTES@GW (1% APTES, plasma oxygen etching, batch 2 sample 2 reacted for 3h) in 0.4M NaOD solution compared to the internal standard of maleic acid (80 mmol) at 5.89 ppm.

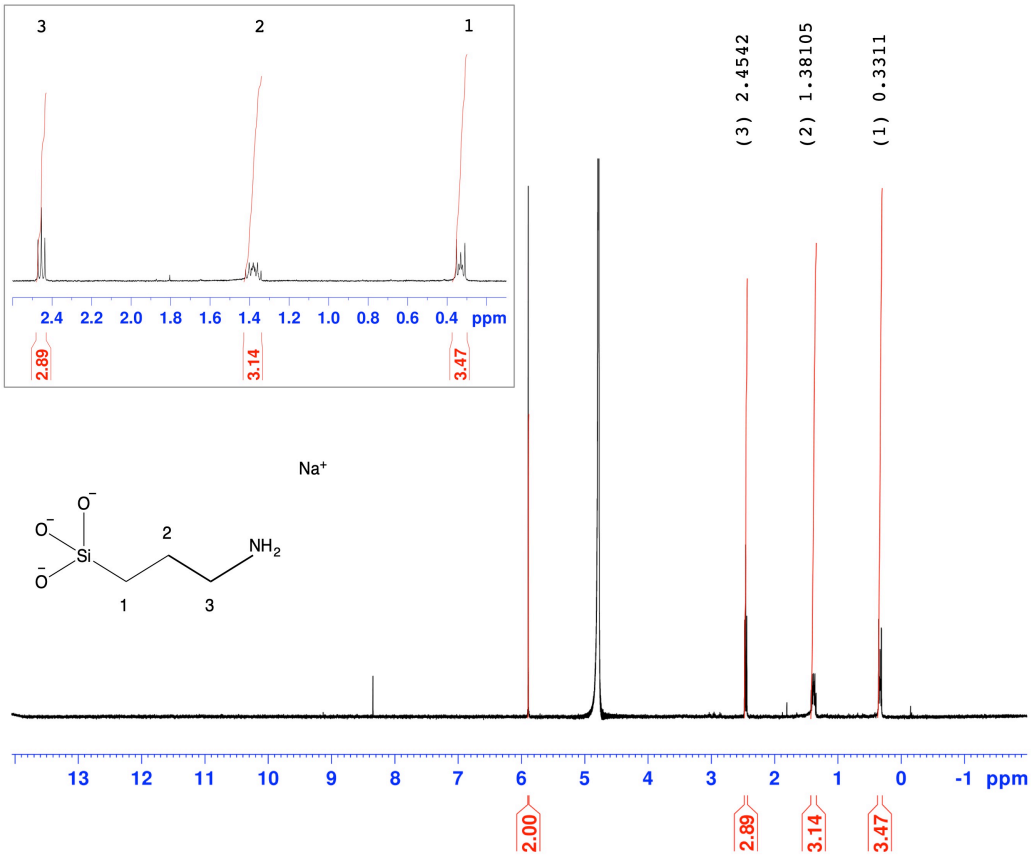

Figure 3A.20. ^{1}H NMR spectrum acquired from APTES@GW (1% APTES, plasma oxygen etching, batch 2 sample 3 reacted for 3h) in 0.4M NaOD solution compared to the internal standard of maleic acid (80 mmol) at 5.89 ppm.

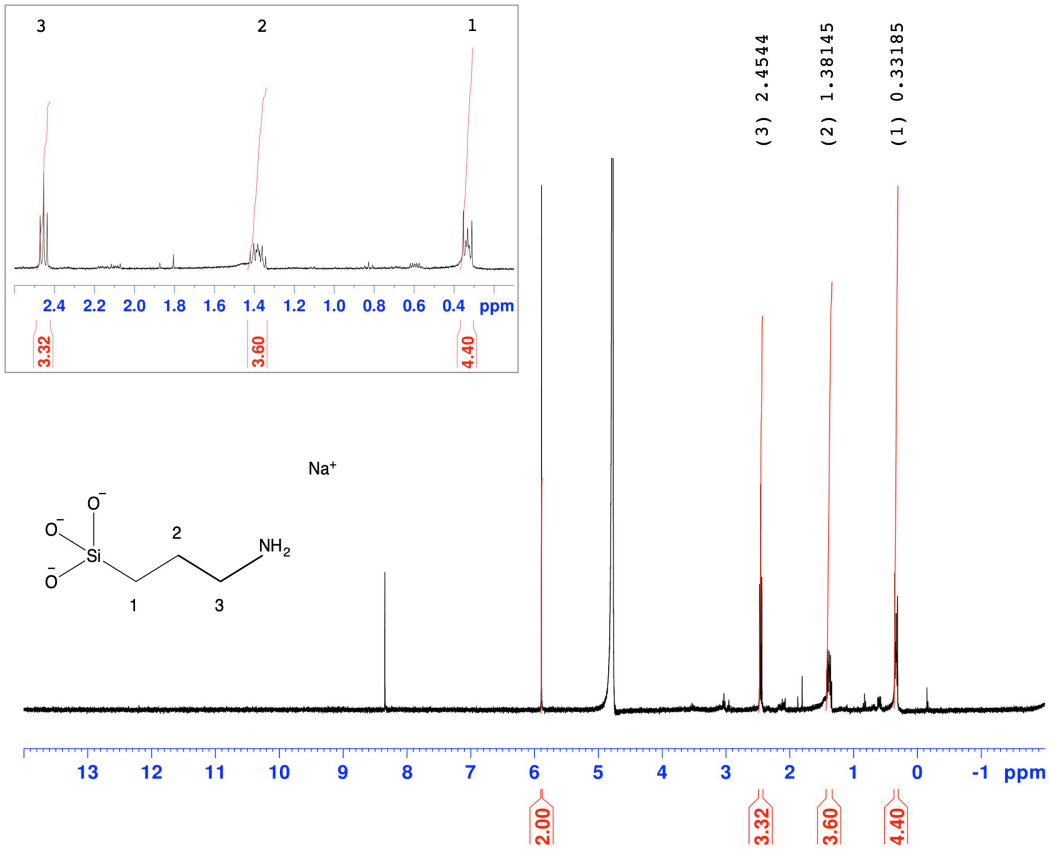

Figure 3A.21. ^{1}H NMR spectrum acquired from APTES@GW Sample 2 (1% APTES, plasma oxygen etching, sample 2 reacted for 3h, APTES treatment 1 week later after etching) in 0.4M NaOD solution compared to the internal standard of maleic acid (80 mmol) at 5.89 ppm.

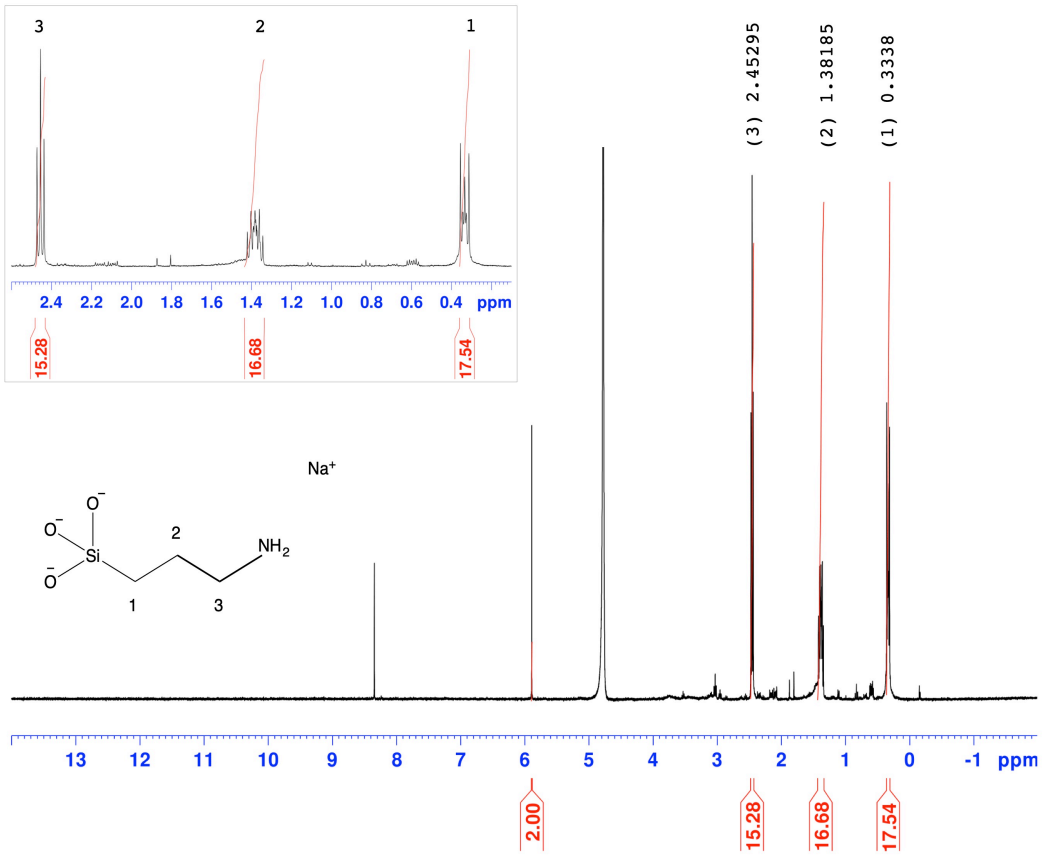

Figure 3A.22. ^{1}H NMR spectrum acquired from APTES@GW Sample 2 (1% APTES, plasma oxygen etching, sample 2 reacted for 3h, APTES treatment 1 week later after etching) in 0.4M NaOD solution compared to the internal standard of maleic acid (80 mmol) at 5.89 ppm.

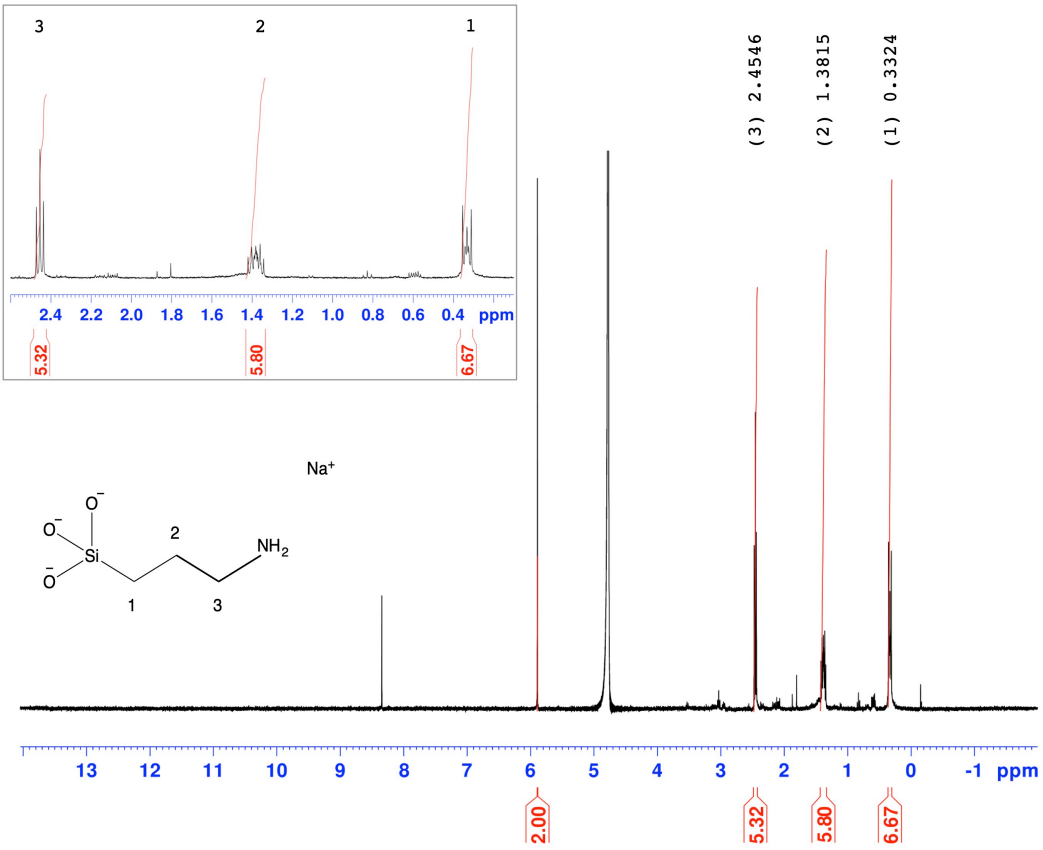

Figure 3A.23. ^{1}H NMR spectrum acquired from APTES@GW Sample 3 (1% APTES, plasma oxygen etching, sample 3 reacted for 3h, APTES treatment 1 week later after etching) in 0.4M NaOD solution compared to the internal standard of maleic acid (80 mmol) at 5.89 ppm.

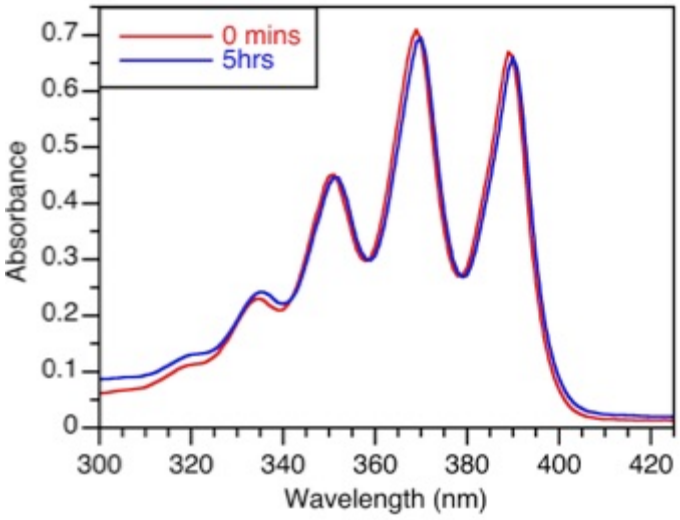

Figure 3A.24. 9,10-anthracenedicarboxylic acid (75 μM) upon 420 nm light irradiation (blue LEDi) in D_2O under air using APTES@GW.

References

1 S. Mulei, Water Quality Degradation Trends in Kenya over the Last Decade, *Water Quality Monitoring and Assessment*, 2012, pp. 509–51.

2 M. Qadir, D. Wichelns, L. Raschid-Sally, P. G. McCornick, P. Drechsel, A. Bahri and P. S. Minhas, The challenges of wastewater irrigation in developing countries, *Agric. Water Manag.*, 2010, **97**, 561–568.

3 S. Sharma and A. Bhattacharya, Drinking water contamination and treatment techniques, *Appl. Water Sci.*, 2017, **7**, 1043–1067.

4 J. Kim, Y. Chung, D. Shin, M. Kim, Y. Lee, Y. Lim and D. Lee, Chlorination by-products in surface water treatment process, *Desalination*, 2003, **151**, 1, 1–9.

5 H. Shi, G. Li, H. Sun, T. An, H. Zhao and P. K. Wong, Visible-light-driven photocatalytic inactivation of E. coli by Ag/AgX-CNTs (X=Cl, Br, I) plasmonic photocatalysts: Bacterial performance and deactivation mechanism, *Appl. Catal. B Environ.*, 2014, **158**–**159**, 301–307.

6 M. Thandu, C. Comuzzi and D. Goi, Phototreatment of Water by Organic Photosensitizers and Comparison with Inorganic Semiconductors, *Int. J. Photoenergy*, 2015, **2015**, 1–22.

7 T. Zhang, X. Wang and X. Zhang, Recent Progress in TiO_2-Mediated Solar Photocatalysis for Industrial Wastewater Treatment, *Int. J. Photoenergy*, 2014, **2014**, 1–12.

8 Ž. Lukšienė, New approach to inactivation of harmful and pathogenic microorganisms by photosensitization, *Food Technol. Biotechnol.*, 2005, **43**, 4, 411–418.

9 M. N. Chong, B. Jin, C. W. K. Chow and C. Saint, Recent developments in photocatalytic water treatment technology: A review, *Water Res.*, 2010, **44**, 10, 2997–3027.

10 Z. Luksiene, Photodynamic therapy: mechanism of action and ways to improve the efficiency of treatment., *Medicina (Kaunas).*, 2003, **39**, 12, 1137–1150.

11 C. H. Sibata, V. C. Colussi, N. L. Oleinick and T. J. Kinsella, Photodynamic therapy in oncology, *Expert Opin. Pharmacother.*, 2001, **2**, 6, 917–927.

12 J. Kou, D. Dou and L. Yang, Porphyrin photosensitizers in photodynamic therapy and its applications, *Oncotarget*, 2017, **8**, 46, 81591–81603.

13 P. Agostinis, K. Berg, K. A. Cengel, T. H. Foster, A. W. Girotti, S. O. Gollnick, S. M. Hahn, M. R. Hamblin, A. Juzeniene, D. Kessel, M. Korbelik, J. Moan, P. Mroz, D. Nowis, J. Piette, B. C. Wilson and J. Golab, Photodynamic therapy of cancer: An update, *CA. Cancer J. Clin.*, 2011, **61**, 4, 250–281.

14 Z. Malik, J. Hanania and Y. Nitzan, New trends in photobiology bactericidal effects of photoactivated porphyrins - An alternative approach to antimicrobial drugs, *J. Photochem. Photobiol. B Biol.*, 1990, **5**, 3-4, 281–293.

15 S. Rani-Beeram, K. Meyer, A. McCrate, Y. Hong, M. Nielsen and S. Swavey, A fluorinated ruthenium porphyrin as a potential photodynamic therapy agent: Synthesis, characterization, DNA binding, and melanoma cell studies, *Inorg. Chem.*, 2008, **47**, 23, 11278–11283.

16 J. S. Lindsey, in *Metalloporphyrins Catalyzed Oxidations. Catalysis by Metal Complexes*, 1994, pp. 49–86.

17 J. S. Lindsey, I. C. Schreiman, H. C. Hsu, P. C. Kearney and A. M. Marguerettaz, Rothemund and Adler-Longo Reactions Revisited: Synthesis of Tetraphenylporphyrins under Equilibrium Conditions, *J. Org. Chem.*, 1987, **52**, 5, 827–836.

18 J. S. Lindsey, Synthetic routes to meso-patterned porphyrins, *Acc. Chem. Res.*, 2010, **43**, 2, 300–311.

19 Z. C. Sun, Y. Bin She, Y. Zhou, X. F. Song and K. Li, Synthesis, characterization and spectral properties of substituted tetraphenylporphyrin iron chloride complexes, *Molecules*, 2011, **16**, 4, 2960–2970.

20 H. Shy, P. Mackin, A. S. Orvieto, D. Gharbharan, G. R. Peterson, N. Bampos and T. D. Hamilton, The two-step mechanochemical synthesis of porphyrins, *Faraday Discuss.*, 2014, **170**, 59–69.

21 A. Elhage, B. Wang, N. Marina, M. L. Marin, M. Cruz, A. E. Lanterna and J. C. Scaiano, Glass wool: a novel support for heterogeneous catalysis, *Chem. Sci.*, 2018, **9**, 33, 6844–6852.

22 R. I. Teixeira, N. C. De Lucas, S. J. Garden, A. E. Lanterna and J. C. Scaiano, Glass wool supported ruthenium complexes: Versatile, recyclable heterogeneous photoredox catalysts, *Catal. Sci. Technol.*, 2020, **10**, 5, 1273–1280.

23 A. D. Adleb, F. R. Longo, J. D. Finarelli, J. Goldmacher, J. Assour and L. Korsakoff, A Simplified Synthesis for Meso-Tetraphenylporphine, *J. Org. Chem.*, 1967, **32**, 2, 476.

24 F. Kunc, V. Balhara, A. Brinkmann, Y. Sun, D. M. Leek and L. J. Johnston, Quantification and Stability Determination of Surface Amine Groups on Silica Nanoparticles Using Solution NMR, *Anal. Chem.*, 2018, **90**, 22, 13322–13330.

25 W. Chidawanyika and T. Nyokong, Characterization of amine-functionalized single-walled carbon nanotube-low symmetry phthalocyanine conjugates, *Carbon N. Y.*, 2010, **48**, 10, 2831–2838.

26 A. H. Corwin, A. B. Chivvis, R. W. Poor, D. G. Whitten and E. W. Baker, The Interpretation of Porphyrin and Metalloporphyrin Spectra, *J. Am.*

Chem. Soc., 1968, **90**, 24, 6577–6583.

27 C. Pavani, A. F. Uchoa, C. S. Oliveira, Y. Iamamoto and M. S. Baptista, Effect of zinc insertion and hydrophobicity on the membrane interactions and PDT activity of porphyrin photosensitizers, *Photochem. Photobiol. Sci.*, 2009, **8**, 2, 233–240.

28 X. Huang, K. Nakanishi and N. Berova, Porphyrins and metalloporphyrins: Versatile circular dichroic reporter groups for structural studies, *Chirality*, 2000, **12**, 4, 237–255.

29 Y. Long, Z. Zhao, L. Wu, S. Luo, H. Wen, W. Wu, H. Zhang and J. Ma, Distinctive ligand effects of functionalized magnetic microparticles immobilizing palladium acetate as heterogeneous coordination catalysts for selective oxidation of styrene to acetophenone, *Mol. Catal.*, 2017, **433**, 291–300.

30 J. Düring and F. Gröhn, ZnO nanorods assembled with different porphyrins-size-tunable hybrid particles, *RSC Adv.*, 2017, **7**, 3321–3330.

31 P. G. Calzavara-Pinton, M. Venturini and R. Sala, Photodynamic therapy: Update 2006 Part 1: Photochemistry and photobiology, *J. Eur. Acad. Dermatology Venereol.*, 2007, **21**, 3, 293–302.

32 J. Klug, L. A. Pérez, E. A. Coronado and G. I. Lacconi, Chemical and electrochemical oxidation of silicon surfaces functionalized with APTES: The role of surface roughness in the AuNPs anchoring kinetics, *J. Phys. Chem. C*, 2013, **117**, 21, 11317–11327.

33 S. Mapukata, A. S. Hainer, A. E. Lanterna, J. C. Scaiano and T. Nyokong, Decorated titania fibers as photocatalysts for hydrogen generation and organic matter degradation, *J. Photochem. Photobiol. A Chem.*, 2020, **388**, 112185.

34 Y.-Y. Song, H. Hildebrand and P. Schmuki, Optimized monolayer grafting of 3-aminopropyltriethoxysilane onto amorphous, anatase and rutile TiO_2, *Surf. Sci.*, 2010, **604**,3-4, 346–353.

35 J. Spadavecchia, C. Méthivier, J. Landoulsi and C. M. Pradier, Interaction of ZnII porphyrin with TiO_2 nanoparticles: From mechanism to synthesis of hybrid nanomaterials, *ChemPhysChem*, 2013, **14**, 11, 2462–2469.

36 E. Y. Jeong, M. B. Ansari, Y. H. Mo and S. E. Park, Removal of Cu(II) from water by tetrakis(4-carboxyphenyl) porphyrin-functionalized mesoporous silica, *J. Hazard. Mater.*, 2011, **185**, 2-3, 1311–1317.

Chapter 4
Lignin@TiO_2 nanocomposites for applications in sunscreens

Introduction

4.1 Sunscreens

Sunscreens are formulated to provide a protective layer on the skin and prevent damage, such as sunburns and skin cancer. Ultraviolet radiation (UVR) is composed of UVA rays (320-400 nm), UVB rays (280-320 nm), which are partially absorbed by the ozone layer and UVC (< 280 nm) rays that are stopped by the ozone layer. Overexposure to UVB and UVA is the main cause for signs of photo-aging, sunburns and skin cancers.[1] Protection in sunscreens from the ultraviolet radiation emitted by the sun is often separated into two major categories: chemical and physical (also called mineral filter).

4.2 Chemical filters

Chemical filters are used to absorb incident rays from UV sunlight radiation. Chemical absorbers are often organic molecules that can be further subdivided depending on if they are either UVA (benzophenones, dibenzoylmethanes) or UVB (PABA derivative and cinnamates) filters.[2] UV light absorption by organic molecules is due to the part of the molecular structure called a chromophore, which can either encompass only a part of the molecule or the entirety of it. Chromophores are generally associated with delocalized π-electrons in conjugated systems. When a molecule absorbs a photon whose energy is high enough, an electron is promoted form a lower energy level to a higher one, going from a ground state to an excited state (Figure 1).[3]

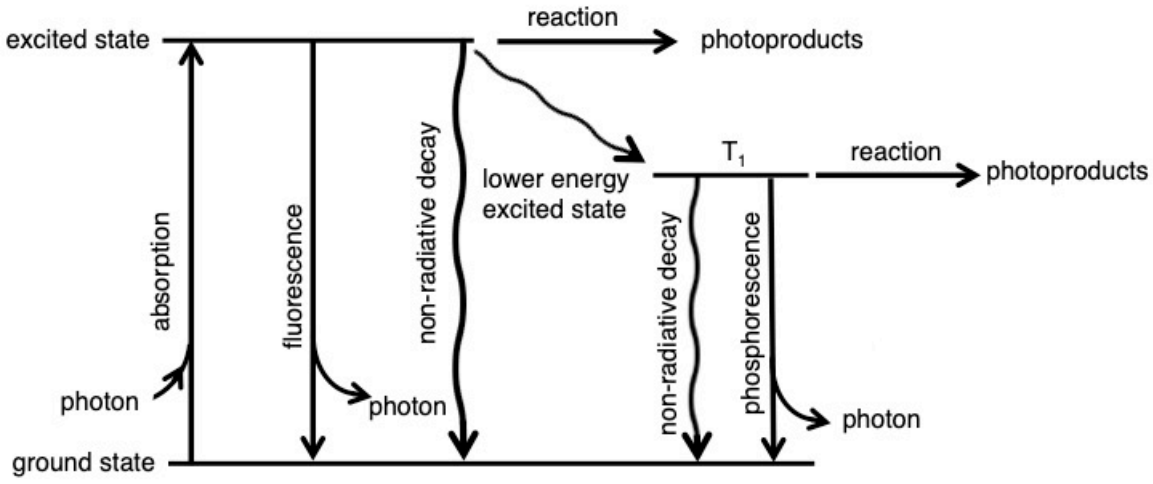

Figure 4.1. A simplified Jablonski diagram indicating the energies associated with ground and photochemically excited states.

It is very important that the active ingredient is photostable and will not form reactive oxygen species (ROS) or other harmful intermediates while absorbing solar energy but will rather dissipate that energy through different photochemical and photophysical pathways. Pathways that produce ROS or reactive intermediates can potentially penetrate the skin and can further penetrate into the epidermis and cause damage to the DNA.[4,5]

Historically, many commercial formulations have contained the active ingredient p-aminobenzoic acid (PABA) due to its high efficiency to absorb within the UVB region. However, PABA was later removed from sunscreen formulations when it was discovered that PABA can induce damage to DNA and cause dimer formation in cell populations when exposed to various wavelengths of light.[6–8]

4.3 Sun protection factor (SPF)

In most occasions, chemical filters are combined with physical filters because the use of only one active agent will not provide a high enough “sun protection factor” (SPF) or broad-spectrum absorption at levels that are permissible by FDA regulation.[2] Additionally, combinations of UVA/UVB chemical

filters are closely regulated since the inappropriate combination can cause photoinstability or negative synergistic interactions between active agents.[9,10]

SPF is the UV energy (UVB radiation) that is needed to produce a minimal erythema dose (MED) on sunscreen-protected skin compared to the necessary UV energy dose required to produce a MED on non-protected skin, given by the equation below[3]:

$$\mathrm{SPF} = \frac{\mathrm{MED\ protected}}{\mathrm{MED\ unprotected}} \quad (1)$$

MED is the lowest time interval or dosage of UV light irradiation sufficient to produce a minimal, perceptible erythema on unprotected skin.[11]

For example, a sunscreen with SPF-15 means that 1/15 of the radiation that would burn skin penetrates the recommended thickness of sunscreen, or in other words, SPF-15 has the ability to block 94% of UVB radiation.

4.4 Physical/Mineral filters

Many formulations contain a combination of chemical and physical filters, where the latter will reflect, absorb and scatter the incident radiation. TiO_2 and ZnO are often employed as physical protection due to their opaque nature.[3] TiO_2 provides better absorption in the UVB while ZnO can also absorb in the UVA region. Moreover, these semiconductors provide the additional benefit of good chemical stability and are relatively inexpensive materials.

In 2019, the FDA proposed that of the current 16 active ingredients that are on the market, zinc oxide and titanium oxide are ”generally recognized as safe and effective” (GRASE) for use in sunscreens. Due to safety concerns, PABA and trolamine salicylate are 2 ingredients that have been determined to not be GRASE for sunscreens. The other 10 ingredients do not have enough sufficient safety data to make a positive GRASE determination.[12]

However, microsized TiO_2 and ZnO have high refractive indexes that

expand the UV and visible spectrum.[13,14] This results in a phenomenon known as the whitening effect, where particles produce an unwanted iridescence and brightness effect. Therefore, the particles have been reduced in size to the nanoscale level (<100 nm). This tactic has lead to increased concerns due to the fact that as the semiconductors size changes, so can other characteristics, including the particles ability to protect from UV and its phototoxicity.[15]

4.5 Phototoxicity and instability of inorganic nanomaterials in sunscreens

There has been some concern regarding the penetration of TiO_2 nanomaterial and the consequential toxicity that this can cause. One study detected increased levels of Ti in the livers of mice that were treated with sunscreen containing TiO_2 nanoparticles when compared to a control that had not been treated. It was also found that the exposure to the UVR did not significantly impact the concentration of Ti in the examined tissue.[16]

TiO_2 can efficiently absorb UV light and form radicals such as superoxides and hydroxyl radicals that can cause damage to the skin and can also initiate oxidations.[17] Light at energies that are equal to or below the wavelength absorbed by the TiO_2 will contain enough energy to promote electrons from the valence band (VB) to the conduction band (CB). The generated single electrons can react with oxygen and the positively charged holes that can react with hydroxyl ions or water to form reactive oxygen species (ROS) such as superoxide and hydroxyl radicals[18]:

$$TiO_2 + h\nu \rightarrow TiO_2\,(e/h) \rightarrow e\,(CB) + h^+(VB) \quad (2)$$

$$e^-(CB) + O_2 \rightarrow O_2^{\cdot-} \rightarrow HO_2^{\cdot} \quad (3)$$

Majority of toxicological concerns regarding the risk of nanoparticles comes from inhalation where the particles can deposit in the respiratory tract.[19] However, similar to the chemical filters, the ROS generated by the TiO_2 and ZnO based sunscreens can cause potential harm to the skin by penetrating the layers

of skin.[20] ROS generated can not only cause cellular damage but can also negatively effect the lifetime of the product by photodegrading the other emulsion components in the sunscreen.[21]

Even with these concerns, the use of sunscreen lotions is still the principal first line of protection against exposure to harmful solar UV radiation. Discovering a method to eliminate the formation of free radicals produced by TiO_2 exposed to sunlight, oxygen and water has proven quite challenging. Recently, CeO_2-based nanocomposites have been proposed as a suitable alternative to TiO_2 and ZnO in sunscreen formulations. While the UV blocking capability and particle size of these semiconductors are suitable for cosmetic purposes, catalytic oxidation of the particles restricts its application in commercial sunscreens.[22]

An alternate solution that is currently being explored is the use of biomolecules or other molecular structures that can limit the interaction between the free radicals generated and the skin rather than replace the inorganic material used. For instance, TiO_2 modified with carbon on the surface demonstrated the ability to reduce the ROS generated by the TiO_2 powder.[23] Another approach that has been employed is the encapsulation of the TiO_2 nanoparticles with biomolecules including chitosan[24] and morin[25] (plant flavonoid).

Similarly, the Scaiano group was able to coat TiO_2 in a thin shell of lignin (denoted as lignin@TiO_2), which is one of the most abundant natural polymers. Lignin in nature forms a key part of the structural materials in cell walls of plants and some algae.[26] The lignin coating does not attempt to stop the production of the free radicals or narrow the band gap but rather traps the ROS and blocks their release into the surrounding environment. Lignin is a complex structure that is comprised of aromatic moieties, where the main building blocks of hydroxycinnamyl alcohols (or monolignols) coniferyl alcohol and sinapyl alcohol, and few amounts of p-coumaryl alcohol.[27] A general structure for lignin is shown in Figure 4.2.

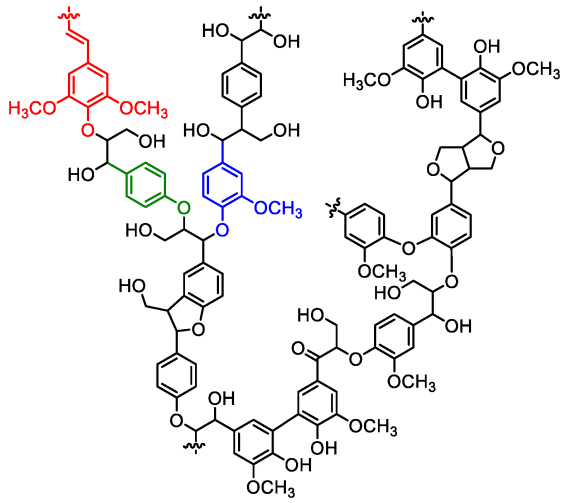

Figure 4.2. General schematic representation of the macromolecular structure of lignin where some major aromatic moieties are colored: sinapyl alcohol (red), guaiacyl alcohol (blue) and *p*- courmaryl alcohol (green). Reproduced with permission from M. S Karunarathna and R. C. Smith[28] (2020) Sustainability.

This allows the lignin to utilize its antioxidant properties and scavenge radicals formed by the TiO_2. Moreover, lignin is a low cost material, biocompatible, found to be undamaging to human health and has antimicrobial properties.[29,30] The Scaiano group demonstrated that the TiO_2 generated ROS in the presence of water under UVA irradiation and that the lignin@TiO_2 nanocomposites were able to dramatically reduce the photocatalytic capability of TiO_2. They also determined that the nanocomposites improved the photoprotection of other ingredients commonly found in sunscreen formulations.[26] Here, we attempted to scale up production of the lignin@TiO_2 nanocomposites for applications in industry and further characterize the nanoparticles.

Additionally, antibacterial and biocompatibility assays using fibroblast were attempted, however, we encountered a few obstacles that did not produce substantial results. There are few reports indicating that lignin contains antibacterial properties.

4.6 Materials and methods

Reagents. Unless otherwise specified, all chemicals were purchased from Sigma-Aldrich or Fisher Scientific and used without further purification. Different lignins were gifted by FPInnovations. TiO_2 P25 was purchased from Univar Canada. TiO_2 P90 was a gift from Evonik Degussa.

Standard synthesis of particles

10 mg of lignin with 10 mg TiO_2 were combined in 5 mL of solvent (alkali aqueous solution of NaOH in Milli-Q water, pH 12) and stirred for an hour prior to irradiation. The slurry was placed in a quartz test tube and subjected to UVA light (369 nm LED) irradiation for 2 h while vigorously stirring. The slurry was separated by centrifugation at 8000 rpm for 15 min, at 22°C and nanoparticles were washed 3 times. The first and second washes used alkali solution (pH 12) to remove any unbound lignin and the last wash was with Milli-Q water, to remove any alkali solution. Any changes to washing cycle are noted, as needed. The particles were dried under desiccation and grounded into a fine powder.

Scale up synthesis of particles (flow system)

Scale up synthesis of the lignin nanoparticles was achieved using a flow reaction setup with slight changes to the light source used (as described in the paragraphs below). As shown in scheme 4.1, the solution mixture of the lignin and TiO_2 was in a glass bottle, under constant stirring. Solution was pumped out of the glass bottle reservoir using a closed loop Teflon tube using a peristaltic pump that circulates the sample. The tubing was connected to a container (either metal or plastic, as indicated) through a small port near the bottom or middle of the container. The sample within the container was irradiated with UVA light source from open top of the container. The sample then flowed out from the output port connect to another Teflon tube and flowed back into the reservoir using gravity. Any modifications made to the system set up were mentioned, as needed.

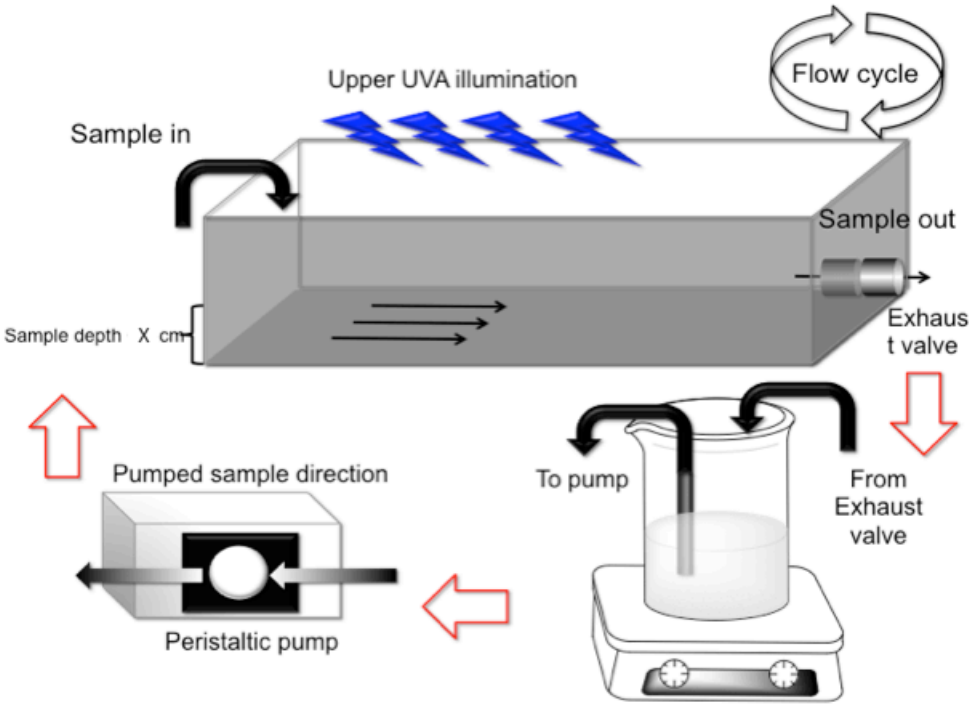

Scheme 4.1. Schematic of flow system design for scaled- up reaction to synthesize A lignin@TiO_2 nanoparticles.

Scale up synthesis of particles (UVA panel)

In the first attempts at increasing the lignin- modified nanoparticle product, 3(6) g of lignin with 1(2) g TiO_2 were combined in 1(2) L of solvent (alkali aqueous solution of NaOH in Milli-Q water (pH 12)) and stirred under heat (~ 60°C) for 1 h prior to irradiation. Solution was illuminated using an exposure panel containing 5 UVA bulbs at a distance of 1.5 cm above the sample, as shown in figure 4.3. Irradiation time of the slurry in the flow reaction was 16(24) h.

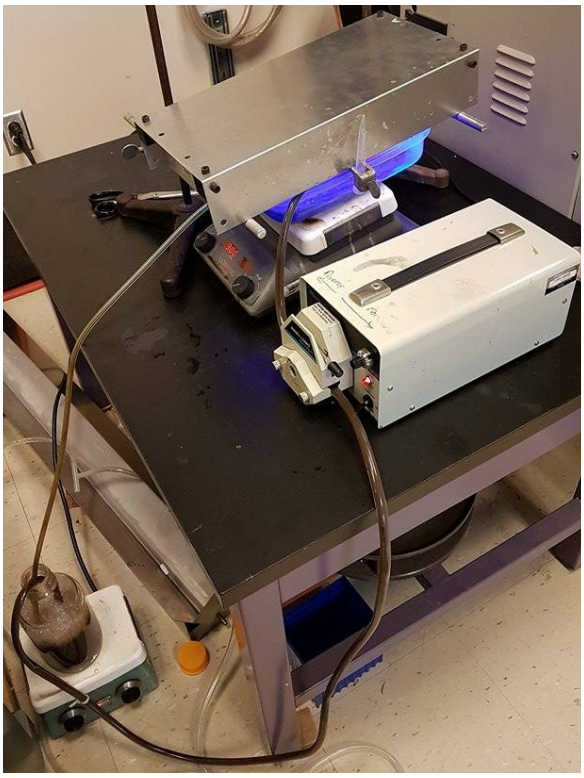

Figure 4.3. Set up of scaled- up reaction for the large batch synthesis of Hinton A lignin@TiO_2 nanoparticles irradiated with UVA light from an exposure panel.

In a second attempt to increase the lignin- modified nanoparticle product, 6 g of lignin with 2 g TiO_2 were combined in 2 L of solvent (alkali aqueous solution of NaOH in Milli-Q water, pH 12) stirred under heat (~ 60°C) for an hour prior to the reaction. Slurry was irradiated using 4x 40 W UVA bulbs, at a distance of 8 cm from the sample, in an open trough within a flow system. Irradiation time of the flowing solution was 24 h. Figure 4.4 shows a system that was inspired by the original. In this figure, it can be seen that there are 3 sets of lamps with 12 bulbs, rather than 4 bulbs that sit above and below the solution. Another difference is that the reaction occurs and travels in glass tubes rather than the metallic containers.

Figure 4.4. Similar set up of scaled- up reaction for the large batch synthesis of Hinton A lignin@TiO_2 nanoparticles irradiated with UVA light from 3 stations, each with 4x 40 W bulbs.

The third and final set-up attempt utilized 4.5 g of lignin with 4.5 g TiO_2 were combined in 1.5 L of solvent (alkali aqueous solution of NaOH in Milli-Q water, pH 12). Slurry was also heated (~ 60°C) before the reaction and irradiated for 6 h using two exposure panels 1.5 cm from the reaction vessel (5 UVA bulbs on bottom + 5 UVA bulbs on top of a condenser flowing solution), as shown in Figure 4.5.

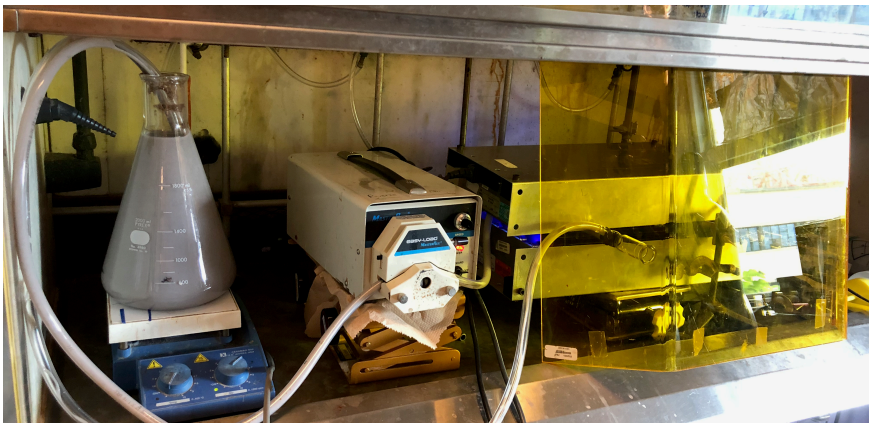

Figure 4.5. Set up of scaled- up reaction for the large batch synthesis of Hinton A lignin@TiO_2 nanoparticles irradiated with 2x exposure panels, for upper and lower UVA light irradiation.

Photocatalytic oxidation of 2-propanol

Photocatalytic activity of the nanoparticles was investigated using an established methodology that evaluates how the lignin modification can inhibit the photocatalytic activity of TiO_2.[26,31] Isopropanol was photo-oxidized to acetone under combined UVA and UVB irradiation (10 UVA lamps and 4 UVB lamps) at 35-38°C. Control experiments under dark conditions were carried out using TiO_2, lignin and lignin@TiO_2 showing no reaction. The conversion of an aqueous solution of 2-propanol (5 mM) under stirring was examined in the presence of TiO_2, lignin and several lignin@TiO_2 nanoparticles (2 mg/mL). The experiments were conducted over a 4 h period, where 1 mL aliquots were collected from a 5 mL solution every hour. Aliquots were centrifuged at 7000 rpm, for 10 min at 20°C. Supernatant (800 µL) was used to record the ^1H NMR spectrum using the water suppression sequence, with the presaturation signal centered at 4.706 ppm (proton signal of H_2O) in the presence of 3-(trimethylsilyl)-2,2,3,3-tetradeuteropropionic acid (sodium salt) (TMSP) in D_2O as the external standard. The degradation of irradiated isopropanol over time was analyzed using a previously fitted calibration curve.

Electron paramagnetic resonance (EPR) spectroscopy

Investigation of trapped electrons and holes was conducted by electron paramagnetic resonance (EPR) spectroscopy. TiO_2, lignin and lignin@TiO_2 nanoparticles (2 mg/mL) powders in a solution of 1 mM of DMPO in THF were irradiation with UV light using a filter cutting of irradiation below 305 nm for various amounts of time, at room temperature.

Fourier transform infrared spectroscopy (FT-IR)

FT-IR measurements were taken using Shimadzu FTIR 8400s equipped with MIRacleTMATR. Each scan recorded 50 scans, in the range from 500 to 4000 cm^{-1} with a resolution of 4 cm^{-1}.

Dynamic light scattering (DLS) measurements

The zeta potential of TiO_2 and lignin nanoparticles were measured in different media, phosphate- buffered saline (PBS) and Luria-Bertani (LB) broth, or a combination of both, at a concentration of 0.1 mg/mL.

Instrumentation

A High Efficacy 368 nm 11W UV LED Emitter LZ4-00U600 was used to synthesize the particles under irradiation.

Photocatalytic oxidation of 2-propanol experiments were conducted using a Luzchem CCP-4V customized computer-controlled photoreactor, with temperature control was used with 10 UVA lamps and 4 UVB lamps.

Electron paramagnetic resonance (EPR) spectra were recorded on a Bruker EMXplus (X-band) equipped with an ER 4119HS cavity at room temperature with a modulation of 2G and irradiated with a LIGHTNINGCURE Spot light source LC5 with a filter cutting of irradiation below 305 nm.

Zeta potential of TiO_2 and lignin@TiO_2 solutions were measured using a Malvern Zetasizer Nano ZS at 20 ºC in a disposable capillary cell. The values reported correspond to triplicate readings of each batch.

Diffuse reflectance (DR) measurements were carried out in VARIAN Cary 7000 UV-VIS Spectrophotometer coupled with an integrating sphere accessory.

Thermogravimetric analysis (TGA) was carried out using a TGA Q500 from TA instruments, from ambient temperature to 600-1000 ºC, at a heating rate of 10 ºC/min. and under a constant nitrogen flow of 25 mL/min.

^{1}H analysis was carried out in a Bruker Advance II 300MHz NMR spectrometer with an appropriate pulse sequence with a spectral width of -0.5 ppm to 12.5 ppm and with the pre-saturation signal centered at 4.706 ppm (proton water signal).

4.7 Results and Discussion

Characterization of lignins by FPInnovations

After the successful production and investigation of the lignin@TiO_2 nanoparticles synthesized by UVA LED, the group was gifted four different alkali lignins by FPInnovations. During the isolation of lignin, it undergoes a number of complex reactions, which alters the final structure of the lignin. The pulping process results in many of the aryl ether bonds found within the lignin complex and can condense uncertain structures containing stable C-C bonds.[32] Therefore, we were required to analyze each different sample and decide which lignin would be chosen to use for future scaled-up manufacturing of the lignin@TiO_2 nanoparticles. The lignins are denoted as such: Hinton A lignin, HW lignin, K31 lignin and ZHL-10 lignin. Each sample was different in their appearance and texture, as shown in Figure 4.6. The K31 lignin was a very dark brown, almost black colour, and had a course powder. The HW lignin was a very fine, dark brown powder. The Hinton A and ZHL-10 lignins were a similar shade of pale brown and had a similar powder texture. The final general appearance of the

nanoparticles needed to be taken into consideration. Most sunscreens and cosmetics are white, and become sheer as it is rubbed into the skin. It is important that these particles can produce a similar effect while in cream formulation.

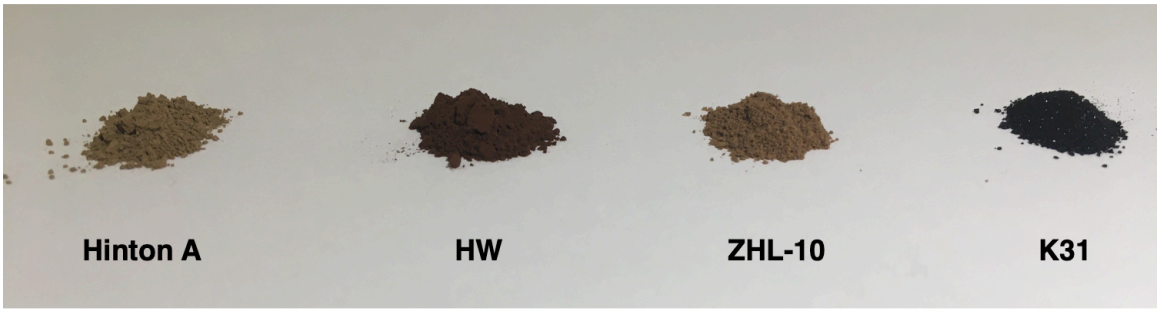

Figure 4.6. Picture of different lignin powder samples by FPInnovations.

Thermal stability of lignins

The thermal degradation of the lignin occurs in three stages, where the initial phase took place at 30-120 °C where water is evaporated and the volatilization of small impurities. The second stage occurs around 180-400 °C, where the lignin degradation begins, and components of carbohydrates and other aliphatic compounds in the samples are removed. The third stage takes place over a wide range above 450 °C and was the active stage of lignin polymer pyrolysis. In this final stage, volatile products are being removed including alcohols, phenols and aldehyde acids.[33] Additionally, lignin samples can still retain 30-40 wt.% of the lignin after 1000 °C, which can be attributed to the formation of condensed aromatic structures in the lignin. TGA of the four alkali lignins are plotted in Figure 4.7. Each lignin produces a similar curve, however, only the Hinton A and HW lignin completely degrade at 800°C. Since TGA is being used to quantify the wt.% of lignin on the nanoparticle, it would be easiest to do so with a lignin that completely degrades during the thermal analysis. Information extracted from TGA spectra (Figure 4.7) is summarized in Table 4.1.

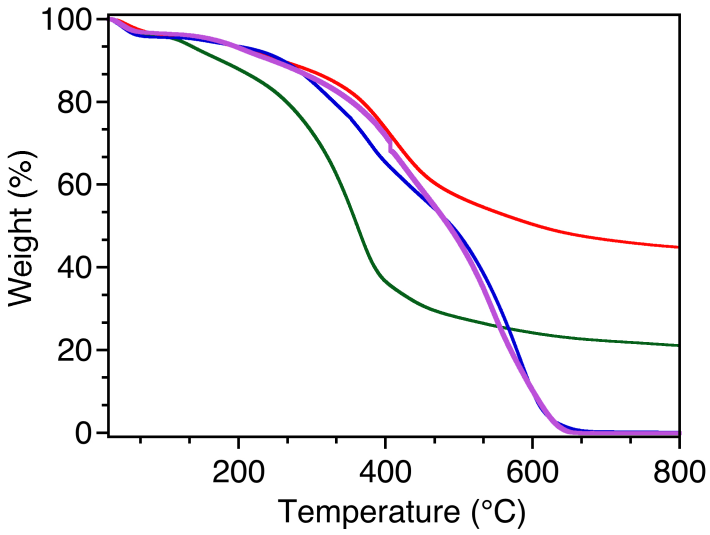

Figure 4.7. TGA of ZHL-10 lignin (3.86 mg, green), K31 lignin (4.26 mg, red) A lignin (3.42 mg, purple), HW lignin (4.49 mg, blue).

Table 4.1. Information of different types of lignin by FPInnovations from TGA analysis.

Types of lignin	Approx. Lignin (%) on NPs	Water (%)	Mass Lost (%) at 800°C
Hinton A	2.7	2	100
HWL	2.3	2.1	100
ZHL-10	18	2	79
K31	2.5	2	55

Functional groups analysis

Lignin samples were analyzed using FTIR, as show in Figure 4.8, and demonstrated similar spectra to those reported in literature.[33,34] There are some characteristic peaks that can be observed in the IR spectrum. Here, we can observe the sp^3 C-H stretching at 2900 cm^{-1}, C=O stretching at 1600 cm^{-1} and aromatic ring bending below 1500 cm^{-1}.[26] These results can help demonstrate the functionalization of TiO_2 using lignin by using the aforementioned peaks to confirm the presence of the organic molecule on the TiO_2.

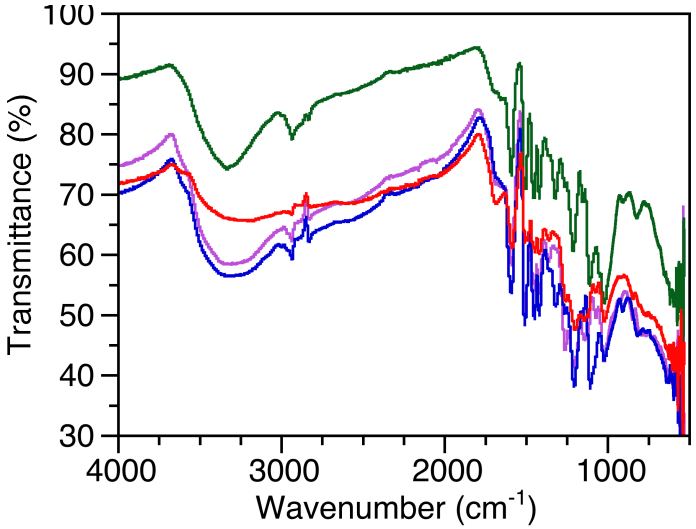

Figure 4.8. FT-IR of ZHL-10 lignin (green), K31 lignin (red), Hinton A lignin (purple), HW lignin (blue).

Diffuse reflectance spectroscopy

The DR spectra in Figure 4.9, demonstrates that lignin absorbs light beyond the UV range. Each of the lignin samples absorbed light in the visible range (greater than 400 nm) to varying degrees. It was previously discovered that the TiO_2 modified with the lignin could have a slightly extended absorption into the visible light region. As previously mentioned, the K31 lignin is an almost black colour which making it not suitable for cosmetics, therefore it was omitted from DR spectroscopy. Spectra's in DR plot are normalized to Hinton A lignin, since that was the lignin that was chosen.

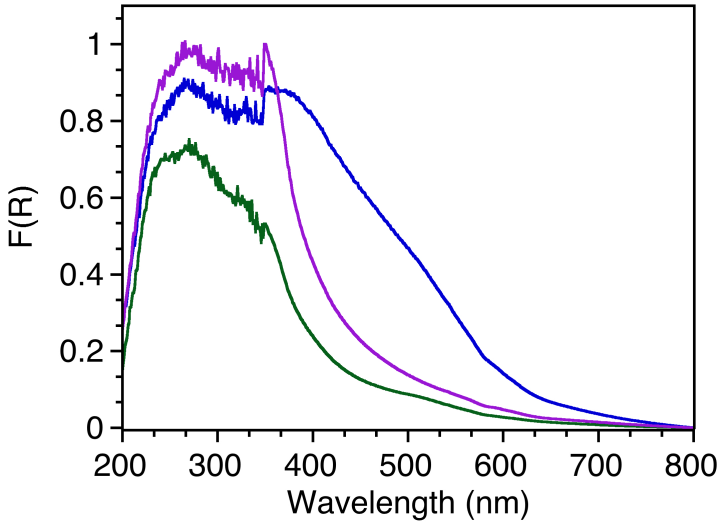

Figure 4.9. DR normalized at λ=266 nm of ZHL-10 lignin (green), Hinton A lignin (purple), HW lignin (blue).

Next we investigated the wt.% of lignin coating the nanoparticles using the different samples. The same methodology was used that was previously reported, however, the lignins by FPInnovations are not soluble in water. Therefore, a NaOH solution (pH 12) was used as the solvent to synthesize the nanoparticles. The alkali solution was also in the initial washes of cleaning the nanomaterial, rather than water. As can be seen in Table 4.1, in general the lignins gave a similar coating (%) on the P25 TiO_2. This was determined using TGA, since only the organic coating will thermally decompose under inert conditions. All lignins produced a different lignin (%) coating on TiO_2 (Appendix Figure 4A.1).

Photocatalytic Oxidation of 2-Propanol

In the previous report, the photocatalytic activity of TiO_2 was measured using a well known process where alcohols are oxidized to ketones.[26] They were able to examine the photocatalytic activity of TiO_2 modified with the lignin by evaluating the conversion of 2-propanol to a ketone, as shown in Scheme 4.2.

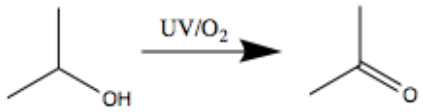

Scheme 4.2. Photocatalytic oxidation of 2-propanol.

Here, the same methodology was used to evaluate the photocatalytic properties of the nanoparticles synthesized in the presence of different lignins and the nanoparticles produced from the scaled up process. Isopropanol is in an aqueous solution with the particles were irradiated under UVA/UVB light at a controlled temperature of 35-38 °C. There were varying amounts of 2-propanol (%) remaining in the samples containing the coated nanoparticles. It can be seen that the K31 lignin @ TiO_2 photodegraded the isopropanol the most, whereas the rest of the particles showed similar performance, with the Hinton A lignin demonstrating slightly higher protection of the alcohol, as shown in Figure 4.10.

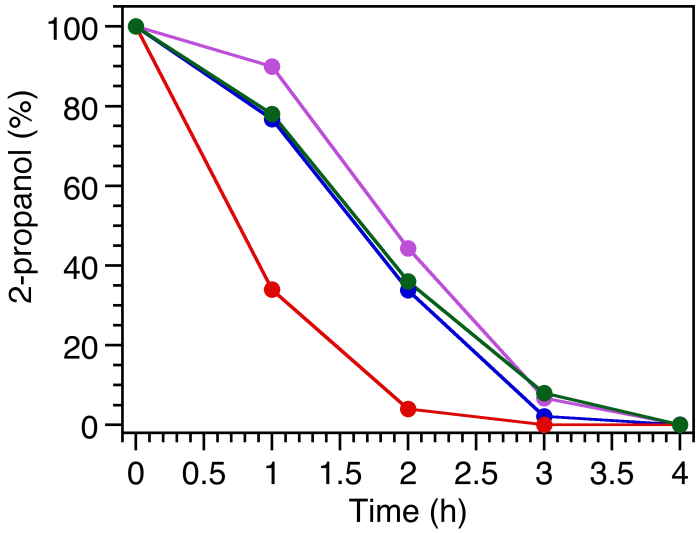

Figure 4.10. Percentage of 2-propanol remaining upon UVA−UVB irradiation in the presence of different particles, Hinton A lignin@TiO_2 (purple), HW lignin@TiO_2 (blue), K31 lignin@TiO_2 (red) and ZHL-10 lingin@TiO_2 (green).

With the consideration of the appearance of the lignin sample, the complete degradation of the sample and the higher photoprotection of 2-propanol from the free radicals, Hinton A lignin was chosen to be continued to be studied

and to use it for scaling up the synthesis of the lignin@TiO_2 nanoparticles. Although ZHL-10 sample had similar conversion rates to Hinton A lignin, the former required less lignin on the TiO_2 to trap the free radicals generated by the TiO_2.

Hinton A lignin@ TiO_2 nanoparticles and scale up reactions.

We created the Lignin@TiO_2 nanoparticles with a large batch of Hinton A lignin received from FP innovations using the same methodology used previously by the group. These nanoparticles had a similar wt.% coating of lignin on TiO_2. We found there was variability in wt.% coating from each sample synthesized, with an average being between 2-5% of lignin on the TiO_2 (Appendix figure 4A.4). The Hinton A lignin nanoparticles appeared beige in colour (Figure 4.11), which is acceptable for cosmetic standards.

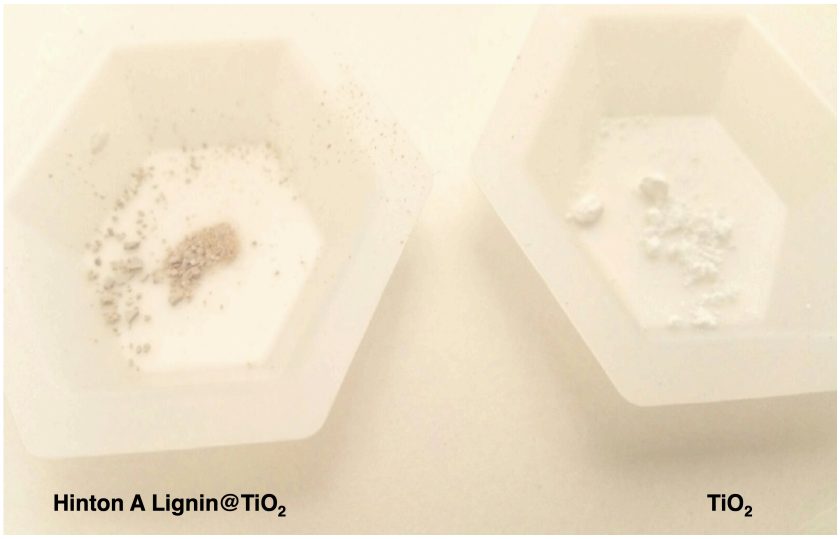

Figure 4.11. Picture of Hinton A lignin@TiO_2 (3 wt.% lignin) nanoparticles and P25 TiO_2 powder.

The IR spectra of TiO_2 demonstrated characteristic bands at 3300 cm^{-1} corresponding to the OH stretching. Additionally, the broad peak between 1000-500cm^{-1} is assigned to Ti-O-Ti stretching bonds, which is the characteristic peak of TiO_2. The lignin bands previously mentioned are apparent in the IR spectrum of the Lignin@TiO_2 nanoparticle sample (Figure 4.12), demonstrating that there

is lignin present on the nanoparticle. DR spectra in Figure 4.13 show that the presence of lignin in the particles is able to slightly extend the absorption of the TiO_2 into the visible range (which typically absorbs below 400 nm). Based on the paper by Makula *et al.*, the band gap of the lignin nanoparticles was estimated by correcting the baseline and using the intersection of the two fitting lines of TiO_2 and lignin because the absorption of lignin is very high.[35] The resulting estimated band gap of the lignin nanoparticles was 3.14 eV. This value is similar to the band gap of TiO_2 (3.2 eV) which means that the light absorption properties of the TiO_2 were barely changed by the addition of lignin.[36] This is important because the photo-absorbing properties of the physical ingredient in sunscreens needs to either remain the same or improve for their use in sunscreens.

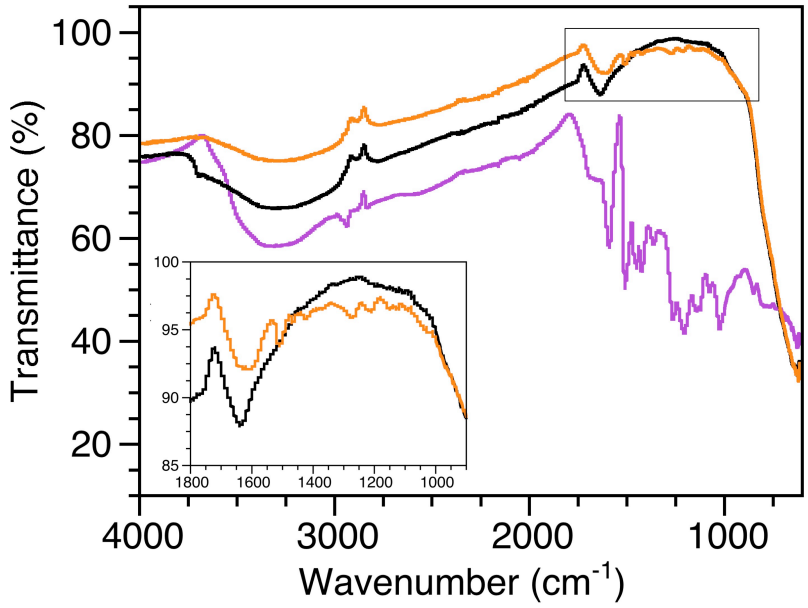

Figure 4.12. FT-IR spectra of Hinton A lignin (purple), TiO_2 (black) and Hinton A lignin@TiO_2 (orange).

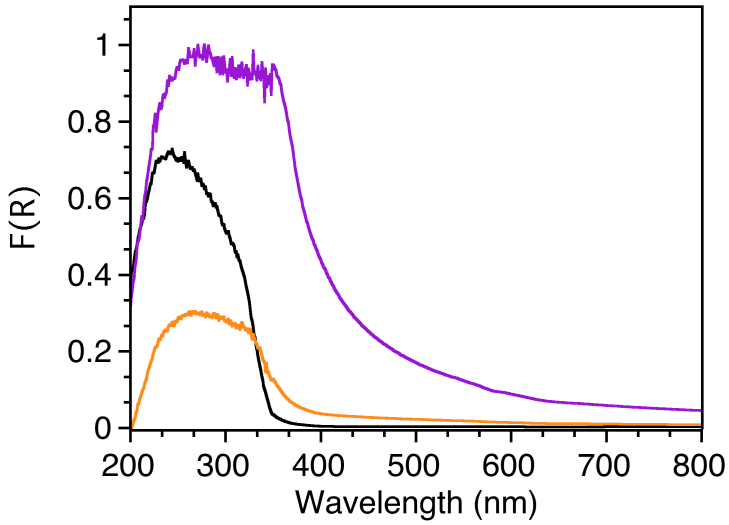

Figure 4.13. DR spectra normalized at λ=271 nm of Hinton A lignin (purple), Hinton A Lignin@TiO_2 (orange) and TiO_2 (black).

Scale up of Hinton A lignin@TiO_2 nanoparticles

After synthesis of the nanoparticles using the LED was conducted, scale-up synthesis was done to provide a large enough batch to industry partners. The first scale up batch was conducted using an exposure panel (Figure 4.3). The flow reaction took place using the basic design shown in Scheme 4.1. For this reaction set up, the reactant was flowed into a reaction vessel (plastic container), with the exposure panel sitting on top. In order to not have much of solution stagnant in the reaction vessel, the container was placed at an angle so the solution remained near the input and output ports and was under constant stirring within the container. Due to the low wt.% of lignin coating the TiO_2, the ratio of lignin to TiO_2 was changed from 1:1 to 3:1 (w/w) to try to improve the coating of the nanoparticles. In our first large scale reaction, 3 g of lignin and 1 g of TiO_2 was irradiated for 16 h.

Due to the increase in free base lignin in the reaction, the cleaning process of the nanoparticles was adjusted to remove the extra lignin in the solution, and more centrifugation cycles using alkali lignin were added to the process.

A batch using the same ratios was attempted and irradiated the sample for 24 h rather than 16 h, to examine if adding more time to the irradiation reaction could increase the amount of lignin. As can be seen in the TGA results in Figure 4.14, both reactions resulted in similar wt.%, with the first attempt producing 3.2 wt.% and other being 3.4 wt.% This reaction produced nanoparticles containing a similar wt.% of lignin to that of small batch samples, which demonstrates that scale up this reaction is possible using a flow system approach.

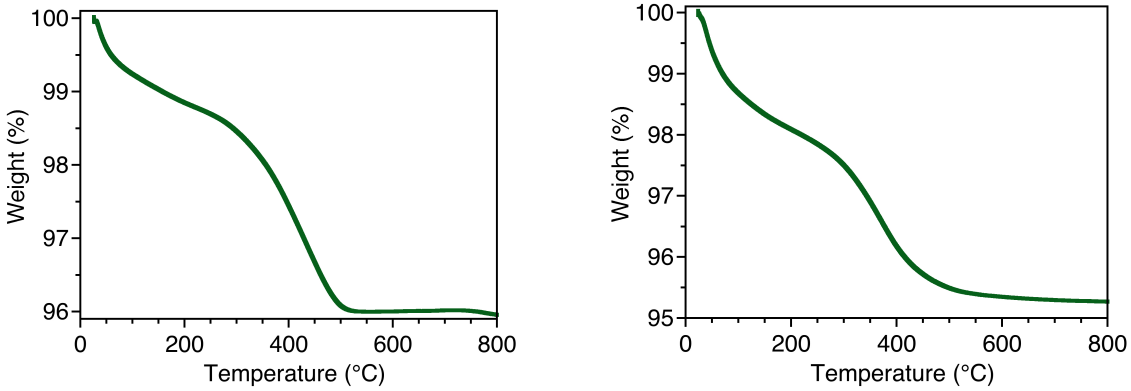

Figure 4.14. TGA spectra of Hinton A lignin@TiO_2 nanoparticles (reaction time of 16 h (left) and 24 h (right)) from scaled- up reaction for the large batch synthesis of Hinton A lignin@TiO_2 nanoparticles irradiated with UVA light from an exposure panel.

The conversion of isopropanol to acetone was measured using the new batch of nanoparticles. From Figure 4.15, it can be seen that the conversion process is similar between the original small batch reaction and the two scaled up reactions.

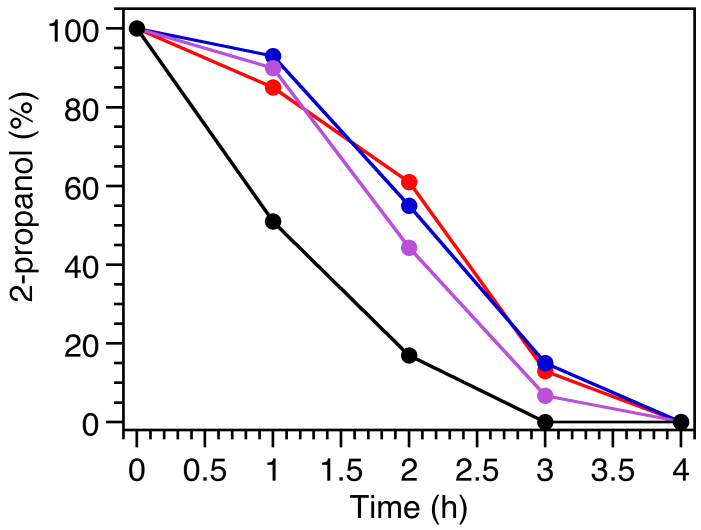

Figure 4.15. Remaining percentage of 2-propanol after irradiation with UVA-UVB in the presence of Hinton A lignin@ TiO_2 exposure panel scale up sample 1 (blue), Hinton A lignin@TiO_2 scale up sample 2 (red), small batch Hinton A lignin@ TiO_2 369 nm LED (purple) and TiO_2 (black).

In an attempt to increase the wt.% of lignin in the nanoparticles, the synthesis using a flow reaction was performed using 4x 40W UVA light bulbs. The set up for this synthetic reaction used longer bulbs and had 2 separate reaction vessels that were subjected to irradiation (Figure 4.5). In these containers, the particles were able to flow down as a thin film rather than irradiating a pool of solution. In this set up, the solution was pumped out into the first trough shaped reaction vessel, and then flowed down into a subsequent reactions vessel using a connecting tube. The slurry then flowed down the second container and back into the glass bottle holding the reaction solution. This new set up approach allowed for increased reaction time between the particles and the light source. The thin film also exposed more of the TiO_2 to the light, which could help in the photogeneration of radicals by TiO_2. This is beneficial over the pool that was formed in the exposure panel since the slurry containing lignin and TiO_2 is quite dark and the light might not fully penetrate the solution. The power of the light source for this reaction was similar to that of the exposure panel. It was slightly more powerful but covered a narrower region of the UV spectrum than the exposure panel. As shown in Figure 4.16, the resulting

nanoparticles had a similar wt.% as the nanoparticles synthesized via the exposure panel with 2.8% of lignin in the nanoparticle powder.

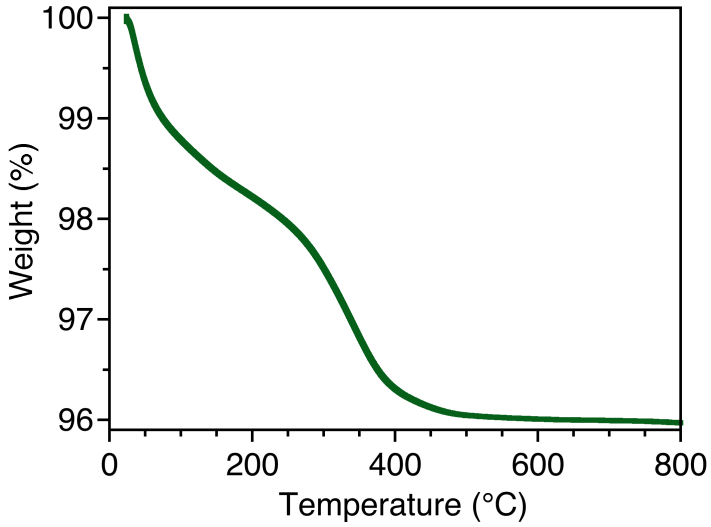

Figure 4.16. TGA of Hinton A lignin@TiO_2 synthesized using scaled- up reaction for the large batch synthesis of Hinton A lignin@TiO_2 nanoparticles irradiated with UVA light from 4x 40W bulbs.

The photocatalytic conversion of isopropanol to acetone of the new nanoparticles was analyzed. The new composites exhibited nearly identical ability to trap the free radical as the small batch reaction (Figure 4.17). Similar to the exposure panel, this reaction produced nanoparticles containing a similar wt.% of lignin to that of small batch samples.

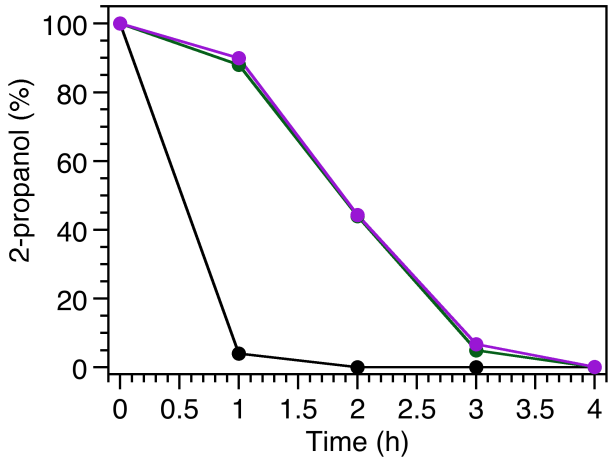

Figure 4.17. Remaining percentage of after the irradiation with UVA-UVB in the presence of Hinton A lignin@ TiO_2 with UVA light from 4x 40W bulbs (green), small batch Hinton A lignin@ TiO_2 369 nm LED (purple) and TiO_2 (black).

The last approach to a scaled- up synthesis of the lignin-modified nanomaterials was irradiating the sample with two exposure panels on either side of the flowing solution. With the increased light exposure, we decreased the reaction time to about half of the other scaled up reactions and used equal amounts (w/w) of lignin and TiO_2, since it was apparent that increasing the amount of lignin does not increase the wt.% lignin coating. The reaction was also conducted using P90 TiO_2 rather than the P25 TiO_2, which has a larger specific surface area than P25 TiO_2. Within the cosmetic industry there has been concern regarding the size of nanoparticles in cosmetics.[37] This reaction produced nanoparticles that were much darker in colour, as shown in Figure 4.18. This is an indication of a more concentrated amount of lignin in the nanocomposites, which was confirmed by TGA. As shown in Figure 4.19, the nanoparticles synthesized with two UVA panels produced particles containing 12.5 wt.% lignin on the P25 TiO_2 and 12.1 wt.% on the P90 TiO_2.

Figure 4.18. Picture of Hinton A lignin@TiO_2 nanoparticles synthesized using P25 (left) and P90 (right) TiO_2 powder.

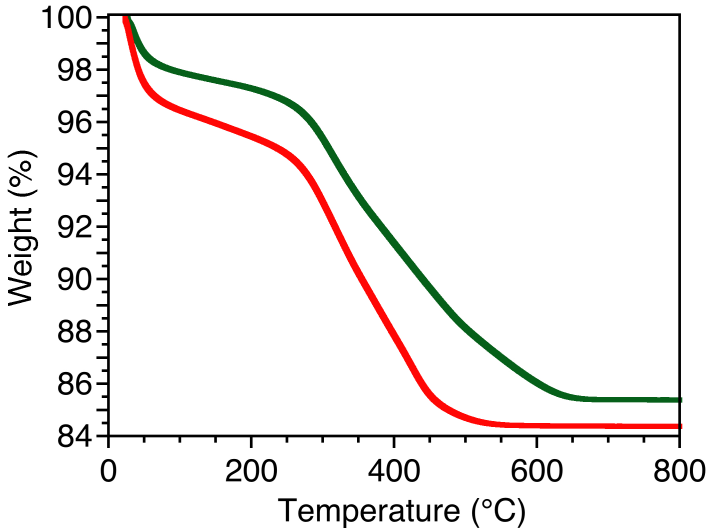

Figure 4.19. TGA of Hinton A lignin@TiO_2 nanoparticles synthesized using P25 (Green) and P90 (Red) TiO_2 powder.

Electron paramagnetic resonance (EPR)

The formation of radicals produced by TiO_2 was further explored by the use of EPR spectroscopy. EPR spectroscopy is a method that allows for the study of the paramagnetic centers that are produced by the photogenerated electrons and holes of the titanium dioxide. The reactive radical intermediates produced by irradiated TiO_2 particulates can be investigated in the presence of an indirect spin trapping technique. This is based on the chemical reaction of

short-lived radicals with a diamagnetic spin trap (ST) to produce a more stable nitroxide radical, using N-oxides [5,5-Dimethyl-1-Pyrroline-N-Oxide (DPMO), 5-(Ethoxycarbonyl)-5-methyl-1-Pyrroline-N-Oxide (EMPO)] and nitrones [α-(4-Pyridyl 1-oxide)-N-tert-butylnitrone (POBN), 4-(N-methy1pyridinium)tert-butyl nitrone (MePyBN)] spin-trapping agents.[38,39]

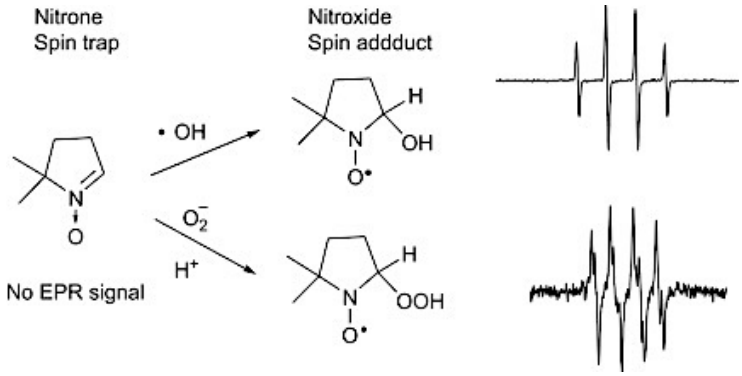

Figure 4.20. EPR signals from spin or radical adduct formation. Reprinted with permission from F.A Villamena.[40] Copyright (2017), with permission from Elsevier.

Here, we used the common spin-trapping agent DMPO (1mM) in THF which leads to the DMPO radical adduct (Figure 4.20) because the radical adduct is very redox inactive. Each sample had a final concentration of 2 mg/mL, which equates to 20% of nanoparticles in solution, which is approximately the maximum percent of TiO_2 allowed in cosmetic products (% value varies between countries). As shown in Figure 4.21, EPR spectroscopy was able to confirm that the TiO_2 generated mobile free radicals that are trapped by the lignin. We also looked at the radical trapping abilities of lignin in solution with TiO_2. Figure 4.22 shows that free lignin does trap some of the radicals generated by TiO_2 to a similar degree as the lignin@TiO_2 nanoparticles.

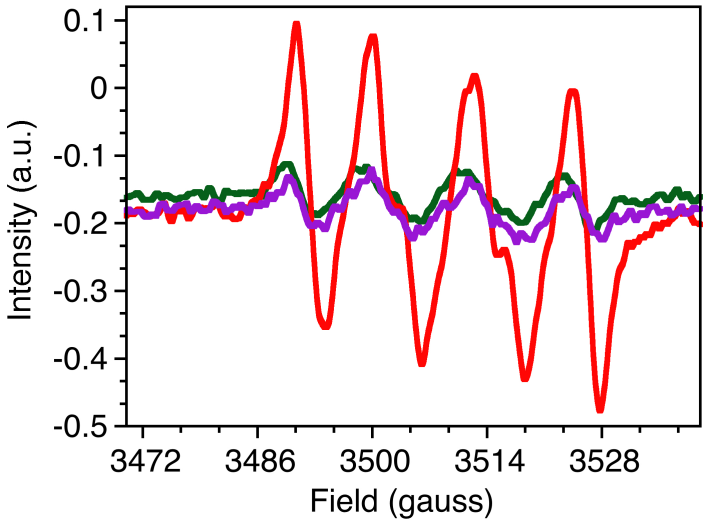

Figure 4.21. EPR spectra of TiO_2 (red), A lignin@TiO_2 (P25) (green) and A lignin@TiO_2 (P90) (purple) irradiated with light for 2, 2 and 1 min, respectively.

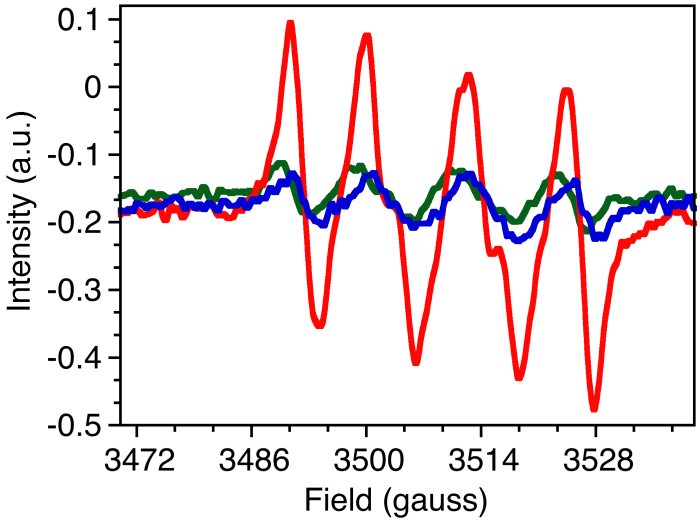

Figure 4.22. EPR spectra of TiO_2 (red), A lignin@TiO_2 (P25) (green) and A lignin + TiO_2 (blue) irradiated with light for 2, 2 and 1 min, respectively.

4.8 Conclusion

After choosing a lignin gifted to us by FPInnovations, we were able to synthesize lignin-modified nanoparticles that had a coating of approximately 3-5% lignin. We successfully transitioned the method of synthesis from a small

batch reaction to a large-scale flow reaction technique. We utilized different scale up methods in order to be able to synthesize nanoparticles in larger amounts for cosmetics purposes. Every batch from scale up manufacturing was able to retain similar radical trapping properties to the small batch samples, which is important for industry partners. Several conditions were varied in order to determine if the % of lignin coating could be increased, which was achieved by irradiating the sample with two exposure panels containing 10 UVA bulbs total (5 bulbs above and below the flow reactor). Each batch of lignin nanoparticles were analyzed and found to be able to trap the free radicals generated by TiO_2 to a similar degree.

4.9 Future Work

Future work that can be continued on this project is testing the antibacterial activity of the nanoparticles, as well as, their biocompatibility with fibroblast cells. Since TiO_2 produces ROS, which are known to kill bacteria and potentially harm mammalian cells, it would be interesting to investigate if the radical trapping abilities of the lignin@TiO_2 nanoparticles would photo-protect different types of cells. We have tested the zeta potential of the particles and TiO_2 in different media, in order to see give an indication the nanomaterials are stable in medias used for antibacterial testing. Normally, the stability of nanoparticles would be monitored over time using UV-VIS spectroscopy, however, since these particles are not soluble in solution. Therefore, the zeta potential of the particles using DLS was measured instead. DLS only gives an indication of stability because it uses the assumption that the particles are spherical and monodispersed, which we know they are not. As seen in Table 4.2 and 4.3, TiO_2 and the lignin nanoparticles are more stable over time in LB broth, however, the zeta value is lower than -20 mV, suggesting that there is not much electrostatic charge separation between particles and the nanoparticles are somewhat agglomerated. This demonstrates that perhaps any further planktonic assays should be conducted using the cylinder-plate method or mixing with the nanoparticles into agar.

Table 4.2. Average Zeta Pot of TiO_2 (0.1 mg/mL) in PBS and LB broth.

Sample	Media	Avg Zeta Potential (mV) Time (h)		
		0	1	2
TiO_2 (P25)	PBS	-20.9 ± 0.97	-18.73 ± 1.50	-16.73 ± 0.87
	LB Broth	-13.3 ± 0.99	-13.13 ± 0.17	-12.47 ± 0.29
TiO_2 (P90)	PBS	-23.07 ± 0.63	-21.43 ± 0.73	-22.7 ± 0.86
	LB Broth	-12.4 ± 0.45	-13.67 ± 0.52	-12.33 ± 0.68

Table 4.3. Average Zeta Potential of A lignin@TiO_2 (0.1 mg/mL) in PBS, LB broth or a mixture of both (LB/PBS) at varying ratios.

Sample	Media	Avg Zeta Potential (mV) Time (h)		
		0	2	5
Hinton A Lignin@TiO_2 (P25)	PBS	-19.9 ± 1.37	-16.7 ± 0.40	-14.8 ± 0.40
	LB Broth/PBS (1:3)	-16.7 ± 4.09	-14.6 ± 0.21	-14.6 ± 0.99
	LB Broth/PBS (1:1)	-10.9 ± 0.58	-12.3 ± 0.15	-11.9 ± 1.18
	LB Broth/PBS (3:1)	-12.3 ± 0.97	-11.8 ± 0.21	-11.2 ± 0.45
	LB Broth	-12.1 ± 1.12	-12.3 ± 0.74	-12.5 ± 0.61

4.10 Appendix

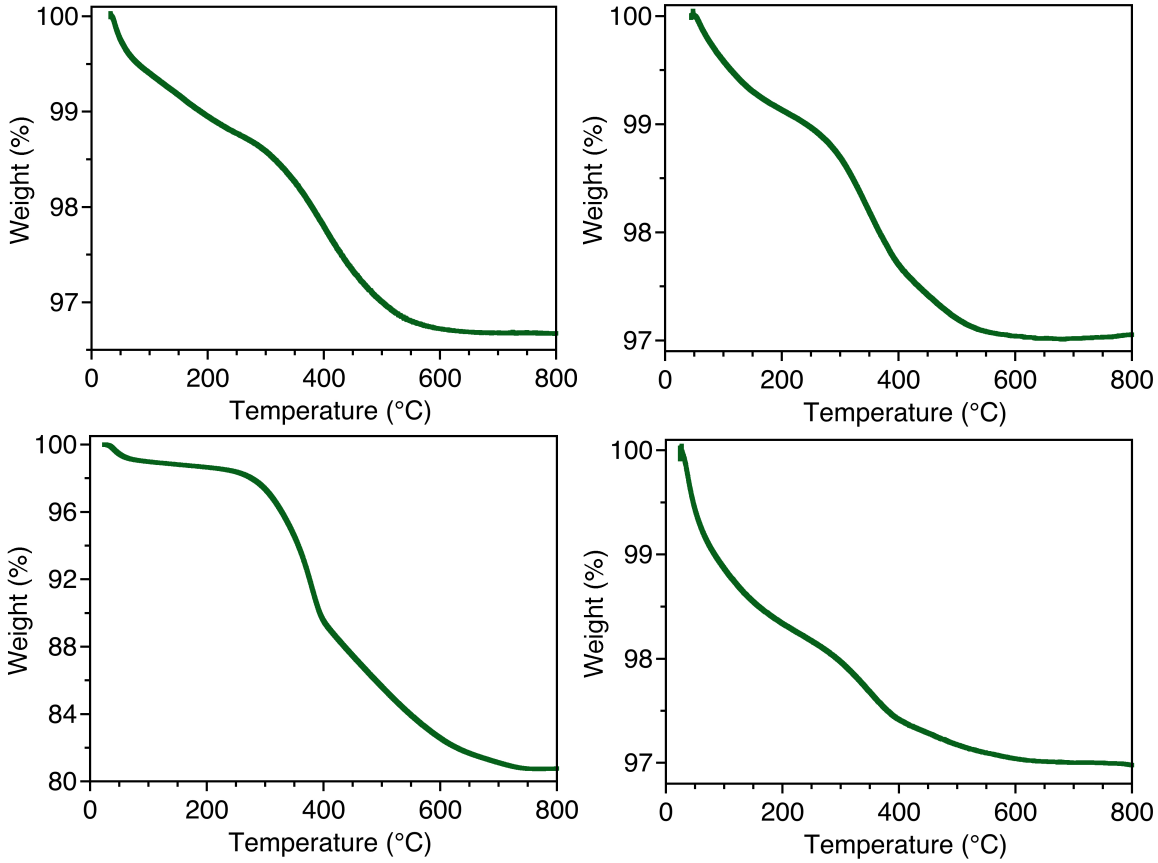

Figure 4A.1 TGA of Hinton A lignin@ TiO_2 (top left), HW lignin@ TiO_2 (top right), ZHL-10 lignin@TiO_2 (bottom left) and K31 lignin@ TiO_2 (bottom right).

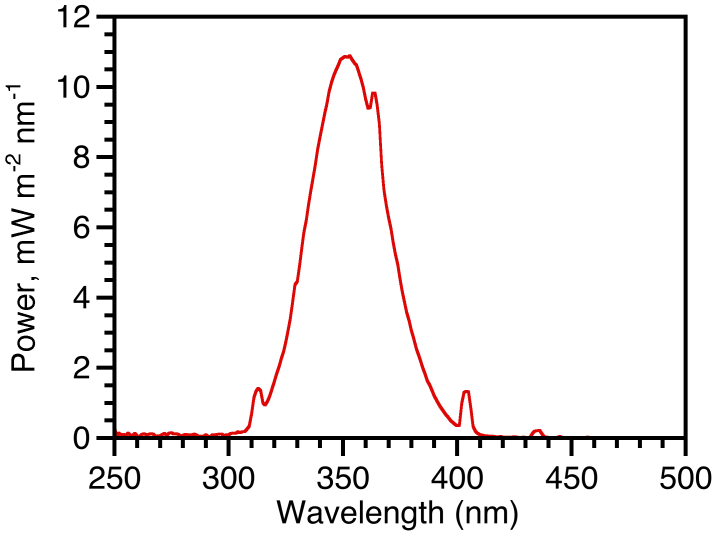

Figure 4A.2. Power emitted from exposure panel with 5 UVA bulbs at a distance of 1.5 cm from sample.

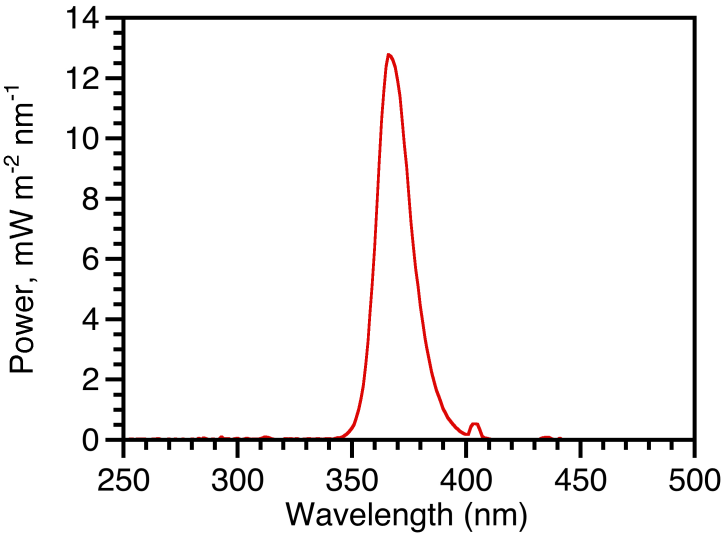

Figure 4A.3. Power emitted from 4x 40W UVA bulbs at a distance of 8 cm from sample.

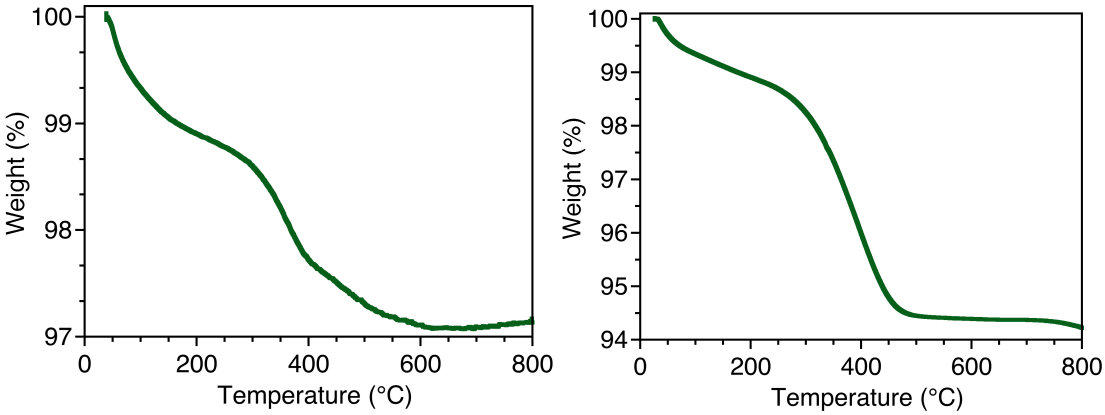

Figure 4A.4. TGA spectra of Hinton A lignin@TiO_2 nanoparticles synthesized using LED (369 nm).

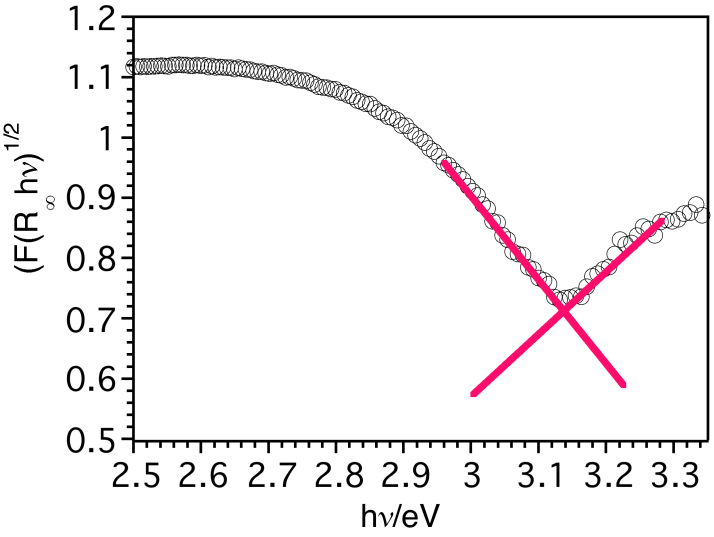

Figure 4A.5. Tauc plot of Hinton A lignin@TiO_2 nanoparticles.[35]

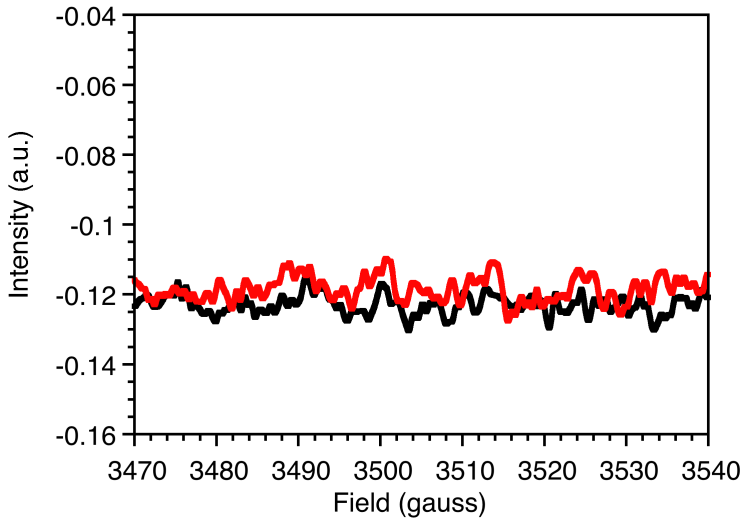

Figure 4A.6. EPR spectra of DMPO under dark (black) and irradiated with light for 5 min (red).

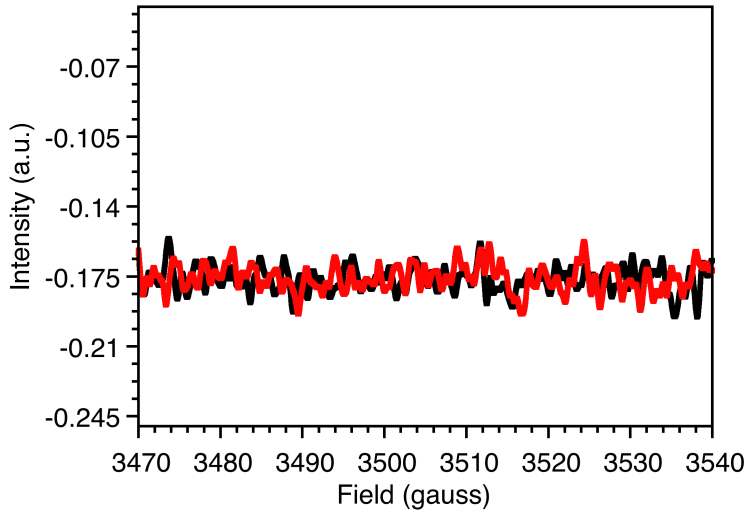

Figure 4A.7. EPR spectra of Hinton A lignin under dark (black) and irradiated with light for 1 min (red).

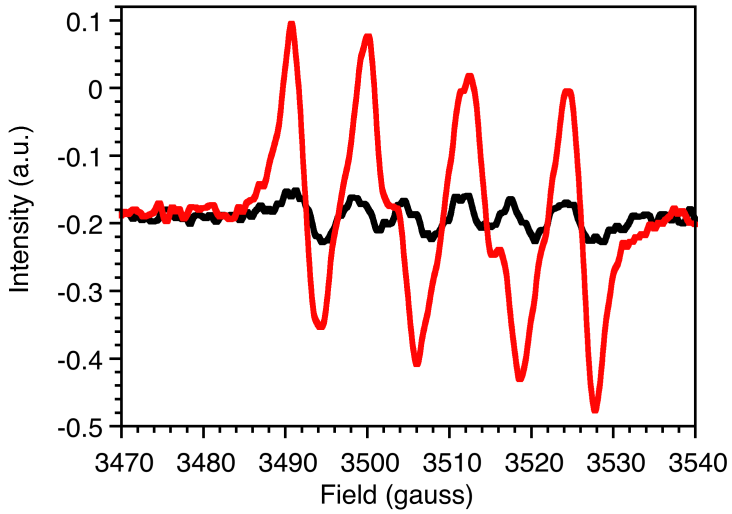

Figure 4.A8. EPR spectra of TiO_2 under dark (black) and irradiated with light for 2 min (red).

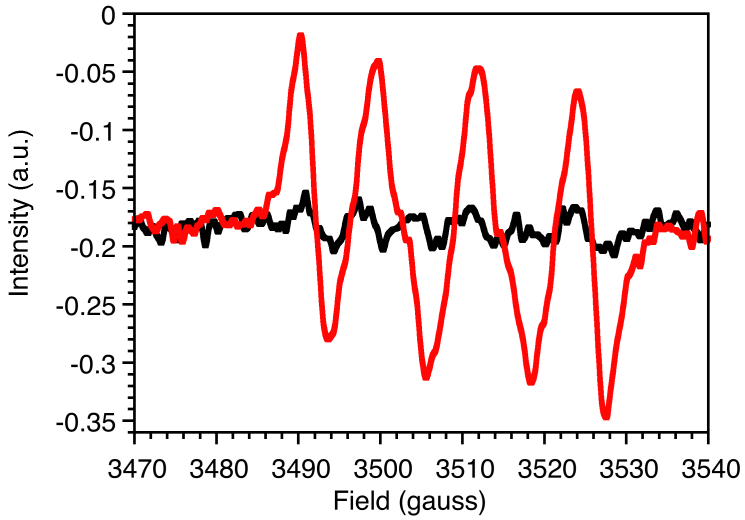

Figure 4.A9. EPR spectra of Hinton A lignin@ TiO_2 under dark (black) and irradiated with light for 2 min (red).

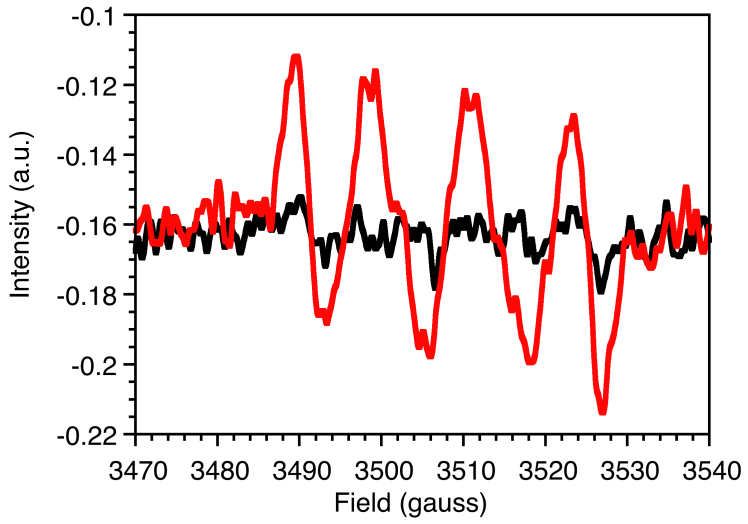

Figure 4.10. EPR spectra of Hinton A lignin@TiO_2 under dark (black) and irradiated with light for 2 min (red)**.**

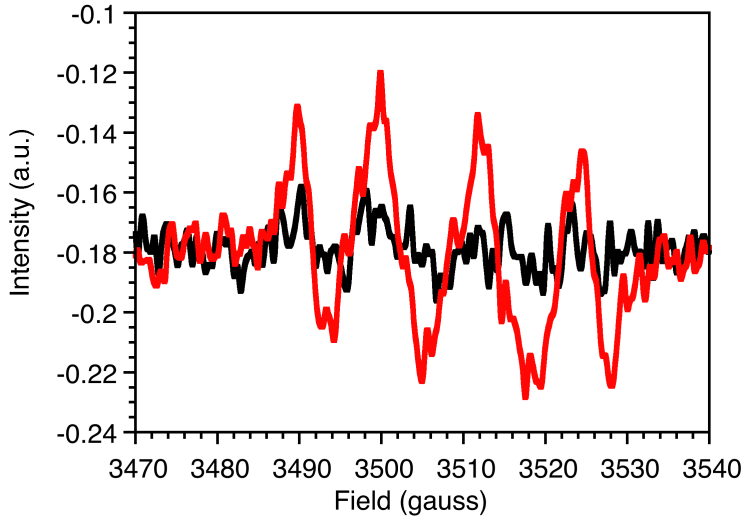

Figure 4.11. EPR spectra of a solution containing Hinton A lignin@TiO_2 (P90) under dark (black) and irradiated with light for 1 min (red).

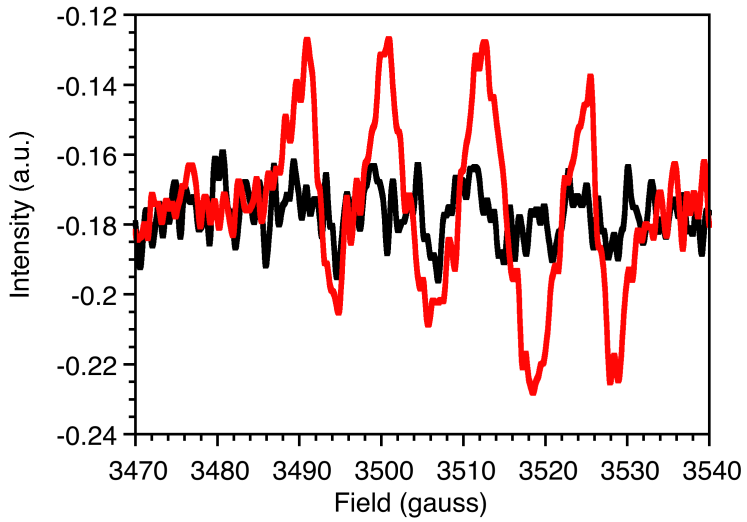

Figure 4.12. EPR of a solution containing Hinton A lignin and TiO_2 under dark (black) and irradiated with light for 1 min (red).

References

1 N. P. Patel, A. Highton and R. L. Moy, Properties of Topical Sunscreen Formulations: A Review, *J. Dermatol. Surg. Oncol.*, 1992, **18**, 4, 316–320.

2 N. Serpone, A. Salinaro, A. V. Emeline, S. Horikoshi, H. Hidaka and J. Zhao, An in vitro systematic spectroscopic examination of the photostabilities of a random set of commercial sunscreen lotions and their chemical UVB/UVA active agents, *Photochem. Photobiol. Sci.*, 2002, 12, 970–981.

3 D. R. Kimbrough, The Photochemistry of Sunscreens, *J. Chem. Educ.*, 1997, **74**, 1, 51–53.

4 K. Suozzi, J. Turban and M. Girardi, Cutaneous photoprotection: A review of the current status and evolving strategies, *Yale J. Biol. Med.*, 2020, **93**, 1, 55–67.

5 J. M. Allen and C. J. Gossett, Photochemical formation of singlet molecular oxygen in illuminated aqueous solutions of several commercially available sunscreen active ingredients, *Chem. Res. Toxicol.*, 1996, **9**, 3, 605–609.

6 N. D. M. Hodges, S. H. Moss and D. J. G. Davies, The Sensitising Effect of a Sunscreening Agent, p-Aminobenzoic Acid, in Near UV Induced Damage in a Repair Deficient Strain of Escherichia Coli, *Photochem. Photobiol.*, 1977, **26**, 5, 493–498.

7 B. M. Sutherland, p-Aminobenzoic Acid-Sunlamp Sensitization of Pyrimidine Dimer Formation and Transformation in Human Cells, *Photochem. Photobiol.*, 1982, **36**, 1, 95–97.

8 J. C. Sutherland and K. P. Griffin, p-Aminobenzoic Acid Can Sensitize the Formation of Pyrimidine Dimers in DNA: Direct Chemical Evidence, *Photochem. Photobiol.*, 1984, **40**, 3, 391–394.

9 B. Herzog, M. Wehrle and K. Quass, Photostability of UV absorber systems in sunscreens, *Photochem. Photobiol.*, 2009, **85**, 4, 869–878.

10 Ngoc, Tran, Moon, Chae, Park and Lee, Recent Trends of Sunscreen Cosmetic: An Update Review, *Cosmetics*, 2019, **6**, 4, 64.

11 E. A. Dutra, D. A. G. Da Costa E Oliveira, E. R. M. Kedor-Hackmann and M. I. R. Miritello Santoro, Determination of sun protection factor (SPF) of sunscreens by ultraviolet spectrophotometry, *Rev. Bras. Ciencias Farm. J. Pharm. Sci.*, 2004, **40**, 3, 381–385.

12 U.S. Food and Drug Administration, FDA advances new proposed regulation to make sure that sunscreens are safe and effective.

13 S. Tanemura, L. Miao, W. Wunderlich, M. Tanemura, Y. Mori, S. Toh and K. Kaneko, Fabrication and characterization of anatase/rutile-TiO_2 thin films by magnetron sputtering: A review, *Sci. Technol. Adv. Mater.*, 2005, **6**, 11–17.

14 X. W. Sun and H. S. Kwok, Optical properties of epitaxially grown zinc oxide films on sapphire by pulsed laser deposition, *J. Appl. Phys.*, 1999, **86**, 408–411.

15 T. G. Smijs and S. Pavel, Titanium dioxide and zinc oxide nanoparticles in sunscreens: Focus on their safety and effectiveness, *Nanotechnol. Sci. Appl.*, 2011, **4**, 85–112.

16 M. J. Osmond-McLeod, Y. Oytam, A. Rowe, F. Sobhanmanesh, G. Greenoak, J. Kirby, E. F. McInnes and M. J. McCall, Long-term exposure to commercially available sunscreens containing nanoparticles of TiO_2 and ZnO revealed no biological impact in a hairless mouse model, *Part. Fibre Toxicol.*, 2016, **13**, 1, 44–57.

17 N. Serpone, D. Dondi and A. Albini, Inorganic and organic UV filters: Their role and efficacy in sunscreens and suncare products, *Inorganica Chim. Acta*, 2007, **360**, 3, 794–802.

18 R. Dunford, A. Salinaro, L. Cai, N. Serpone, S. Horikoshi, H. Hidaka and J. Knowland, Chemical oxidation and DNA damage catalysed by inorganic sunscreen ingredients, *FEBS Lett.*, 1997, **418**, 87–90.

19 P. J. A. Borm, D. Robbins, S. Haubold, T. Kuhlbusch, H. Fissan, K. Donaldson, R. Schins, V. Stone, W. Kreyling, J. Lademann, J. Krutmann, D. Warheit and E. Oberdorster, The potential risks of nanomaterials: a review carried out for ECETOC, *Part. Fibre Toxicol.*, 2006, **3**, 11.

20 M. D. Newman, M. Stotland and J. I. Ellis, The safety of nanosized particles in titanium dioxide- and zinc oxide-based sunscreens, *J. Am. Acad. Dermatol.*, 2009, **61**, 4, 685–692.

21 D. Dondi, A. Albini and N. Serpone, Interactions between different solar UVB/UVA filters contained in commercial suncreams and consequent loss of UV protection, *Photochem. Photobiol. Sci.*, 2006, **5**, 9, 835–843.

22 S. Parwaiz, M. M. Khan and D. Pradhan, CeO_2-based nanocomposites: An advanced alternative to TiO_2 and ZnO in sunscreens, *Mater. Express*, 2019, **9**, 3, 185–202.

23 S. Livraghi, I. Corazzari, M. C. Paganini, G. Ceccone, E. Giamello, B. Fubini and I. Fenoglio, Decreasing the oxidative potential of TiO_2 nanoparticles through modification of the surface with carbon: A new strategy for the production of safe UV filters, *Chem. Commun.*, 2010, **46**, 44, 8478–8480.

24 A. Morlando, V. Sencadas, D. Cardillo and K. Konstantinov, Suppression of the photocatalytic activity of TiO_2 nanoparticles encapsulated by chitosan through a spray-drying method with potential for use in sunblocking applications, *Powder Technol.*, 2018, **329**, 252–259.

25 P. K. Shetty, V. Venuvanka, H. V. Jagani, G. H. Chethan, V. S. Ligade, P. B. Musmade, U. Y. Nayak, M. S. Reddy, G. Kalthur, N. Udupa, C. M. Rao and S. Mutalik, Development and evaluation of sunscreen creams

containing morin-encapsulated nanoparticles for enhanced UV radiation protection and antioxidant activity, *Int. J. Nanomedicine*, 2015, **10**, 6477–6491.

26 M. Morsella, N. D'Alessandro, A. E. Lanterna and J. C. Scaiano, Improving the Sunscreen Properties of TiO_2 through an Understanding of Its Catalytic Properties, *ACS Omega*, 2016, **1**, 3, 464–469.

27 R. Vanholme, B. Demedts, K. Morreel, J. Ralph and W. Boerjan, Lignin biosynthesis and structure, *Plant Physiol.*, 2010, **153**, 3, 895–905.

28 M. S. Karunarathna and R. C. Smith, Valorization of lignin as a sustainable component of structural materials and composites: Advances from 2011 to 2019, *Sustain.*, 2020, **12**, 2, 734.

29 Y. Ge, Q. Wei and Z. Li, Preparation and evaluation of the free radical scavenging activities of nanoscale lignin biomaterials, *BioResources*, 2014, **9**, 4, 6699–6706.

30 V. K. Thakur, M. K. Thakur, P. Raghavan and M. R. Kessler, Progress in green polymer composites from lignin for multifunctional applications: A review, *ACS Sustain. Chem. Eng.*, 2014, **2**, 5, 1072–1092.

31 M. Morsella, M. Giammatteo, L. Arrizza, L. Tonucci, M. Bressan and N. d'Alessandro, Lignin coating to quench photocatalytic activity of titanium dioxide nanoparticles for potential skin care applications, *RSC Adv.*, 2015, **5**, 57453–57461.

32 C. Zhao, J. Huang, L. Yang, F. Yue and F. Lu, Revealing Structural Differences between Alkaline and Kraft Lignins by HSQC NMR, *Ind. Eng. Chem. Res.*, 2019, **58**, 71, 5707–5714.

33 D. Watkins, M. Nuruddin, M. Hosur, A. Tcherbi-Narteh and S. Jeelani, Extraction and characterization of lignin from different biomass resources, *J. Mater. Res. Technol.*, 2015, **4**, 1, 26–32.

34 A. H. Ab Rahim, Z. Man, A. Sarwono, W. S. Wan Hamzah, N. M. Yunus and C. D. Wilfred, Extraction and Comparative Analysis of Lignin Extract from Alkali and Ionic Liquid Pretreatment, *J. Phys. Conf. Ser.*, 2018, **1123**, 012052.

35 P. Makuła, M. Pacia and W. Macyk, How To Correctly Determine the Band Gap Energy of Modified Semiconductor Photocatalysts Based on UV-Vis Spectra, *J. Phys. Chem. Lett.*, 2018, **9**, 23, 6814–6817.

36 S. George, S. Pokhrel, Z. Ji, B. L. Henderson, T. Xia, L. Li, J. I. Zink, A. E. Nel and L. Mädler, Role of Fe doping in tuning the band gap of TiO_2 for the photo-oxidation-induced cytotoxicity paradigm, *J. Am. Chem. Soc.*, 2011, **133**, 29, 11270–11278.

37 D. M. Bowman, G. van Calster and S. Friedrichs, Nanomaterials and regulation of cosmetics, *Nat. Nanotechnol.*, 2010, **5**, 2, 92.

38 D. Dvoranová, Z. Barbieriková and V. Brezová, Radical intermediates in

photoinduced reactions on TiO_2 (An EPR spin trapping study), *Molecules*, 2014, **19**, 11, 17279–17304.

39 K. Ranguelova and R. P. Mason, The fidelity of spin trapping with DMPO in biological systems, *Magn. Reson. Chem.*, 2011, **49**, 4, 152–158.

40 F. A. Villamena, EPR Spin Trapping, *Reactive Species Detection in Biology*, ed., Elsevier, Boston, 2017, pp. 163–202.

Chapter 5
Future Work

Future work

5.1 Bacterial Cells as SEDs for H_2 Generation Using Pd@TiO_2 Photocatalyst

Further investigation into the antibacterial capacity of the Pd@TiO_2 nanoparticles would help determine if the Pd@TiO_2 nanoparticles can simultaneously eradicate the bacterial cells while generating H_2. A planktonic assay can be conducted against both gram-positive and –negative bacteria using the catalyst concentration (2.5 mg/mL) previously used in our reactions, and at lower concentrations since this is a very concentration solution for antibacterial assays. Previously, we have seen total cell death of bacteria after solar simulated irradiation, however some controls are missing and would be required to make any conclusive conclusions. Similarly, performing a biofilm eradication assay to determine if the particles have the ability to eradicate a biofilm, which a more system than the bacteria alone. This could be beneficial for their application in a flow system, since biofilms can form in water treatment systems if the there is not enough turbidity in the flow system.[1]

There are a few reports on the interaction between palladium nanoparticles and single celled microorganisms. For example, Pd nanoparticles were found to demonstrate more toxicity than Pd^{2+} ions when exposed to gram-positive bacteria, *S. aureus*. They also observed a decrease in the number of colonies when the nanoparticles were in contact with gram-negative bacteria, *E. coli*. It did require a higher concentration of nanoparticles and a longer exposure time, compared to the gram-positive before an inhibitory effect could be observed.[2] This can possibly be attributed to the structure of the cell wall of the gram-negative bacteria, as was previously mentioned in chapter 3, that can lead them having a stronger resistance to treatment.

5.2 Water purification using porphyrin attached to glass wool (GW) for potential flow system applications

Similarly to inorganic nanoparticles, organic molecules have been increasingly used for environmental purposes, including water remediation. However, as was previously mentioned, organic catalysts present the problem of catalyst separation. A possible solution is to place the catalyst on a support, but in doing so, the catalytic capabilities might be hindered or gone altogether. Therefore, the next step for this project is to further characterize the porphyrin on GW and perform a planktonic assay to measure the antibacterial capacity of the new material. Though, it might be required to include cationic substituents onto the porphyrin structure to attract the negatively charged cell walls. This is due to the fact that the mechanism of cell-death typically used by porphyrins is through the permeation of the porphyrin into cell to cause internal and external damage, killing the living cells.[3]

Risk of nanoparticle use for water remediation

A possible reason for the infrequent use of Pd based nanoparticles for environmental purposes is the reported ability for these nanoparticles to exert adverse eco-toxicological effects on different systems and populations.[4] In 2010, a study found that 5-10 nm Pd particles could be released in the surrounding environment. This study followed the nanotoxicity of the particles against kiwifruit pollen and the endpoints, which included *in vitro* pollen performance and lethality. It was found that Pd nanoparticles damaged kiwifruit pollen and inhibited pollen tube emergence and elongations at concentrations of 0.4 mg/L.[5] In addition to the examples of the effects of the Pd nanoparticles against vegetation and other ecological environments, there have also been some reports of Pd particles demonstrating potential toxicity in mammalian cell lines. For example, Iavicoli et al. demonstrated that palladium nanoparticles inhibited cell growth in both a dose and time dependent manner in rat fibroblasts and lung carcinoma human epithelial cells using both *in vitro* and *in vivo* models.[6]

These findings, amongst others, demonstrate the importance of preventing the release of metal nanoparticles and organic material into the environment. Leaching tests can be performed on glass wool containing porphyrin to determine if any free base porphyrin can potentially leak into the surrounding environment. The palladium nanoparticles can also be attached to glass wool, as was previously done by the group[7] and tested for particle leaching. Alternatively, palladium could also be replaced with elements that have lower toxicity or that more abundant.

For the application of nanomaterials for water remediation, nanoparticles alone or attached to glass wool would ideally be integrated into a flow system, which would minimize the leaching of the catalyst and allow for a continuous method for water purification.

Flow systems

Processes for water treatment can be classified as either a batch or continuous system, both providing their own advantages and disadvantages. Batch systems operate by using a chemical, physical or biological method to treat a given volume of polluted water and then discharging the gathered water. Whereas, in a continuous system, the polluted water is continuously added and treated, with the output of product being constant as well. Batch reactors have a relatively basic setup that provides relative ease when increasing the size and/or number of containment vessels. Optimization of this method often does not require the extensive reaction cell design (and redesign) and can save on time and money. However, once the strategy for the design has been optimized, continuous flow can be more cost efficient by having a greater volume-time output if the reactor hours are not excessive and/ or the reactions volume is suboptimal.

Different types of flow systems are currently being developed using heterogeneous catalysts. For example, Sacco *et al.* developed a continuous flow micro-reactor to treat coloured wastewater (crystal violet dye) through adsorption and photocatalysis. The active material was zinc oxide (ZnO) immobilized on a

zeolite pellet into a condenser and irradiated with UV-LED strips to maximize exposure to the light sources, as shown in Figure 5.1.[8]

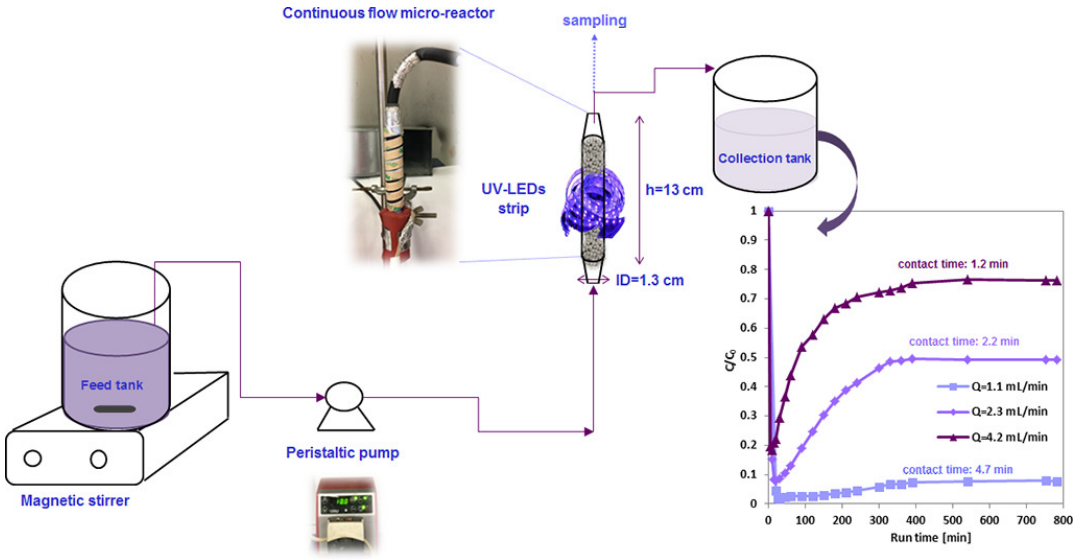

Figure 5.1. Experimental set up of continuous flow micro-reactor. Reproduced with permission from O. Sacco *et al.*[8] Copyright (2018) Elsevier, Science of the Total Environment.

Dr Ayda Elhage in the Scaiano group constructed a prototype for a flow reactor designed by Luzchem Research, Inc (Ottawa, Canada).[9] The main compartment consisted of a teflon block with 4 disk shaped grooves connected to each other and Luer joints at the input/output terminals. A glass window was placed over the top of the Teflon block to cover the reactor and allowed for light to reach the samples inside the cells. The flow reactor was sealed using two aluminum frames screwed together. A diagram of the Teflon flow reaction is presented in Figure 5.2.

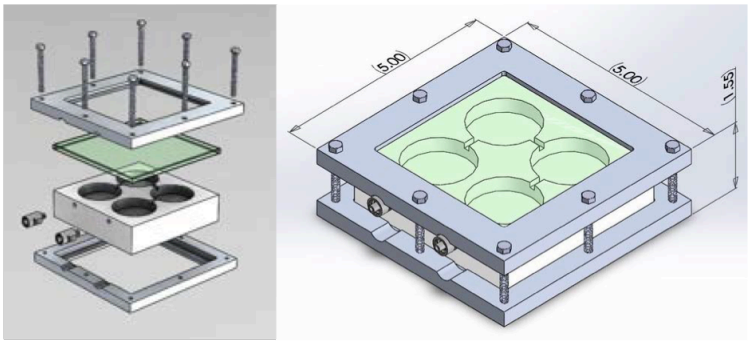

Figure 5.2. Teflon flow reactor from A. Elhage Ph. D, dissertation[9], University of Ottawa (2019).

This reactor was designed for the purpose of performing Sonogashira coupling and reductive halogenation catalytic reactions, using Pd@GW as the catalyst. These reactions had been conducted to evaluate the capabilities of the fibrous materials for heterogeneous flow catalysis using a larger volume of reactants. It was previously reported that the palladium nanoparticles on the glass wool support were able accomplish Sonogashira coupling with high yields and were able to demonstrate the reusability of the photocatalyst.[7]

5.3 Lignin@TiO_2 nanocomposites for the application in sunscreens

Lignin@TiO_2 nanoparticles project demonstrated that the nanocomposites could act as antioxidants and scavenge free radicals produced by the semiconducting material. Scaling up production of the nanocomposites yielded a few grams of the desired product. We were able to reproduce the A lignin@TiO_2 nanoparticles when scaling up to a few grams of product, using a flow reaction under UVA light. This demonstrates that the small-scale reaction can be scaled up to form larger batches for antibacterial and biocompatibility testing. Although, this is not a large enough quantity for cosmetic companies to test in their sunscreen formulations, it does give us confidence that a scale up production to that magnitude is very possible. Since we were able to synthesize the nanoparticles using flow reaction rather than a batch method, it can save industry time and money by being able to continuously produce lignin@TiO_2 nanoparticles, rather than having to stick to a batch format.

Additionally, the variability of the lignin structure that occurs during processing can result in a slight inconsistency in the thickness of the lignin coating between batches. One of the biggest challenges regarding production scale up is the separation of the catalyst from solution. Typically, separation is done using centrifugation; however, the total volume of sample per cycle of centrifugation is inadequate for the desired amount (kilogram) of nanoparticles. For this reason, scale up production of the nanoparticles is currently being done in collaboration with Greenbeaver, a Hawkesbury, ON based company. This collaboration enables access to necessary resources that can help overcome the current limitations. Additional information regarding these particles can be completed upon the success of the scale up production of the nanoparticles. Analysis of the antibacterial properties and cytotoxicity of particles from the same batch allows for consistency and validity between assays.

Whereas, TiO_2 alone has shown antibacterial capabilities[10], and that lignin nanoparticles have demonstrated some antibacterial activity,[11] we do not suspect a bactericidal or bacteriostatic effect on cells since majority of the ROS produced should be scavenged. The nanoparticles can also potentially act as a sunscreen and protect fibroblasts and skin from UV radiation.

References

(1) Maes, S.; Vackier, T.; Nguyen Huu, S.; Heyndrickx, M.; Steenackers, H.; Sampers, I.; Raes, K.; Verplaetse, A.; De Reu, K. Occurrence and Characterisation of Biofilms in Drinking Water Systems of Broiler Houses. *BMC Microbiol.* 2019, **19**, 77.

(2) Adams, C. P.; Walker, K. A.; Obare, S. O.; Docherty, K. M. Size-Dependent Antimicrobial Effects of Novel Palladium Nanoparticles. *PLoS One* 2014, **9**, e85981.

(3) Moserova, I.; Kralova, J. Role of Er Stress Response in Photodynamic Therapy: Ros Generated in Different Subcellular Compartments Trigger Diverse Cell Death Pathways. *PLoS One* 2012, **7**, 3, e32972.

(4) Leso, V.; Iavicoli, I. Palladium Nanoparticles: Toxicological Effects and Potential Implications for Occupational Risk Assessment. *Int. J. Mol. Sci.* 2018, **19**, 2, 503.

(5) Speranza, A.; Leopold, K.; Maier, M.; Taddei, A. R.; Scoccianti, V. Pd-Nanoparticles Cause Increased Toxicity to Kiwifruit Pollen Compared to Soluble Pd(II). *Environ. Pollut.* 2010, **158**, 3, 873–882.

(6) Iavicoli, I.; Farina, M.; Fontana, L.; Lucchetti, D.; Leso, V.; Fanali, C.; Cufino, V.; Boninsegna, A.; Leopold, K.; Schindl, R.; et al. In Vitro Evaluation of the Potential Toxic Effects of Palladium Nanoparticles on Fibroblasts and Lung Epithelial Cells. *Toxicol. Vitr.* 2017, **24**, 191–199.

(7) Elhage, A.; Wang, B.; Marina, N.; Marin, M. L.; Cruz, M.; Lanterna, A. E.; Scaiano, J. C. Glass Wool: A Novel Support for Heterogeneous Catalysis. *Chem. Sci.* 2018, **9**, 33, 6844–6852.

(8) Sacco, O.; Matarangolo, M.; Vaiano, V.; Libralato, G.; Guida, M.; Lofrano, G.; Carotenuto, M. Crystal Violet and Toxicity Removal by Adsorption and Simultaneous Photocatalysis in a Continuous Flow Micro-Reactor. *Sci. Total Environ.* 2018, **644**, 430–438.

(9) Elhage, A. Palladium-Based Catalyst for Heterogeneous Photocatalysis. Ph.D Dissertation, University of Ottawa, 2019.

(10) Foster, H. A.; Ditta, I. B.; Varghese, S.; Steele, A. Photocatalytic Disinfection Using Titanium Dioxide: Spectrum and Mechanism of Antimicrobial Activity. *Appl. Microbiol. Biotechnol.* 2011, **90**, 6, 1847–1868.

(11) Yang, W.; Fortunati, E.; Gao, D.; Balestra, G. M.; Giovanale, G.; He, X.; Torre, L.; Kenny, J. M.; Puglia, D. Valorization of Acid Isolated High Yield Lignin Nanoparticles as Innovative Antioxidant/Antimicrobial Organic Materials. *ACS Sustain. Chem. Eng.* 2018, **6**, 3, 3502–3514.